

UNIVERSITY OF MIAMI

SEA SURFACE STRUCTURE MEDIATION OF KINETIC ENERGY TRANSFER
AND DISSIPATION

By

Andrew W. Smith

A DISSERTATION

Submitted to the Faculty
of the University of Miami
in partial fulfillment of the requirements for
the degree of Doctor of Philosophy

Coral Gables, Florida

May 2021

©2021
Andrew W. Smith
All Rights Reserved

UNIVERSITY OF MIAMI

A dissertation submitted in partial fulfillment of
the requirements for the degree of
Doctor of Philosophy

SEA SURFACE STRUCTURE MEDIATION OF KINETIC ENERGY TRANSFER
AND DISSIPATION

Andrew W. Smith

Approved:

Brian K. Haus, Ph.D.
Professor of Ocean Sciences

William M. Drennan, Ph.D.
Professor of Ocean Sciences

Lynn K. Shay, Ph.D.
Professor of Ocean Sciences

Guillermo Prado, Ph.D.
Dean of the Graduate School

Jun A. Zhang, Ph.D.
Scientist
NOAA Hurricane Research Division/AOML/University of Miami-CIMAS

James B. Edson, Ph.D.
Senior Scientist
Woods Hole Oceanographic Institution
Woods Hole, Massachusetts

SMITH, ANDREW W. (Ph.D., Meteorology and Physical Oceanography)
Sea Surface Structure Mediation of Kinetic Energy Transfer (May 2021)
and Dissipation

Abstract of a dissertation at the University of Miami.

Dissertation supervised by Professor Brian K. Haus
No. of pages in text. (159)

Atmosphere, waves, and the ocean are coupled and indivisible as evidenced by physical processes that can be observed or measured near the air-sea interface such as the growth of waves, visible streaks, foam, bubbles, and wave breaking. Fluxes of momentum, heat, gases, salts, and marine aerosols all contribute to the transfer of energy into near-surface boundary layers as part of air-sea interactions. In these boundary layers, turbulent and wave-induced kinetic energy is produced as a consequence of flux-mean state interaction and transferred or dissipated to or within the atmospheric surface or ocean surface layers. Dissipation of this kinetic energy has been difficult to measure, and there is a paucity of measurements in high or hurricane-force wind conditions. Additionally, simultaneous investigation of surface wave evolution and sub-surface response to that wave field has not been accomplished in hurricane wind-wave conditions. Given the upscale effects of the aforementioned kinetic energy to larger scale processes such as gas exchange, climate, and hurricanes, connecting its production, transfer, and dissipation rate to the sea surface structure is critical to improving numerical model parameterizations, particularly for high-wind environments where measurements have been limited.

In this study, we have used field and laboratory measurements of fluxes, waves, turbulence, and its dissipation rate to improve understanding of sea surface mediation of kinetic energy production, exchanges, and dissipation. Field data from the LAgrangian

Submesoscale ExpeRiment (LASER, 2016) were compared to hurricane boundary layer data from several hurricanes during the Coupled Boundary Layer Air-Sea Transfer (CBLAST) campaign from 2000-2005. Laboratory data was collected during a collaborative high-wind bubble dynamics experiment at the University of Miami, and included a suite of experiments in variable wind, wave, and water temperature conditions that also captured bubble populations beneath the water surface.

Our goals were therefore to determine how turbulence and dissipation rate behave in explicitly non-hurricane and hurricane near-surface boundary layers subject to different wind and wave conditions and parameterize dissipation rates in terms of the atmospheric conditions and sea state. Experiments in the laboratory allowed us to augment and compare the field work to hurricane-force wind conditions with prescribed wave fields including wave evolution, unforced breaking, and bubble production in natural seawater. With this data in addition to the field observations, we endeavored to parameterize bubble size distributions beneath the high-wind/wave fields based on the surface wave statistics and quantify the sub-surface turbulence and dissipation in the context of wave breaking and bubble statistics.

Based on data from the nearly 1-month long LASER field campaign, turbulent kinetic energy (TKE) dissipation rates are found to be up to an order of magnitude larger in windsea, where wind and waves are coupled, as compared to swell, while field data from LASER and CBLAST collectively was generally well-described by the drag coefficient rather than purely by the 10-meter equivalent wind speed. The largest dissipation rates overall were found in near-neutral unstable atmospheric stability, where shear and buoyancy both act to produce turbulence. Transport, pressure work, and buoyancy

production of TKE had greater magnitude in swell wave conditions seen predominantly over the open ocean in deep water, and where atmospheric stability was more unstable. Ultimately, the TKE dissipation rates could be parameterized as a product of shear production of turbulence and the dissipation rate phi-function, which is a function of only the atmospheric stability.

Surface wave statistics were calculated and breaking prevalence and intensity determined given the wind stress and wave conditions. Wave breaking across multiple scales resulted in air entrainment and production of bubbles. Entrained bubble volume and number of bubbles were found to increase with stress and wave height, while bubble radius was found to decrease – behavior we attributed to the increased frequency and intensity of wave breaking. Bubbles were found to transition from being freely moving, to occasionally clustering, and finally images were seen to be largely populated with bubble clusters, particularly once the winds are at and above hurricane force. Bubble size distributions were parameterized using a lognormal distribution, successfully linking bubble size discriminations to sub-surface turbulence and degassing associated with wave breaking events.

Turbulence and dissipation rate below the surface increased with added energy input from the wind and subsequent increased wave breaking. Steeper, longer waves observed in monochromatic wave conditions we tested produced greater rates and intensity of breaking and subsequently more turbulence and higher dissipation rates. Hinze scale estimates of the maximum bubble size attainable against sub-surface turbulent shear forces was smaller in these monochromatic conditions compared to the broad-spectrum JOint North Sea WAves Project (JONSWAP) wave conditions modeled after open ocean

conditions. In both field and laboratory data, sub-surface dissipation rates exceed wall layer theory as a consequence of wave-induced turbulent fluxes.

DEDICATION

I dedicate this dissertation to my fiancé Alison Enchelmaier, for her tireless encouragement and love during my pursuit of science, this degree, and in all my passions and endeavors.

In loving memory, for Charles Keith Comeaux and Edna Millie Enchelmaier, whose love and the joy they brought to others will be sorely missed – and never forgotten. Thank you for being my family, and the greatest of role models.

ACKNOWLEDGEMENTS

I would like to first thank my advisor, Dr. Brian Haus, for giving me the opportunity to pursue this research and explore laboratory and field work as part of my scientific career. His guidance, encouragement, and advice to collaborate and get involved have afforded me exciting, educational, and fruitful opportunities and have advanced my growth and knowledge as a scientist.

I would also like to thank my committee members, Dr. William M. Drennan, Dr. Jun Zhang, Dr. Nick Shay, and Dr. Jim Edson, whose expertise, feedback, and questions posed to me have reminded me to remain diligent, skeptical, and intentional in my scientific pursuits. I am grateful and fortunate to have had the privilege of such an experienced and involved doctoral committee.

Special thanks to scientists and laboratory colleagues Dr. Rachel Stanley, Dr. Nathan Laxague, Dr. David Ortiz-Suslow, and Dr. Neil Williams with whom I had the fortune of collaborating and working with. Each of you brought me knowledge, perspective, and reminded me to remain ambitious but present.

I also greatly appreciate the friendship, fellowship, and help of the SUSTAIN laboratory team, especially Dr. Milan Curcic, Dr. Ming Shao, Mike Rebozo, Cedric Guigand, and Wellesley student Lumi Kinjo.

Lastly, this work would not have been possible without the love and support of my parents, Jason and Melissa Smith, my brothers Simon and Jacob Smith, my grandfather Dr. Winston Smith, grandfather Anthony Constantine, friends from RSMAS including Kurt Hansen, Matthias Ibach, Christian Kunzi and Hanjing Dai, friends from Miami including Matthew Toich, Julie Ivers, Stephan Proctor, Brie Teasdale, Heather Gordon, Liz Watkins,

Amanda Barton and Reed Barton, and my future family including Scott and Karen Enchelmaier, Lindsey Enchelmaier, and Kevin White.

This research has been generously supported by grants from the Consortium for Advanced Research on the Transport of Hydrocarbons in the Environment (CARTHE), the National Oceanographic and Atmospheric Administration (NOAA), the National Science Foundation (NSF), and the Gulf of Mexico Research Initiative (GoMRI).

TABLE OF CONTENTS

	Page	
List of Figures	viii	
List of Tables	xvii	
Chapter		
1	INTRODUCTION	1
1.1	Background and literature review	1
1.1.1	Turbulent kinetic energy in surface layers	1
1.1.2	Dissipation rate of turbulence	10
1.1.3	Sea surface structure evolution	13
1.1.4	Bubble production and governing physics	17
1.2	Motivation and research objectives	22
2	DATA AND ANALYSIS METHODOLOGY	25
2.1	Data	25
2.1.1	Field campaign background and objectives	25
2.1.2	Ship data	26
2.1.2.1	Flux tower	27
2.1.2.2	Ultrasonic distance meter array	27
2.1.2.3	Microthermosalinograph	28
2.1.2.4	Marine Doppler radar	28
2.1.3	Laboratory experiments overview and objectives	28
2.1.4	Laboratory wind-wave tank facility	30
2.1.5	Laboratory data	31
2.1.5.1	Noble gas mass spectrometry and discrete sampling	31
2.1.5.2	Air-side instrumentation and measurements	32
2.1.5.3	Sub-surface instrumentation and measurements	33
2.2	Analysis methodology	35
2.2.1	Motion correction for ship data	35
2.2.2	Eddy covariance fluxes and signal decompositions	36
2.2.3	Turbulence spectra and dissipation rate	40
2.2.3.1	Atmospheric surface layer	40
2.2.3.2	Sub-surface laboratory	41
2.2.4	TKE budget in the atmospheric surface layer	44
2.2.5	Open ocean sea state determination	45
2.2.6	Laboratory wave crest analysis	47
2.2.7	Wave growth and directional wave spectra	49
2.2.8	Bubble imaging and feature determination	50
2.3	Summary	54
3	TURBULENCE, FLUXES, AND DISSIPATION IN THE ATMOSPHERIC SURFACE LAYER	56
3.1	Turbulent kinetic energy observations and ambient conditions	56
3.2	Flux observations	59

3.3	Dissipation rate measurements	62
3.3.1	Dissipation rates from different regimes and platforms	63
3.3.2	TKE dissipation as a surface layer heat flux	67
3.3.3	Dissipation rates in windsea and swell	72
3.4	Normalized turbulent kinetic energy budget	78
3.5	Parameterization of TKE dissipation rate	81
3.6	Summary	83
4	LABORATORY SUB-SURFACE TURBULENCE AND DISSIPATION BENEATH HURRICANE WIND AND WAVE CONDITIONS	85
4.1	Surface wave statistics	85
4.1.1	Wave conditions in the experiments	85
4.1.2	Wave breaking	90
4.2	Bubble size distributions	96
4.2.1	Field versus laboratory data	97
4.2.2	Monochromatic versus spectrum wave conditions	100
4.2.3	Bubble size distribution parameterization	110
4.2.4	Validation of bubble size distribution parameterization	112
4.3	Wave-scaled sub-surface turbulence dissipation	116
4.3.1	Wave growth rate in monochromatic and spectrum waves	117
4.3.2	Wind input to waves	119
4.3.3	Sub-surface turbulence & wave-scaled TKE dissipation rates	126
4.4	Bubble spectra response to sub-surface turbulence	132
4.4.1	Hinze scale	133
4.5	Summary	136
5	CONCLUSIONS	141
REFERENCES		148

LIST OF FIGURES

	Page
1.1 Fluid flow over a flat plate, with vertical profiles of velocity $u(y)$ labeled in laminar, transition, and turbulent regions of the flow. Adapted from Schlichting (1979).	2
1.2 Examples of the triple decomposition of instantaneous velocity above laboratory waves captured using LIF and PIV cameras into mean, turbulent, and wave-coherent contributions. All quantities are plotted in meters per second. Wind speed increases from the upper-most row to the bottom-most row. Figure source: Buckley and Veron (2017), Figure 7.	6
1.3 Dissipation rate versus depth in the wall-layer coordinates of Soloviev et al. (1988). The vertical line represents the result of wall layer theory: $u_*^3 \kappa^{-1} z^{-1}$. The three dashed lines represent the predictions from the model of Craig and Banner (1994) for roughness lengths of 0.1, 1.0, and 10 meters with $\alpha = 100$. Other parameters in the Craig and Banner model are as in their Table 1. Source: Drennan et al. (1996), Figure 4.	9
1.4 Turbulent energy spectra and subsequent energy cascade for 3D turbulence. Figure source: Vallis (2006), Figure 8.3.	12
1.5 Side-looking mounted camera images of bottom-illuminated waves in the SUSTAIN wind-wave tank. Imaging commenced at 50 frames per second, though images here are of order 1 second apart. (a) Forward crest of wave approaching from left with microbreaking or light spilling on the crest itself (b) Tips of wave crest destabilizing, directional spreading is noticeable (c) Wave crest plunges and breaks, with spray globules and detachment near the crest (d) Breaking-induced entrainment and bubble plumes seen trailing slightly behind the crest and downward. Disruption of the smooth interface by breaking and wall friction increase the scattering and therefore, brightness of the aforementioned features.	16
1.6 Logarithmic timeline (in seconds) of bubble plume evolution showing the acoustic (formation) phase and the quiescent (evolution) phase. (a) Collapse of wave crest air cavity and jet intrusion at the forward edge of the collapsing crest 0.49s after wave breaks (b) Cavity collapse continues, showing associated breaking-induced shear and turbulence. (c) Establishment of bubble plume and initial bubble size distribution complete at about 2s after wave breaks. Figure source: Deane and Stokes (2002).	18
1.7 Table of Hinze scale values based on laboratory, surf zone, and open ocean data from the respective publications. Source: Deane et al. (2016)	20

1.8	Schematic depiction of growth and collapse of bubble in acoustic cavitation. The blue sinusoidal curve physically represents the air-sea interface in terms of the various sea surface structures (waves). Figure source: Abbas et al. (2013)	22
2.1	(a) Primary site for the LASER experiment in the Gulf of Mexico. Solid blue lines show the recording periods and track of R/V <i>F.G. Walton Smith</i> . The red circle is the location of the <i>Deepwater Horizon</i> oil rig. The magenta hatched square shows the location of the DeSoto Canyon region. Black contours with numbers are the isobaths in meters. (b) Bow instrumentation on R/V <i>F.G. Walton Smith</i> during LASER. Group A (B) refer to the starboard (port) flux towers, equipped with IRGASON and RM Young sonic anemometers and a Rotronic relative humidity/air-temperature (RH/AT) sensor numbered in that order on each tower. Group C refers to the array of five Senix ultrasonic distance meters (UDMs).	26
2.2	Schematic of the test section of the SUrge STructure Atmosphere INteraction (SUSTAIN) facility wind-wave tank. The large black arrow on the left side of the schematic indicates the direction of air-flow. The instrument locations are indicated with symbols.	31
2.3	The bubble shadowgraph imager unit (a) photograph and (b) schematic diagram of components and operation concept. The blue arrows show the path of light from the LED. The shadowed objects in the center between the nodes are bubbles. Schematic not to scale.	35
2.4	(a) Sonic anemometer zonal velocity (starboard tower) and water surface elevation from R/V <i>F.G. Walton Smith</i> where $U_{10} = 8.80 \text{ ms}^{-1}$. Total and mean velocities are in black and red, respectively. Ultrasonic distance meter (UDM) derived water surface elevation, , is plotted in magenta. (b) Sub-surface zonal and vertical velocity components, and water surface elevations from the SUSTAIN wind-wave tank laboratory. Total and mean velocities are in black and red, respectively. Wave-coherent zonal and vertical velocities are in lime green. Water surface elevation is in magenta. The horizontal axis in each figure is the time in seconds relative to the start of the record.	39
2.5	Vectrino ADCP de-spiking example using Goring and Nikora (2002) 3D phase-space algorithm. (a) Raw timeseries and spikes identified (b) Velocity versus derivative within the 3D phase space (c) Derivative versus Laplacian of velocity within the 3D phase space. Red values are spiky, blue values are good, and the black circle indicates the Poincare ellipse. Aspect ratio of the figures not to scale.	42
2.6	(a) Three waves of different non-linearity, where the blue solid line is an incipient breaking wave with asymmetry, skewedness and steepness, c.f. Babanin et al. (2007). (b) Example wave crest analysis from a monochromatic wave case in the SUSTAIN wind-	48

	wave tank. Water surface displacement η is in black solid, wave crests and troughs are indicated by blue and red triangles, respectively. Magenta and yellow lines identify the height and width of wave features. Green and red squares are situated at zero crossings in η to denote forward and rear edges of the waves.	
2.7	Optical physics of light and scattering through spherical bubbles per Snell's Law. A schematic is shown on the left, with a bubble identified from shadowgraph images to scale on the right. Yellow arrows indicate the path of light, with dashed lines indicating light passing through the bubble. The thickness of yellow arrows indicates the amount of light reaching the location. The angle θ_{crit} is the angle beyond which there is total internal reflection and hence, no refraction or bending of the light.	50
2.8	Percent error in (a) center position (b) radius, and (c) circularity comparing CHT and RP analysis methods as a function of absolute bubble gradient (interior versus exterior illumination of bubble) from open ocean wave spectrum conditions in SUSTAIN. All errors are percent errors. The magenta line is a linear fit or trend line. The black boxes and error bars indicate the median and standard deviation, respectively.	53
2.9	Comparison of Circular Hough Transform (CHT) and region properties (RP) analysis, where identified bubble boundaries are given in blue and red for the two methods, respectively. (a) Entire raw image with background filtered using a reference image (b) Zoomed in on a cluster of bubbles identified with CHT (c) Zoomed in further to show a comparison of object boundaries, center positions, and size using CHT and RP analysis.	54
3.1	Summary of meteorological and oceanographic conditions during the LAgrangian Submesoscale ExPeRiment (LASER) from January 19 2247 – February 14 0907 UTC 2016. (a) Local rate of change of TKE ($\partial \bar{\epsilon} / \partial t^{-1}$) and average TKE dissipation rate $\bar{\epsilon}$ (b) Water temperature T_w and air temperature T_a and water depth h (c) 10-meter equivalent wind speed U_{10N} and wave age $c_p U_{10N}^{-1}$ after Pierson and Moskowitz (1963) and (d) wind and wave direction relative to ship heading. All units are given in the figure.	56
3.2	Sea conditions during LASER (2016). (a) Dominant wave phase for each wave spectrum as a function of water depth. The green dashed lines correspond to different wavelength values L . The black thick lines segregate shallow, intermediate, and deep water conditions according to dominant wave aspect ratio. (b) Water surface elevation spectra plotted in semi-logarithmic coordinates with their median plotted in the heavy lines. The green dashed curve corresponds to f^{-4} .	58
3.3	(a) Zonal momentum flux ogives for windsea (blue) and swell (red) wave conditions during LASER (2016), with the binned mean and standard deviation according to length of data overlaid (b) Percent	60

	of turbulence captured considering the cospectrum of zonal and vertical velocity perturbations, with color coding as in the left panel.	
3.4	(a) Wind stress τ from eddy covariance (EC) method and based on COARE 3.5 bulk algorithm color-coded by wave condition (b) Sensible heat flux and (c) latent heat flux. A black dashed 1:1 line is also given in each plot. Binned mean and standard deviation are included in each plot. Units are Nm^{-2} in (a) and Wm^{-2} in (b) and (c).	61
3.5	Zonal velocity spectra ($\text{m}^2\text{s}^{-2}\text{Hz}^{-1}$) derived from 10-minute velocity timeseries from the (a) port and (b) starboard sonic anemometers during LASER. The gray solid lines in (a) and (b) show individual spectra. The per-frequency-bin median is shown by magenta circles. The solid lime green line is the $f^{-5/3}$ slope line for the inertial subrange. (c) The Taylor's frozen turbulence ratio given by (3.1) as a function of drag coefficient.	63
3.6	Plots of horizontal aircraft track superimposed on top of a <i>GOES-12</i> image and the aircraft altitude in color varying with time (UTC). The measurements were taken on September 2003 in Hurricane Fabian. Image is courtesy of the Naval Research Laboratory, Monterey, CA. Figure and caption from Zhang (2010).	64
3.7	(a) Wind stress and (b) 10-meter neutral drag coefficient $C_{D10N} = u_*^2 U_{10N}^{-2}$ from LASER (Smith, Haus, and Zhang, 2019) in circles and CBLAST (Zhang, 2010) in \times s. The magenta lines are the average data from Edson, et al. (2013). Error bars are one standard deviation.	65
3.8	Turbulent kinetic energy (TKE) dissipation rate (m^2s^{-3}) as a function of (a) 10-meter neutral wind speed and (b) drag coefficient. Blue and red circles indicate the LASER (2016) windsea and swell condition data, respectively. Large circles indicate binned averages, with error bars giving the standard deviation. Data from Zhang (2010) is given in black \times s as in Figure 3.7. In both panels, the y -axis is plotted in logarithmic scale.	66
3.9	Dissipative heating (Wm^{-2}) measurements as a function of (a) U_{10N} using the theoretical equation $\rho C_{D10N} U_{10N}^3$ from Bister and Emanuel (1998) and from explicitly measured TKE dissipation rates via $\rho \bar{\epsilon} z_1$ after Zhang (2010). In both panels, the circles and \times s indicate data from LASER and CBLAST (Zhang, 2010), respectively. Large markers indicate the median of binned data, with error bars denoting standard deviation. In both panels, the y -axis is plotted in logarithmic scale.	69
3.10	(a) Ratio of dissipative heating (heat flux) and sensible heat flux (percentage, %) as a function of Monin-Obukhov stability $\zeta = zL_\zeta^{-1}$ (b) Timeseries depiction of the ratio of dissipative and sensible heat fluxes (black, %), shear production of TKE (blue) and	71

	buoyancy production of TKE (green). The TKE production terms are given in m^2s^{-3} . The x -axis is the date (MM/DD).	
3.11	TKE dissipation rate (m^2s^{-3}) from LASER as a function of the Monin-Obukhov shear production $u_*^3 \kappa^{-1} z^{-1}$ in windsea (blue) and swell (red) wave conditions. Data from Zhang (2010) is included as black \times s. The 1:1 line where $\bar{\epsilon} = u_*^3 \kappa^{-1} z^{-1}$ is shown in thick black dashed lines.	73
3.12	(a) Wave-scaled roughness using (3.7; C55) parameterized using the aforementioned D03 wave-age parameterization. (b) As in (a), except using YT01 steepness parameterization. In each panel, the black dash-dot line connects the binned average values (black squares) from Drennan et al. (2005). Blue and red circles indicate the LASER (2016) data in windsea and swell conditions, respectively. Binned average values are in colored squares.	76
3.13	(a) TKE dissipation rate (m^2s^{-3}) from LASER (yellow, left axis) and wave-scaled roughness $z_0 H_{sig}^{-1}$ (dimensionless; green, right axis) parameterized via (3.7; C55), D03 (purple), and YT01 (steel blue). (b) Wave age with the Pierson and Moskowitz (1964) criterion value of 1.2 marked in red dot-dashed line. The x -axis is the date (MM/DD) of the measurements.	77
3.14	(a) Normalized TKE budget as a function of Monin-Obukhov stability, ζ . Curves from Edson and Fairall (1998) are in solid black. For the LASER data, values from windsea are given by blue circles and swell by red squares. Each TKE budget term is labeled. The magenta dotted line indicates $\zeta = 0$	80
3.15	(a) TKE dissipation rate as a function of the MOST parameterization (Ortiz-Suslow, et al. 2020) in windsea (blue) and swell (red) conditions. The black-dashed line indicates 1:1. (b) TKE dissipation rate measurements (black), parameterized (magenta), and the corresponding wave age (lime green).	82
4.1	Wave spectra and statistics based on individual crest analysis from Babanin (2007). (a) Monochromatic water surface elevation spectra (b) JONSWAP water surface elevation spectrum (c) Median wave frequency (d) Median wavenumber (e) Median wave steepness. In panels (c)-(e), the triangles and circles indicate statistics from the JONSWAP spectrum and monochromatic wave conditions, respectively.	86
4.2	Water surface elevation timeseries segment $\eta(t)$ (blue) and instantaneous frequency $F(t)$ (black) for (a) Experiment 8 and (b) Experiment 34.	91
4.3	Wavelet amplitude segment for (a) Experiment 8 and (b) Experiment 34 as in Figure 4.2. Overlaid in magenta is the localized total energy. The black stars, where present, are the location of wave crests satisfying the wave crest downward acceleration breaking criterion $AF_l^2 \geq \beta_0 g$.	92

4.4	(a) Percentage of wave crests satisfying the aforementioned breaking criteria for Runs 1-8 (red) and Runs 27-34 (blue) and (b) Localized wave energy at breaking wave crests in the same experiments and colors, respectively. Error bars denote one standard deviation, and the marker indicates the mean. The black line denotes 1:1. In both panels, the x -axis is wind stress.	94
4.5	Histogram of a bubble size distribution (blue border bars) in terms of bubble size in pixels contrasted with the lognormal distribution (red). Figure and caption adapted from Riquelme et al. (2013).	98
4.6	(a) Normalized bubble size distributions from prior field, laboratory, and numerical model studies listed in Table 4.3. (b) Normalized lognormal fits corresponding to each distribution given in panel (a).	99
4.7	Probability distributions $P(r)$ for bubble size distributions (blue) and the lognormal distribution fit obtained using the maximum likelihood method (MLM, red) for (a) monochromatic wave conditions from Runs 2,7,4, and 6 from left to right (b) JONSWAP spectrum wave conditions from Runs 31,33,27, and 29 from left to right. Bubble radius is binned into 49 bins $dr = 30.25 \mu\text{m}$ equal to 1 square pixel from the images.	101
4.8	Bubble size distributions for (a) monochromatic (Experiments 1-8) and (b) JONSWAP spectrum waves (Experiments 27-34), color-coded by U_{10N} . Colored circles indicate the bin average, and error bars show 1 standard deviation.	102
4.9	Bubble statistics as a function of wind-wave Reynolds number Re_{Hw} . (a) Total integrated bubble volume (b) number of observed bubbles and (c) bubble radius.	105
4.10	Colorized bubble shadowgraph images from (a) monochromatic experiments 2,7,4, and 6 from left to right and from (b) JONSWAP spectrum experiments 31,33,27, and 29, respectively. All images have the same color axis from 0 to 255, where darker/cooler values are closer to black and yellow/warm values are closer to white in the original images. Each image's dimensions are in pixels.	107
4.11	Bubble statistics as a function of the percentage of breaking wave crests P_b . (a) Total integrated bubble volume (b) number of observed bubbles and (c) bubble radius. Linear polynomial fits are overlaid in each panel for monochromatic (red) and JONSWAP spectrum (blue) wave conditions. As in Figure 4.9, circles and triangles indicate monochromatic wave and JONSWAP wave spectrum data, respectively.	109
4.12	Lognormal distribution parameters and their relationship to the wind-wave Reynolds number Re_{Hw} . (a) Distribution amplitude a (b) mean μ and (c) variance σ . Colors indicate the 10-meter neutral wind speed U_{10N} and as previously, circles and triangles represent the data from monochromatic and JONSWAP spectrum wave conditions, respectively.	111

4.13	Linear regression fit between parameterized and observed lognormal distribution variables (a) α (b) μ and (c) σ from the JONSWAP wave spectrum experiments. The magenta squares give the mean value across 10 bubble size distributions from each experiment. The black dashed line is 1:1. Error bars are 1 standard deviation. Pearson R^2 values are given in each panel, respectively.	113
4.14	Observed and parameterized bubble size distributions in the JONSWAP spectrum wave conditions. Histograms depicting the observed distributions are in blue bars, the parameterized distribution is plotted in red. Pearson correlation coefficients for each are given in each panel. The title indicates the wind speed in each panel (a) – (h).	114
4.15	Observed and parameterized bubble size distributions in the monochromatic wave conditions. Histograms depicting the observed distributions are in blue bars, the parameterized distribution is plotted in red. Pearson correlation coefficients for each are given in each panel. The title indicates the wind speed in each panel (a) – (g).	115
4.16	Measured wave growth rate $\beta_m(\omega, \theta)$ in (a) JONSWAP wave spectrum conditions during Experiments 27-34 and (b) monochromatic wave conditions during Experiments 1-8. Average wave growth rate (across angular frequency ω for $\theta = 0$) as a function of wind speed is given in panel (c). In panels (a) and (b), the mean wave growth rates are indicated by triangles or circles colored by U_{10N} . Black error bars indicate 1 standard deviation.	118
4.17	Directional wave spectra for JONSWAP spectrum conditions in Experiments 27-34 plotted in polar coordinates. Each polar plot has the same value axis, and the wind speed is given above each plot.	119
4.18	Directional wave spectra for monochromatic conditions in Experiments 1-8 plotted in polar coordinates. Each polar plot has the same value axis as in Figure 4.17, and the wind speed is given above each plot.	120
4.19	Significant wave height calculated from wave-wire water surface elevation timeseries compared with manual calculation using the directional wave spectra constructed using wavelet directional method (WDM). Plot includes both JONSWAP spectrum and monochromatic wave values from Experiments 27-34 and Experiments 1-8.	121
4.20	Product of wave growth rate and directional wave spectrum averaged over angular wave frequency (a, c) and wave direction (b, d) from (a, b) JONSWAP spectrum experiments 27-34 and (c, d) monochromatic experiments 1-8. Data are colored by U_{10N} indicated in the legends.	122
4.21	Energy input from wind to waves F as a function of inverse wave age $u_* c_p^{-1}$ from Drennan et al. (1996) in black squares, and from the SUSTAIN wind-wave tank in circles. Wave condition is	124

- indicated by the color and legend. The black dashed lines correspond with $F \approx \alpha_F(u_*c_p^{-1})^2$ where $\alpha_F = 0.132$ in the upper dashed line and $\alpha_F = 0.076$ in the lower dashed line. 126
- 4.22 Vectrino II 3-D ADCP derived (a) mean water velocity, (b) water-side friction velocity, and (c) signal to noise ratio (SNR) in JONSWAP spectrum (blue triangles) and monochromatic (red circles) wave conditions. Each point is an average taken over the 0.012-meter region of the measurement profile. Error bars are indicated in each figure. 126
- 4.23 Vectrino II 3-D ADCP derived zonal water velocity spectra $S_{uu}(f)$ and isotropic region identified by ARIIS for JONSWAP wave spectrum conditions, experiments 27-34. Spectra are shown in blue, the solid black line is $f^{-5/3}$, the dashed black line is zero slope, and the magenta lines bound the identified inertial sub-range. Wind speed is given above each figure. 128
- 4.24 Vectrino II 3-D ADCP derived zonal water velocity spectra $S_{uu}(f)$ and isotropic region identified by ARIIS for monochromatic wave conditions, experiments 1-8. Spectra are shown in blue, the solid black line is $f^{-5/3}$, the dashed black line is zero slope, and the magenta lines bound the identified inertial sub-range. Wind speed is given above each figure. 128
- 4.25 Wave-scaled dissipation rate $\varepsilon H_{sig} F^{-1}$ as a function of wave-scaled depth zH_{sig}^{-1} as measured in Drennan et al. 1996 (black squares) and in the SUSTAIN wind-wave laboratory tank (circles). The black solid line is the best fit of WAVES data (Terray et al. 1996) as depicted in Drennan et al. (1996) Figure 5. The other dashed lines are fits to the data from SWADE (Drennan et al. 1996) and SUSTAIN laboratory data. 130
- 4.26 (a) Signal to noise ratio and (b) TKE dissipation rate averaged over the center of the Vectrino II 3-D ADCP profile. Blue triangles and red circles indicate the data from the laboratory wave conditions indicated in the legends. Dissipation rates derived from zonal sub-surface velocity spectra in Drennan et al. (1996) are shown in black squares in panel (b). Error bars are one standard deviation. 131
- 4.27 Average bubble size distribution estimated from 14 breaking events during their acoustic phase. Error bars show one standard deviation. The inset shows the bubble size distribution 0 seconds (crosses) and 1.5 seconds into the quiescent phase (open circles). The Hinze scale is identified in this figure by the purple circle and magenta line at the bubble radius where the slope changes. 133
- 4.28 Average bubble size distributions $N_b(r)$ from the 10 shadowgraph images from JONSWAP wave spectrum experiments 27-34 (triangles) and monochromatic wave experiments 1-8 (circles). The magenta line is the Hinze scale estimate, and the black dashed 134

lines, c.f. Deane and Stokes (2002), are $r^{-3/2}$ and $r^{-10/3}$. Error bars indicate one standard deviation.

4.29

Average estimates of the Hinze scale based on bubble size distributions as a function of (a) local wave energy and (b) Monin-Obukhov (wall-layer) theory shear production of TKE in JONSWAP wave spectrum (blue triangles) and monochromatic wave (red circles) conditions. In panel (c), wall-layer shear production of TKE (proxy for dissipation rate in MOST balance) is compared with measured TKE dissipation rates. Data from Drennan et al. (1996) taken during SWADE is included in black squares. The dashed black line is 1:1, where $\bar{\varepsilon}_{meas} = \bar{\varepsilon}_{wall} = u_{*w}^3 \kappa^{-1} z^{-1}$.

136

LIST OF TABLES

	Page
4.1 Wave statistics summary table for the SUSTAIN experiments.	87

Chapter 1: Introduction

1.1 Background and literature review

1.1.1 Turbulent kinetic energy in surface layers

Turbulent kinetic energy (TKE) is the energy associated with turbulence or turbulent fluid motions. These motions or turbulence occur relative to the time-independent average or mean, and are a three-dimensional, stochastic phenomenon characterized by strong vorticity or rotation. Turbulence occurs across a spectrum of temporal and spatial scales but is transient in nature and requires energy input at large scales to persist. The non-dimensional Reynolds number is commonly used to classify a fluid flow as aerodynamically smooth (or laminar) or rough (turbulent) by comparing the inertial and viscous forces associated with the fluid, that is,

$$Re = \frac{UL}{\nu} \quad (1.1)$$

where U is the velocity or velocity scale in meters per second, L is the length scale in meters, and $\nu = \rho u^{-1}$ is the fluid dynamic viscosity in meters squared per second. Dimensionally, this compares the acceleration of the fluid flow to a roughness associated with fluid interactions or surfaces. When (1.1) is sufficiently large, the fluid flow is turbulent. TKE therefore, is produced by multi-scale interactions between moving fluids or near solid-fluid interfaces, typically of differing densities where energy is supplied at large scales. Satisfying conservation of energy, TKE may also be transported vertically, advected, or dissipated as heat. The complete equation describing the time rate-of-change of TKE is referred to as its' ‘budget’, and involves the forces of shear, buoyancy and pressure gradients.

First directly measured in the now-well known Kansas experiments in the summer

of 1968 (Wyngaard and Coté, 1971), the TKE budget has since been investigated over grassland plains (Wyngaard and Coté (1971); McBean and Elliott (1975); Champagne, Friehe, and LaRue (1977); Bradley, Antonia, and Chambers (1981)), deserts (Charuchittipan and Wilson, 2009), lakes (Wuest, Piepke, and Van Senden, 2000), and open ocean environments (Edson and Fairall (1998); Sjöblom and Smedman (2002); Goodman, Levine, and Lueck (2006); Högström et al. (2009)) to deduce the energy balance of local turbulence modulated by the conditions in specific environments. From Zhang (2010), the TKE budget equation valid in the atmospheric surface layer (ASL) is

$$\frac{De}{Dt} = \underbrace{-\bar{u}'w' \frac{\partial \bar{u}}{\partial x} - \bar{v}'w' \frac{\partial \bar{v}}{\partial x}}_{(1)} + \underbrace{\left(\frac{g}{\bar{w}'\theta'}\right) \bar{w}'\theta'}_{(2)} + 0.61\varrho \bar{w}'\bar{a}' - \underbrace{\frac{\partial \bar{w}'e}{\partial z}}_{(3)} - \underbrace{\frac{1}{\bar{e}} \frac{\partial \bar{w}'p'}{\partial z}}_{(4)} - \varepsilon \quad (1.2)$$

where $e = (\bar{u}'^2 + \bar{v}'^2 + \bar{w}'^2)/2$ and the right-hand side terms represent the (1) zonal and (2) meridional shear production, (3) dry and moist buoyancy production, (4) turbulent transport, (5) non-hydrostatic turbulent pressure work, and (6) dissipation rate of TKE, respectively. A generalized schematic diagram of fluid flow over a flat plate, labeled with structural features of turbulence in boundary layers is shown in Figure 1.1 (c.f. Figure 2.2, Schlichting, 1979).

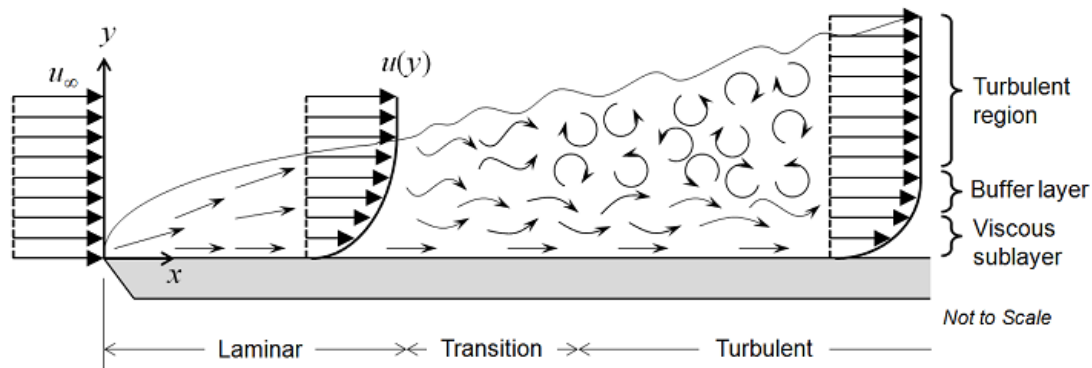


Figure 1.1 Fluid flow over a flat plate, with vertical profiles of velocity $u(y)$ labeled in laminar, transition, and turbulent regions of the flow. Adapted from Schlichting

(1979).

The viscous sublayer, and turbulent layers depicted in Figure 1.1 are regions governed by the dominance of viscous (molecular) and turbulent shear stress, respectively. A buffer layer separates these regions, however the thickness or existence of a viscous sublayer impinges upon the fluid flow properties and structure or roughness of the boundary or wall. Monin-Obukhov similarity theory (MOST; Monin and Obukhov, 1954) takes the physical concepts from Figure 1.1, in which the behavior of turbulence is described by creating universal functions of normalized variables and depends upon vertical distance from the wall or boundary. The Obukhov length L_ζ is a length scale that defines the height z at which shear and buoyancy forces, which act to produce or suppress TKE, are equal – it is defined,

$$L_\zeta = -\frac{\bar{\theta} u_*^3}{g \kappa \bar{w}' \bar{\theta}' + 0.61 g \bar{w}' q'} = \frac{\bar{\theta}_v u_*^3}{g \kappa \bar{w}' \bar{\theta}'_v} \quad (1.3)$$

where $\kappa = 0.41$ is the von Karman constant, θ is the potential temperature, g is the gravitational acceleration, u_* is the frictional velocity, and q is the specific humidity at saturation. Moist and dry thermodynamics can be combined here and potential temperature and humidity can be replaced with the virtual potential temperature θ_v .

Normalizing the TKE budget terms in (1.2) by multiplying them by the inverse shear production $\kappa z u_*^{-3}$ was standard practice in early studies (Wyngaard and Coté (1971); McBean and Elliott (1975); Caughey and Wyngaard (1979); Frenzen and Vogel (1992) and others) to characterize the budget terms in the context of Monin-Obukhov stability $\zeta = z L_\zeta^{-1}$. More recently, investigators have acknowledged the potential role of wave-induced effects, and reaffirmed the invalidity of MOST in the wave boundary layer (WBL;

Edson and Fairall, 1998). This WBL is a boundary layer adjacent to the air-sea interface where wave-induced momentum flux is a non-negligible contributor to the total stress (Edson and Fairall, 1998).

The vertical extent of the WBL is directly related to the composition of the surface wave field and has been empirically shown to be of order 0.1 meters in windsea (Drennan et al. 1999) and may exceed 10 meters height in swell conditions (Sjöblom and Smedman, 2002). Thus, in swell conditions where wave induced pressure-velocity correlations are significant (Drennan, Kahma, and Donelan (1999); Drennan et al. (2003)), velocity profiles in the near surface atmosphere may be altered and no longer conform to the logarithmic layer paradigm dictated by MOST. Hara and Sullivan (2015) recently implemented a TKE budget valid in the WBL as part of a large eddy simulation (LES) of wind over a strongly forced sinusoidal wave train, wherein (1.2) becomes,

$$\frac{De}{Dt} = -\tau_{i3} \underbrace{\frac{\partial \bar{u}_i}{\partial z}}_{(1)} + \left[\underbrace{\frac{g}{w' \theta_v}}_{(2)} - \underbrace{\frac{\partial}{\partial z} (\overline{w' e})}_{(3)} \right] \underbrace{\tilde{v}^2}_{(4)} \quad (1.4)$$

based on a triple decomposition rather than a Reynolds averaging, expanding a variable (e.g. zonal velocity u_1) such that $u_1(t, z, \phi) = \bar{u}_1(z) + u'_1(t, z) + \tilde{v}$ includes horizontal time mean, turbulent fluctuations and wave-coherent fluctuations.

As with (1.2), in (1.4) terms (1) and (2) collectively are the shear production of TKE, and (3) is the buoyancy production of TKE. In the WBL, the surface wave field induces pressure fluctuations on either side of the air-sea interface proportional to the surface area of the waves and coherent with subsequent wave-induced vertical velocity perturbations. Hence, in (1) the wind stress (or momentum flux) $\tau_{i3} = \bar{\tau}'_{i3} + \tilde{\tau}$ includes turbulent stress and wave-induced stress. The transport term (4) includes TKE flux due to

turbulent vertical velocity fluctuations, TKE flux due to wave-induced vertical velocity fluctuations, and wave-induced skin drag. In a similar way, the pressure work term (5) includes the turbulent pressure transport and the wave-induced form drag.

Hara and Sullivan (2015) found wave-induced stress is enhanced at the expense of turbulent stress and TKE dissipation rate for roughness scaled height above the air-sea interface $k\zeta_z < 0.15$ very near the water surface (where $k\zeta_z$ is the non-dimensional product of wavenumber and a sinusoidal wave-following vertical coordinate, see Hara and Sullivan 2015 Eq. 46), while the opposite trend was observed at roughness heights $0.15 < k\zeta_z < 0.7$ above that. Therefore, although turbulent and wave-induced stress both contribute to shear production of TKE, the magnitude of these stresses acting against the mean wind shear increases and decreases with roughness height from the water surface, respectively. Buoyancy production of TKE is enhanced in weakly stratified, warmer, less dense surface layers where fluid is less viscous and more easily mixed.

Consequently, TKE production in surface layers adjacent to a wavy air-sea interface is optimized when long, steep waves are subject to moderate winds resulting in large wave-induced stress near the surface and large turbulent stress especially downwind of wave crests in regions where air-flow separation, sheltering, and enhanced vorticity occur. These features can be seen in images of the velocity fields above laboratory surface waves in Figure 1.2, captured using laser-induced fluorescence (LIF) and particle image velocimetry (PIV) camera techniques by Buckley and Veron (2017).

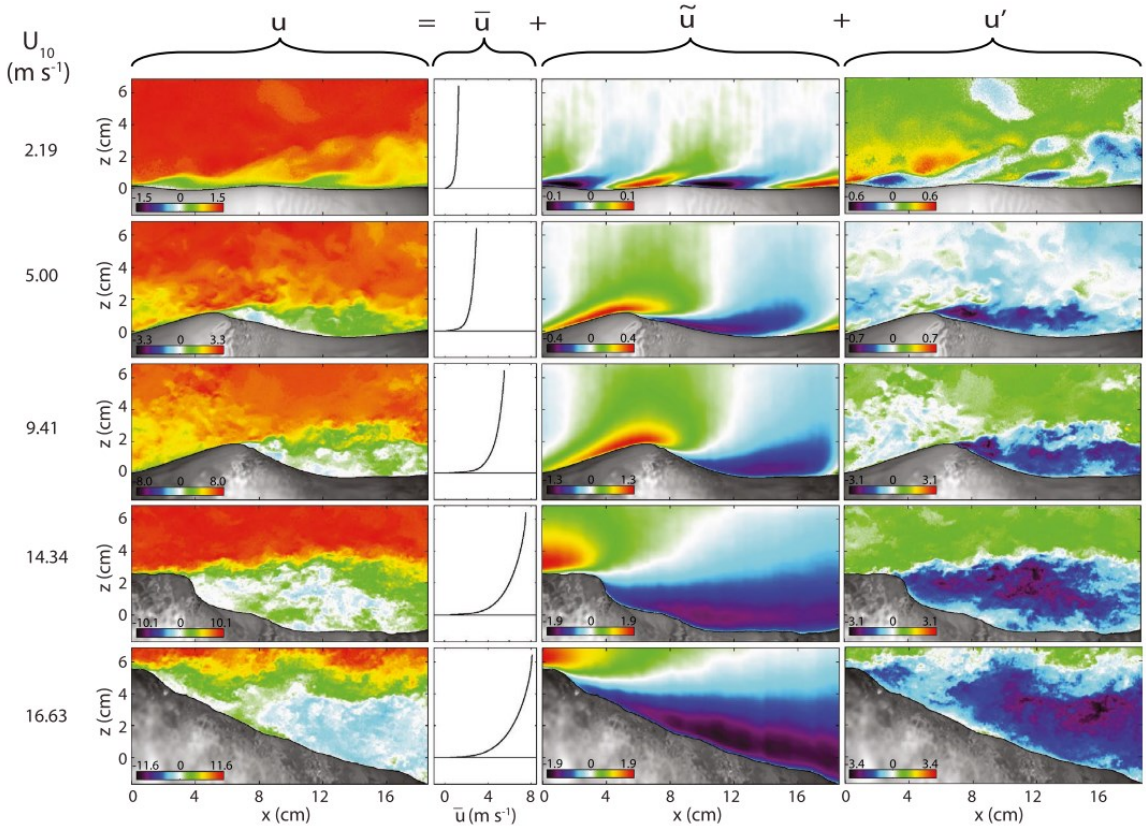


Figure 1.2 Examples of the triple decomposition of instantaneous velocity above laboratory waves captured using LIF and PIV cameras into mean, turbulent, and wave-coherent contributions. All quantities are plotted in meters per second. Wind speed increases from the upper-most row to the bottom-most row. Figure source: Buckley and Veron (2017), Figure 7.

TKE is also intuitively present and important in the ocean surface layer, as a result of momentum fluxes from turbulent and wave-induced stresses at the air-sea interface. Lakes, oceans, and other water bodies however are bounded in depth and have complex bathymetry that results in bottom friction, for example, that influences the profile of velocity and thereby kinetic energy in water columns. Nevertheless, TKE flux into water bodies contributes to horizontal and vertical mixing, near-surface currents, internal waves, and biochemical processes, which have important consequences for euphotic zone biology and global climate (e.g. nutrient and gas concentrations, gas transfer, photosynthesis).

As a result of water density differences compared to the atmosphere, the vertical

transport, pressure work, and dissipation rate terms of the TKE budget are particularly contextually important in this domain. Some of the first measurements of sub-surface TKE and its dissipation were made in the early 1960s by H.L. Grant and R.W. Stewart; making estimates near the sea surface at depths 1-15 meters over winds 7-10 meters per second, dissipation rate was found to have “weak dependence on depth” near the surface and to increase with wave height. Measurements from a hot-film flow-meter however, were 0.4-7 times larger than the expected theoretical “law of the wall” values determined via inertial dissipation method (Stewart and Grant, 1962).

Subsequent studies have measured TKE dissipation rates consistent with “law of the wall” (Arsenyev et al. 1975; Dillon et al. 1981; Oakey and Elliott 1982; Soloviev, Vershinsky, and Bezverchnii 1988), while others have found higher rates of dissipation inconsistent with log-layer predictions (e.g. Kitaigorodskii et al. 1983; Gregg 1987; Gargett 1989). Dissipation rate observations supporting the ‘inverted log-layer’ ocean surface layer have however been made in lighter winds or at greater depths (i.e. not very near the surface; Terray et al. 1996).

Tower-based and ship-based measurements have confirmed the presence of higher dissipation rates in this very-near-surface region (Agrawal et al. (1992); Drennan et al. (1996); Terray et al. (1996)). Enhancement of dissipation very near the surface has been attributed to both wave breaking (Osborn et al., 1992) and wave-current interaction related to the Stokes’ drift (Langmuir turbulence; e.g. Stips et al. (2005)); at high wind speeds the rate of wind stress on the waves was found to be consistent with depth integrated water-side TKE dissipation, with the inference that most of the energy flux to waves is reaching the water by the process of wave breaking (Drennan et al., 1992).

Aside from determining the dominant mechanism for energy loss from the surface wave field (e.g. Sutherland and Kendall Melville (2015)), other studies have reported evidence of how the TKE budget terms balance in the near-surface ocean; Craig and Banner (1994) for example, using 1-D model experiments, found that the downward flux of TKE (transport) balances dissipation in a wave-enhanced sub-surface layer; beneath this wave-enhanced layer, a transition to classical law-of-the-wall behavior (shear balanced by dissipation) is observed to occur rapidly.

Indeed, other investigators have carried out scaling of TKE budget terms on the water side based on normalized timescales (e.g. Melville, Veron, and White (2002); Drazen and Melville (2009); Savelyev, Maxeiner, and Chalikov (2012)), typically related to wave breaking. Drennan et al. (1996) used open ocean ship-board measurements to calculate the sub-surface TKE dissipation rate during the Surface Waves Dynamics Experiment (SWADE) and their results relative to classical wall-layer theory are shown in Figure 1.3, clearly demonstrating the effect of wave-induced stress and breaking in enhancing sub-surface turbulence and dissipation.

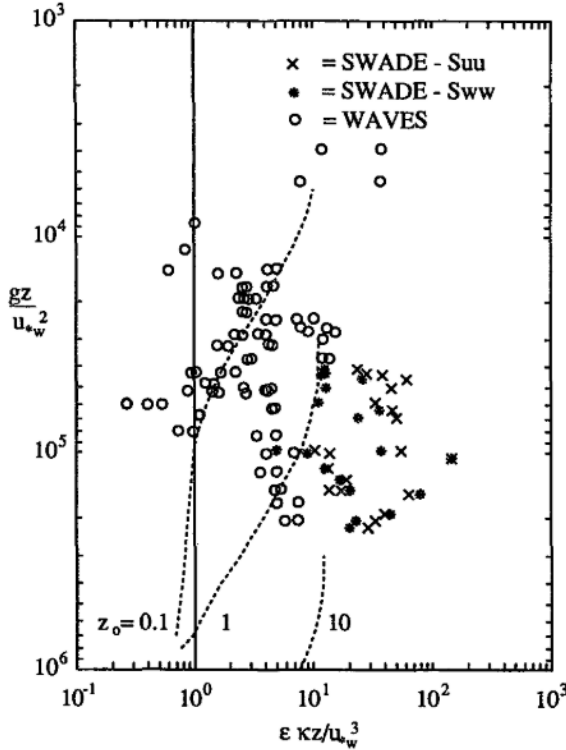


Figure 1.3 Dissipation rate versus depth in the wall-layer coordinates of Soloviev et al. (1988). The vertical line represents the result of wall layer theory: $\varepsilon = u_{*w}^3 / \kappa z$. The three dashed lines represent the predictions from the model of Craig and Banner (1994) for roughness lengths of 0.1, 1.0, and 10 meters with $\alpha = 100$. Other parameters in the Craig and Banner model are as in their Table 1. Figure source: Drennan et al. (1996), Figure 4.

Although not explicitly decomposed as such in (1.4), the dissipation rate of TKE responds to both turbulent and wave-induced TKE production, which have associated spatial and temporal scales and therefore as is suggested by Drennan et al. (1996) and others, appropriate estimation of TKE and its' dissipation requires inclusion of wave-coherent forces and wave-induced stresses where appropriate. A careful description of the measurement techniques and mathematical formalism for TKE dissipation rate is given in the next section.

1.1.2 Dissipation rate of TKE

The dissipation rate of TKE is fully described by the viscous dissipation tensor,

$$\varepsilon_{ij} = 2\nu \frac{\overline{\partial u'_i}}{\partial x_j} \frac{\overline{\partial u'_i}}{\partial x_j} \quad (1.5)$$

where ν is the kinematic viscosity and $i, j = 1, 2, 3$ across velocity components and spatial directions. From the reporting of the Kansas turbulent kinetic energy budget experiments (Wyngaard and Coté, 1971) to the present, predominantly two methods have been used to determine the TKE dissipation rate: direct (e.g. Wyngaard and Coté (1971); Bradley, Antonia, and Chambers (1981); Goodman, Levine, and Lueck (2006)), and spectral (e.g. Champagne, Friehe, and LaRue (1977); Edson and Fairall (1998); Albertson et al. (1997)). Each of these makes assumptions regarding the turbulent flow, in particular that the turbulent flow is locally isotropic, and that invoking Taylor's hypothesis of frozen turbulence is acceptable. The assumption of isotropy is made to reduce the complexity of (1.5).

Taylor's hypothesis of frozen turbulence (c.f. Taylor, 1938) states that if the assumption is made that advection contributed by turbulent circulations themselves is *small*, then the advection of a field of turbulence past a fixed point can be taken as entirely due to the mean flow; such turbulence is theoretically not statistically changing during the advection process, hence for $U \gg u$,

$$u = \phi(t) = \phi\left(\frac{x}{U}\right) \quad (1.6)$$

In the context of the direct computation of dissipation rate, (1.5) is therefore reduced to

$$\varepsilon = 2\nu \left(\frac{\overline{\partial u}}{\partial x} \right)^2 = 2\nu \left(\frac{1}{\bar{U}} \frac{\overline{\partial u}}{\partial t} \right)^2 \quad (1.7)$$

Using an indirect approach based on turbulent velocity spectra, the dissipation rate is derived by rearranging the Kolmogorov (1941) equation for the turbulent energy spectrum $S(k) = \alpha \varepsilon^{2/3} k^{-5/3}$ such that

$$\varepsilon = \alpha^{-3/2} \frac{2\pi f}{U} [fS_{uu}(f)]^{3/2} \quad (1.8)$$

where α_u is the one-dimensional Kolmogorov constant whose value varies across literature (e.g. $\alpha_u = 0.5$ in Sreenivasan, 1995) and $S_{uu}(f)$ is the zonal velocity spectrum constructed using a Fourier transform of a zonal velocity timeseries $u(t)$. In (1.6), (1.7), and (1.8) U is the advection velocity, or velocity at which turbulence is advected past a particular measurement site or location. In (1.8), the dissipation rate has been transformed from wavenumber to frequency space via $k = 2\pi f U^{-1}$ by invoking Taylor's frozen turbulence hypothesis.

Kolmogorov's depiction of the turbulent energy spectrum $S(k)$ includes three distinct spatial scales pertaining to the evolution of turbulence. These three scales are the integral, inertial or equilibrium, and viscous or dissipation scales and they separate the spectrum into sub-ranges. The dissipation rate of TKE in (1.8) is only valid over a viscosity-independent section Δk of the turbulent spectrum, the inertial sub-range, which is isotropic and conforms to the expected theoretical slope of $k^{-5/3}$. Isotropy can be ascertained by comparing ratios of velocity spectra $R = S_{x_i x_i} / S_{x_j x_j}$ to Kolmogorov theory for convergence to the theoretical ratio expected between zonal and vertical velocity spectral density, $R_c = 4/3$ (Pope, 2000).

The inertial sub-range, or equilibrium range of the spectrum exists where the supply of injected turbulence at larger scales maintains equilibrium with losses of turbulence to dissipation at viscous scales. Such conditions remain valid when transformation to frequency space f is performed. The energy spectrum and turbulent cascade for 3D turbulence is given in Figure 1.4.

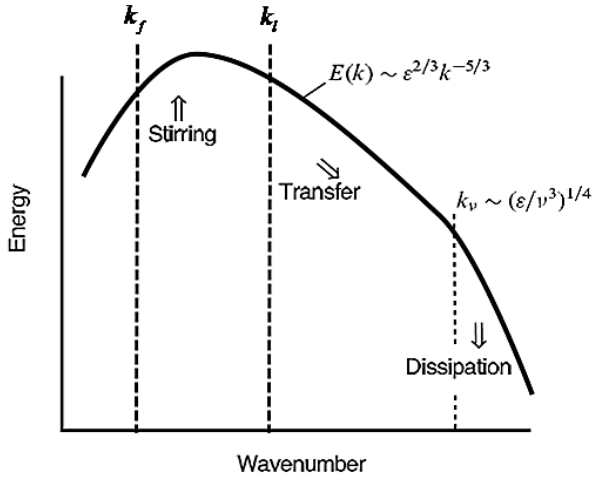


Figure 1.4 Turbulent energy spectra and subsequent energy cascade for 3D turbulence. Figure source: Vallis (2006), Figure 8.3.

In Figure 1.4, Kolmogorov length scales k_f and k_i bound the energy-containing or integral sub-range while the inertial sub-range exists between integral and viscous length scales k_i and k_v , respectively. The dissipation rate of TKE therefore increases via (1.4) where advection velocity U is smaller but still sufficiently large to satisfy frozen turbulence, and increases as the integrated energy beneath the curve across Δk increases. This integral theoretically takes a greater value when the slope of $E(\Delta k)$ increases as a result of for example, wave-induced stress in the WBL injecting energy at inertial scales (Ortiz-Suslow, et al. 2019).

1.1.3 Sea surface structure evolution

The sea surface is a complex, multi-scale, unsteady density surface composed of spatiotemporally varying roughness elements viewed collectively and contextually according to physical forcing and inherent fluid properties. The roughness elements are predominantly waves of different scales and physical regimes. The scale and roughness of waves determines the magnitude and means of influence on turbulence in the adjacent atmospheric surface layer and ocean via shear, stratification and mixing, pressure perturbations, and so forth (Phillips, 1977; Young, 1999).

Additionally, wave scales dictate the penetration depth of entrained air bubbles, the intensity of breaking-induced turbulence, the length scale of orbital oscillations associated with Stokes drift, and the magnitude of sub-surface Eulerian currents (Andrews and McIntyre, 1978; Craik, 1982; McWilliams et al. 2004). Small-amplitude or linear water-wave theory (e.g. Airy, 1845; Stokes, 1847; Dean and Dalrymple 1984) allows for a description of the sea surface structure in terms of individual waves according to conservation of waves (or mass) and relationships between their wavenumber and frequency. To third order, this dispersion relationship is

$$\omega^2 = \underbrace{gk}_{\text{gravity}} + \underbrace{kh}_{\text{capillary}} + \underbrace{k^3}_{\text{nonlinear}} - kh \quad (1.9)$$

which includes terms for waves in (1) gravity and (2) capillary regimes or a combination thereof. By solving (1.9) using the known wavenumber k , water depth h , water density ρ , and surface tension σ , for any wave a theoretical wavelength L , phase speed c , wave period T , and angular wave frequency ω can be calculated.

The regimes described by (1) and (2) are determined by the scale, and thus, restoring force of the waves. For small-scale or very short waves on the order of millimeters

to few centimeters, k is large and capillary action and surface tension between water molecules is significant to the integrity and evolution of the wave. For waves of smaller k , capillary forces either play a negligible role or act in combination with gravity g to restore waves against forcing. The aspect ratio kh determines whether waves behave as deep, intermediate, or shallow (non-dispersive).

The wave energy balance equation is used in air-sea coupling and wave modeling implementation to provide wave conditions in space and time based on physical processes that facilitate wave growth, nonlinear wave-wave interactions, and wave dissipation. In effect, this budget combines the sources, sinks, and physical methods of redistribution of wave energy in wavenumber and directional space via

$$\frac{\partial E}{\partial t} = \underbrace{S}_{(1)} + \underbrace{D}_{(2)} + \underbrace{N}_{(3)} - \underbrace{E}_{(4)} - \underbrace{F}_{(5)} \quad (1.10)$$

where $E(k, \phi)$ is the directional water surface elevation (or wave) spectrum, (2) is the wind input, (3) the non-linear interaction term, and (5) is wave energy dissipation. The remaining term (4) contains the advection of wave energy and can be expanded as

$$-\nabla \cdot (c_g E) = - \left[\underbrace{\frac{\partial E(c_g \cos \phi + u_c)}{\partial k}}_{(1)} + \underbrace{\frac{\partial E(c_g \sin \phi + v_c)}{\partial \phi}}_{(2)} \right] + \underbrace{\frac{\partial (kE)}{\partial k}}_{(3)} + \underbrace{\frac{\partial (\phi E)}{\partial \phi}}_{(4)} \quad (1.11)$$

with (1) the horizontal advection of wave energy at group velocity plus local Eulerian current velocity, (2) advection in wavenumber space, and (3) wave refraction (Donelan et al., 2012). Momentum flux from wind to waves provides the source for wave energy S_{in} in (1.10), the magnitude of which is contingent upon the relative directions of wind and wave propagation as well as the relative wind speed and wave phase speed.

The rate of wind input to waves F in terms of wave growth rate β across the entire directional wave spectrum S_η was computed by Drennan et al. (1996) and Terray et al. (1996) from ship and fixed platform measurements using

$$F = g \int \int \beta(\omega, \theta) S_\eta(\omega, \theta) d\omega d\theta \quad (1.12)$$

where β is the wave growth rate. According to Donelan and Plant (2009), the two most common parameterizations for wave growth rate are $\beta = 0.04 u_*^2 \omega c^{-2}$ (Plant, 1982) and

$$\beta = 0.194 \frac{\rho_a}{\rho_w} \left(\frac{U_{L/2} \cos \theta}{c(k)} \right) \left| \frac{U_{L/2} \cos \theta}{c(k)} \right| \omega \quad (1.13)$$

coming from Donelan and Pierson (1987). Both growth rates involve a ratio of momentum flux or wind stress and a wave phase speed term as well as an empirical coefficient for wave sheltering (Jeffreys 1924, 1925). The sheltering coefficient has been determined from laboratory and field measurements across a variable range of values 0.12-0.28 (Hsiao and Shemdin, 1983; Donelan, 1999; Donelan et al. 2006) however an exact parameterization is a matter of choice and research is ongoing to properly characterize the physics.

The ratio of wind speed at half-wavelength and wave phase speed $U_{L/2} \cos \theta c^{-1}(k)$ is a proxy for inverse wave age for each wavenumber k and at each wind-wave direction θ such that wave growth is large when wind and waves are directionally aligned and waves propagate at speeds slower than the wind speed. Since (1.13) is sign-preserving, negative growth can result when swells propagate against the wind direction.

Breaking is the consequence of destabilization of the physical structure of a wave and is typically forced by topography, large momentum flux or wind stress, or the consequence of constructive wave-current or wave-wave interactions. Breaking may be intermittent and relatively gentle (as in microbreaking or spilling), or abrupt and violent as with plunging

or surging waves. Regardless, wave energy is lost to turbulence or by viscosity depending on the length scale of the waves and timescale of the breaking event (Phillips, 1977; Donelan and Plant, 2009). A series of side-looking mounted camera images capturing the spilling and plunging breaking of wind-forced mechanically driven paddle waves modeled after an open ocean wave spectrum observed during the JOint North Sea WAves Project (JONSWAP; Hasselmann et al. 1973) in the University of Miami SURge STructure Atmosphere INteraction (SUSTAIN) wind-wave tank are shown in Figure 1.5.

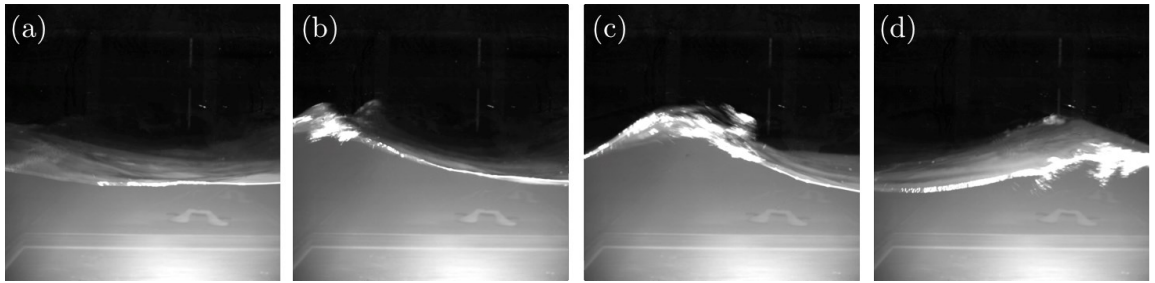


Figure 1.5 Side-looking mounted camera images of bottom-illuminated waves in the SUSTAIN wind-wave tank. Imaging commenced at 50 frames per second, though images here are of order 1 second apart. (a) Forward crest of wave approaching from left with microbreaking or light spilling on the crest itself (b) Tips of wave crest destabilizing, directional spreading is noticeable (c) Wave crest plunges and breaks, with spray globules and detachment near the crest (d) Breaking-induced entrainment and bubble plumes seen trailing slightly behind the crest and downward. Disruption of the smooth interface by breaking and wall friction increase the scattering and therefore, brightness of the aforementioned features.

Bubbles and sea spray are vehicles for the exchange of heat, momentum, fluid properties, surfactants and aerosols, which directly result from momentum flux from wind to waves and wave breaking across a variety of scales (Gemmrich, 2010). Bubbles, in particular, have been observed on and below the water surface of lakes, coastal areas, and oceans in light and extreme wind conditions for decades (Blanchard and Woodcock, 1957; Thorpe, 1982; Deane and Stokes, 2002 among others). A short history of bubble observations and the wave-driven and environment-driven physics and forces governing bubble dynamics is given in the next section.

1.1.4 Bubble production and governing physics

Bubbles are a captivating visual cue of processes intrinsic to the evolving sea surface and an important participant in air-sea exchanges. A complete understanding of bubble dynamics and behavior remains elusive, but is imperative to quantifying gas transfer and improving climate and hurricane numerical models (Stanley et al. 2009; Brumer, et al. 2017). Intermittent destabilization of the sea surface results in wave breaking events that entrain air and generate turbulence. This turbulence fragments the initial volume of air into groups or plumes of bubbles (Holthuijsen and Herbers, 1986; Gemmrich, 2010). Bubbles have been observed and studied in the field and laboratory for decades (Blanchard and Woodcock, 1957; Medwin 1970; Johnson and Cooke, 1979; Thorpe 1982; Deane 1997).

Such research has revealed bubbles' diverse role in air-sea interactions – namely, altering sub-surface optical properties (Medwin, 1977), scattering sound (Osborn, et al. 1992; Deane 1997), contributing to marine aerosol production (Gemmrich et al. 1999b) and enhancing air-sea gas flux (Kanwisher, 1963; Broecker and Siems, 1984; Jaehne and Monahan, 1995; Brumer et al. 2017). Since the earliest studies, size distribution has been observed to be the most important quantifiable property of a bubble population (Deane and Stokes, 2002). Bubble size distributions have an initial or acoustically active period and subsequent, more quiescent period of evolution associated with the forces creating and maintaining bubbles of size r at depth z considering any time t . A logarithmic timeline of bubble plume evolution and associated bubble plume images from Deane and Stokes (2002) is shown in Figure 1.6.

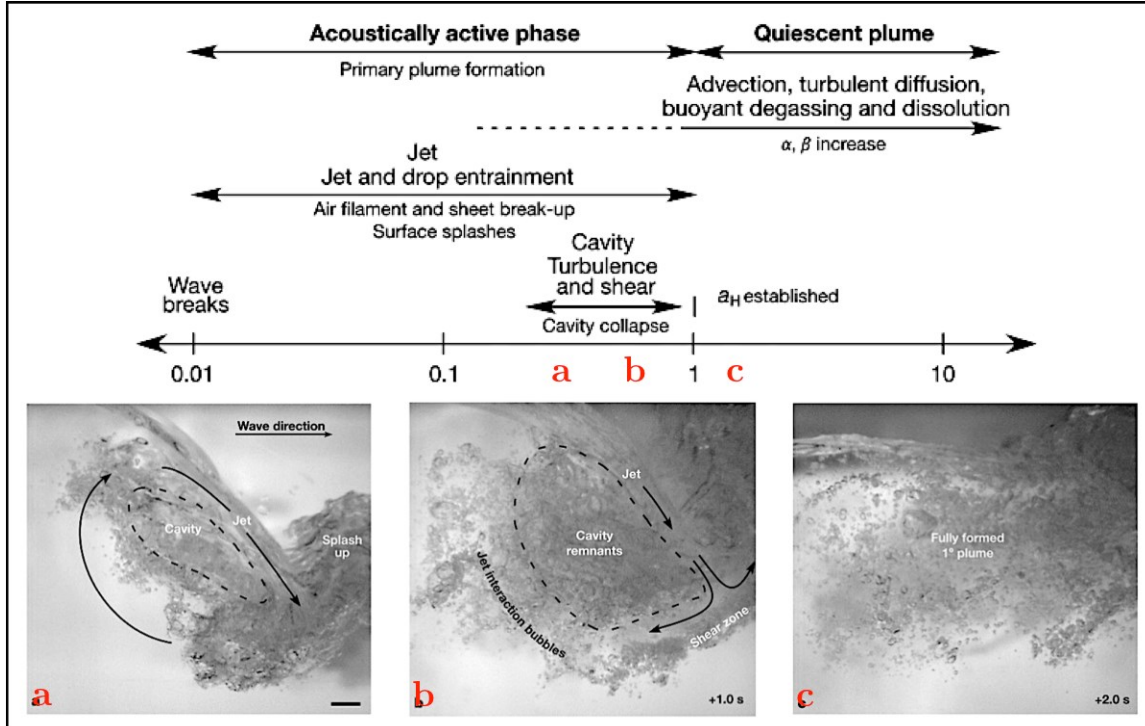


Figure 1.6 Logarithmic (in seconds) of bubble plume evolution showing the acoustic (formation) phase and the quiescent (evolution) phase. (a) Collapse of wave crest air cavity and jet intrusion at the forward edge of the collapsing crest 0.49s after wave breaks (b) Cavity collapse continues, showing associated breaking-induced shear and turbulence. (c) Establishment of bubble plume and initial bubble size distribution complete at about 2s after wave breaks. Figure source: Deane and Stokes (2002).

The initial size distribution of a bubble population is the direct result of wave breaking, which occurs across the wave spectrum at different frequencies and with varied intensity (Gemmrich, 2010). The steepness of wave crests, influence of sub-surface bathymetry, the angle between wind and waves, and frequency of occurrence of breaking all moderate wave breaking and therefore the creation of bubble populations. Visible entrainment is common, but not always observed, and while microbreaking may not lead to the entrainment of large air volumes it disrupts the surface skin and molecular boundary layer which can enhance air-sea gas exchange.

Turbulence induced by wave breaking results in the discrimination of the entrained air volume into a number of bubbles of different radius, eccentricity, and void fraction,

defining the bubble population. Once created, bubbles are subject to horizontal (or advection), vertical (or buoyancy-driven) and omni-directional forces that act proportional to the bubble radius. Horizontal forces include advection of bubbles by the mean Eulerian current, Stokes drift, and the initial horizontal velocity of the bubble itself. Vertical forces include buoyancy subject to void-fraction and initial downward momentum subject to wave steepness and breaking intensity.

Surface tension, shear turbulence, and pressure work associated with the sea surface wave field represent forces that act over all facets of the bubble surface (i.e. they are omni-directional). Surface tension acts on molecular scales to maintain the bubble structural integrity against shear or pressure-induced deformations to the shape or size of the bubble; such deformations occur naturally also as a bubble grows via rectified diffusion. This rectified diffusion results in a net mass influx to bubbles below a critical unstable radius. Surface tension and pressure work forces are altered by the ambient water conditions as well, specifically by water density; it has been clearly demonstrated in earlier studies that water impurities (increased salinity) and warmer water temperatures weaken surface tension and result in the production of more bubbles and sea spray (Monahan, 1967; Slauenwhite and Johnson, 1999). Water density also has a substantial influence on bubble injection depth (Hwang et al. 1991). The Weber number quantifies the balance of disruptive turbulent forces and the restoring force of surface tension pertaining to bubbles – it is,

$$We = (\rho_w / \gamma) u^2 d \quad (1.14)$$

where ρ_w is the water density, γ is the fluid surface tension, u^2 is the turbulent kinetic energy on the scale of the bubble, and d is the bubble diameter.

Bubble fragmentation occurs for any bubble when (1.14) exceeds a critical value subject to the flow conditions – typically between 3-4.7 based on laboratory experiments (Lewis and Davidson, 1982; Martinez-Bazan, et al. 1999; Deane and Stokes, 2002). A now well-known fluid dynamics study of globule splitting and deformation by J.O. Hinze (1955) derived a formula including (1.14) determining the maximum size a bubble can achieve prior to fragmentation – the so-called ‘Hinze’ scale,

$$a_H = 2^{-8/5} \varepsilon^{-2/5} \left(\frac{\gamma We_C}{\rho_w} \right)^{3/5} \quad (1.15)$$

where a_H is the Hinze scale in meters, ε is the TKE dissipation rate, γ is the fluid surface tension, We_C is the critical Weber number (where 1.14 takes a critical value), and ρ_w is the water density as in (1.14). A table of values for a_H is given in Figure 1.7, reported in millimeters, for laboratory and field environments.

Study	Energy (J m^{-2})	U_{10} (m s^{-1})	a_H (mm)	Location
Present	50	—	1.3–1.6	Laboratory
Leifer and de Leeuw (2006)	18	10	1–1.7	Laboratory
Blenkinsopp and Chaplin (2010)	—	—	0.9–1.2	Laboratory
Deane (1997)	3000	—	0.7	Surfzone
Deane and Stokes (2002)	2000–7000	7–10	1	Open ocean
Bowyer (2001)	5000	10	0.7–1	Open ocean

Figure 1.7 Table of Hinze scale values based on laboratory, surf zone, and open ocean data from the respective publications. Figure source: Deane et al. (2016)

Surface tension is an effective molecular elasticity in which turbulent perturbations in pressure and/or pressure gradient relative to the physical boundary of the fluid or bubble act over the length scale (a radius or radius of curvature) of the fluid, bubble, or boundary surface; naturally therefore, a spherical shape has internal and external pressure in balance

and is the preferred natural configuration for entrained air suspended in a liquid medium. Mathematically, the surface tension is,

$$\gamma = \frac{\Delta p}{2} r \quad (1.16)$$

where the pressure gradient $\Delta p = p_i - p_o$ describes the force balance acting azimuthally outward and physically represents the mass flux tendency. The necessary condition for bubble survival is that $\Delta p \geq 0$ where

$$p_i = \rho_a R_g T \quad (1.17)$$

is the internal pressure of the bubble which acts outward in all directions, governed by entrained air density ρ_a , universal air gas constant R_g , and T is the air temperature. The external pressure acting downward in all directions is,

$$p_o = \rho_w g (-z + \eta K_p(z)) \quad (1.18)$$

which includes the hydrostatic pressure $-\rho_w g z$ and the dynamic pressure modulated by the pressure response factor $K_p(z) = \cosh k(h+z) / \cosh kh$ (Dean and Dalrymple, 1984). If $\Delta p < 0$, pressure forces induced by depth and wave-induced pressure perturbations at wavelength scales crush or implode bubbles. A schematic of the time-varying evolution of bubbles in the context of these pressure forces is shown in Figure 1.8, adapted from Abbas, et al. (2013).

Bubbles undergo rarefaction beneath surface wave troughs and compression beneath surface wave crests dependent on wave height and wavelength. Compressions (rarefactions) are associated with diffusive outgassing (ingassing) that result in a net gain in bubble size due to the bubble surface area to volume ratio beneath surface wave troughs (Leong et al., 2010).

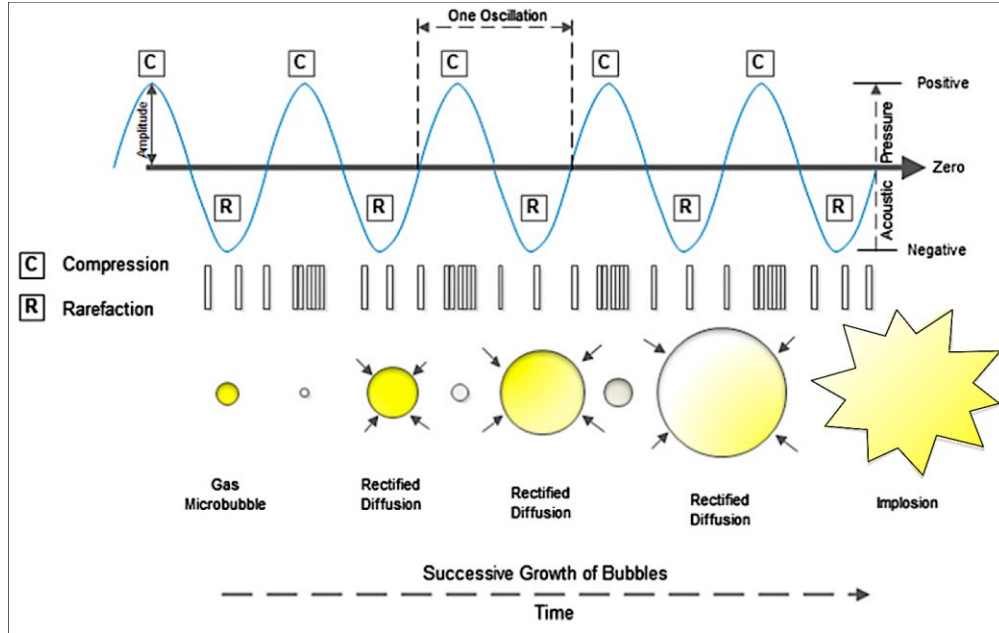


Figure 1.8 Schematic depiction of growth and collapse of bubble in acoustic cavitation. The blue sinusoidal curve physically represents the air-sea interface in terms of the various sea surface structures (waves). Figure source: Abbas et al. (2013)

Through (1.13) and (1.14), bubble size distributions regardless of the environment in which they are observed, are explicitly linked to sub-surface TKE dissipation, sea surface structure evolution, and ambient water properties such as water density and surface tension. Bubble populations therefore provide multi-scale evidence of sea surface wave structure, breaking prevalence, and the scales and magnitude of turbulence resulting from wave breaking events. Furthermore, the ambient air and water conditions are also reflected in the observed bubble distribution through the Hinze scale and vertical distribution of bubbles. For absolute clarity and to unify this review of relevant subjects, a bulleted list of the research objectives to be addressed in this dissertation is given in the following section.

1.2 Motivation and research objectives

The air-sea interface is a fundamentally important dynamical boundary in regards to the balance and physical exchange of energy between the atmosphere and ocean; these exchanges are accomplished by mechanical and thermodynamic processes that transfer,

redistribute or dissipate the energy. Fluxes of heat and momentum through and at the interface contribute energy to large-scale phenomena such as convection, hurricanes, wave growth, surface ocean currents, and mixing to name a few (Emanuel (1986); Liu and Wang (2013); Melville (1996)). However, physical processes occur on smaller time and space scales that are simultaneously important to the dynamics of these large-scale phenomena and often difficult to measure or model.

Unsteady, inhomogeneous wind forcing and viscosity at the air-sea interface results in rapidly evolving, transient turbulent motions, and turbulent kinetic energy (TKE). Within the surface and wave-affected boundary layers adjacent to the air-sea interface, the production and re-distribution of TKE are inextricably linked to the vertical structure and stability of these layers and closure of the TKE budget is achieved through dissipation at viscous scales. Given that the forces governing the aforementioned origins of turbulence and its dissipation (wind stress and viscous forces) also provide for the growth and breaking of waves for example, the structure of the sea surface is critically important to the balance and partitioning of energy near and at the air-sea interface.

Although TKE and its dissipation have been experimentally, numerically, and observationally investigated over the past few decades (e.g. Wyngaard and Coté (1971); Bradley, Antonia, and Chambers (1981); Edson and Fairall (1998); Sjöblom and Smedman (2002); Melville, Veron, and White (2002); Drazen and Melville (2009) and many others), there remains disagreement as to the dominant terms in the TKE budget and how they balance under different conditions, limited observations of the budget terms or TKE dissipation have been made in or beneath the surface during extreme, hurricane-force

conditions, and the accurate measurement of TKE dissipation, due to instrumentation limitations and resolution of the necessary scales of motion, has proven difficult.

Therefore, we make use of field data and laboratory experiments to address and alleviate these challenges; specifically, we use turbulence and dissipation measured in low winds within the atmospheric surface layer (Smith, Haus, and Zhang, 2019) and contrast these data with sub-surface laboratory measurements beneath hurricane-force winds. TKE and its' dissipation rate are then explicitly linked to evolution of the sea (water) surface structure in wind-sea, mixed, and swell conditions from the open ocean as well as high-wind breaking-wave laboratory conditions, where spray and bubbles act as vehicles for further TKE flux into layers adjacent to the air-sea interface. In so doing, we ask the following questions:

1. How do turbulent kinetic energy (TKE) and its' dissipation rate behave in the non-hurricane atmospheric boundary layer at different sea states and roughnesses? Can dissipation rate be parameterized in terms of a physically constrained sea state or drag?
2. How do bubble size distributions vary beneath hurricane-force winds when comparing idealized monochromatic versus open ocean spectrum wave conditions? Can the distributions be parameterized in terms of wave statistics?
3. How do the sea surface wave breaking prevalence and ambient water properties such as temperature influence sub-surface turbulence spectra? Is there evidence of bubble-induced energy injection into turbulent spectra?

Chapter 2: Data and Analysis Methodology

2.1 Data

2.1.1 Field campaign background and objectives

Field data used in this dissertation was collected during the LAgrangian Submesoscale ExpeRiment (LASER). LASER was conducted January–February 2016 by investigators from the Consortium for Advanced Research on Transport of Hydrocarbons in the Environment (CARTHE) group, as part of the Gulf of Mexico Research Initiative (GoMRI) to investigate marine, biological, and physical effects of the *Deepwater Horizon* (DWH) oil spill (2010).

LASER was motivated by data and preliminary findings on near-surface ocean transport from large-scale currents and eddies to submesoscale fronts, collected during the Grand Lagrangian Deployment (GLAD) experiment in August 2012 (e.g., Olascoaga et al. 2013; Poje et al. 2014; Beron-Vera and LaCasce 2016). Material transport remains difficult to predict due to complex dynamical interactions between multi-scale processes that challenge existing model resolution and parameterization constraints.

LASER combined surface drifter deployments, regional scale modeling, aerial observations, and small boat operations with the goal of improving knowledge and understanding of the fate of the spilled crude oil and predicting its transport in future spill events. Figure 2.1a shows the study region overlain with the vessel track of the R/V *F.G. Walton Smith* (*FGWS*), operated by the University of Miami Rosenstiel School of Marine and Atmospheric Sciences (RSMAS).

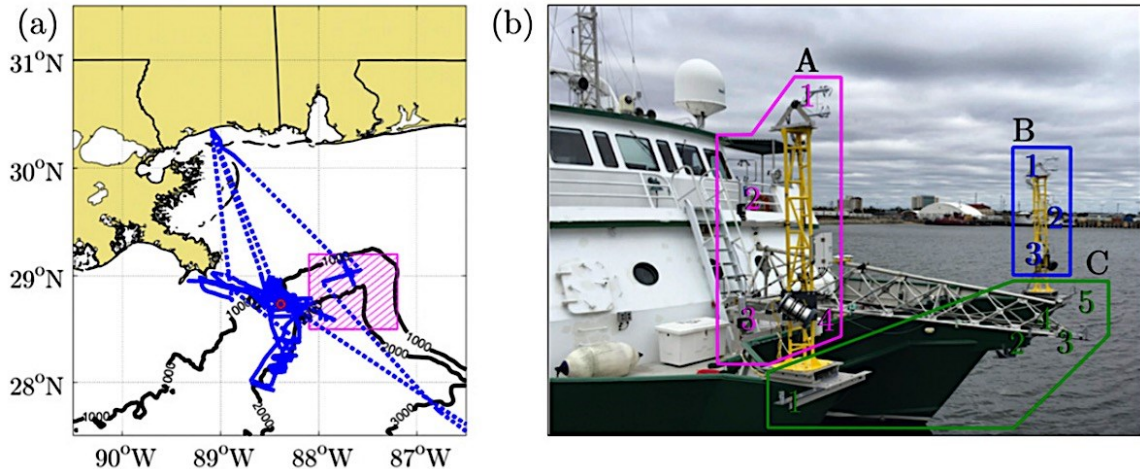


Figure 2.1 (a) Primary site for the LASER experiment in the Gulf of Mexico. Solid blue lines show the recording periods and track of R/V *F.G. Walton Smith*. The red circle is the location of the *Deepwater Horizon* oil rig. The magenta hatched square shows the location of the DeSoto Canyon region. Black contours with numbers are the isobaths in meters. (b) Bow instrumentation on R/V *F.G. Walton Smith* during LASER. Group A (B) refer to the starboard (port) flux towers, equipped with IRGASON and RM Young sonic anemometers and a Rotronic relative humidity/air-temperature (RH/AT) sensor numbered in that order on each tower. Group C refers to the array of five Senix ultrasonic distance meters (UDMs).

2.1.2 Ship data

Surface-layer atmospheric and both in-situ and remote surface ocean measurements were collected on *FGWS* using a combination of fixed-mount digital sensors, direct water sampling instruments, and a marine Doppler radar (MDR). With the exception of port calls and localized maneuvering for small-boat operations as needed, the ship was underway in open ocean with non-zero forward speed $0 < U_{FGWS} \leq 4.67 \text{ ms}^{-1}$ when data were collected.

Figure 2.1b shows the configuration of high-frequency fixed-mount instrumentation on the *FGWS* bow. The vessel bow included two flux towers (one per vessel prow) and a center truss extending outward from the hull directly ahead over open water. A motion measurement package was also installed aboard *FGWS* and included one Columbia Research Laboratory SA-307HPTX accelerometer and three Systron Donner

QRS11 angular rate gyros to measure and correct data for the vessel's roll, pitch, yaw, surge, sway and heave accelerations.

2.1.2.1 Flux towers

The flux towers aboard *FGWS* consisted of two triangular, metal scaffolds affixed each with one Campbell Scientific open-path integrated sonic anemometer-gas analyzer (IRGASON) and two R.M. Young Model 81000 sonic anemometers (RMY). Each sonic anemometer was mounted at a specific height on each flux tower, and measured 3D velocity and sonic temperature at a sampling rate of 16 values per second, or Hertz (Hz). The IRGASON units also measured IR-gas analyzer derived partial pressure concentrations for water vapor and carbon dioxide and absolute air pressure in hectopascals (hPa). The starboard flux tower was additionally equipped with a Rotronic relative humidity and air-temperature sensor (RH/AT) equipped with a radiation and moisture shield for marine use.

2.1.2.2 Ultrasonic distance meter array

An array of five Senix ToughSonic 30 ultrasonic distance meters (UDMs) were arranged in a dual triangular configuration on the *FGWS* bow, with one on each prow and three in smaller triangle on the center truss attached to the bow deck. Each UDM sampled at 16 Hz, providing time-of-flight water surface elevations in meters to a maximum range of 30 feet (9.14 meters). Exact height and location of bow instrumentation and the ship motion measurement package is given in Table 2.1.

Instrument	Fixed-Mount Location	Height (meters)
Motion measurement package (QRS11 and SA-307HPTX)		3.986
CS IRGASON	P	5.950
CS IRGASON	S	5.955

RMY 81000 (lower)	P	4.155
RMY 81000 (upper)	P	5.190
RMY 81000 (lower)	S	4.165
RMY 81000 (upper)	S	5.185
Rotronic RH/AT	S	3.685
Senix TS30 UDM	P	3.150
Senix TS30 UDM	CT-P	3.325
Senix TS30 UDM	CT-O	3.325
Senix TS30 UDM	CT-S	3.325
Senix TS30 UDM	S	3.150

Table 2.1 R/V *F.G. Walton Smith* bow instrumentation heights. For the center column of the table, “P” denotes port prow, “S” denotes starboard prow, and “CT” denotes center truss. For the UDM array, “-O” denotes “outboard”.

2.1.2.3 Microthermosalinograph

A Seabird Scientific SBE 45 microthermosalinograph (MicroTSG) routed surface seawater samples from intakes at the *FGWS* bow to the fore-stern wet laboratory, which provided sea surface temperature (SST), salinity (SSS), and pressure at 6 Hz sampling frequency along the vessel track.

2.1.2.4 Marine Doppler radar

A single X-band Marine Doppler radar (MDR) was mounted above the *FGWS* wheelhouse and can be seen in Figure 2.1a. The MDR collected approximately 30-minute circular swaths of backscatter (reflectivity) with $7.5\text{ m} \times 7.5\text{ m}$ spatial resolution extending a radius of approximately 3 kilometers in each direction. Near surface currents were constructed following a procedure outlined in Lund et al. (2015) involving 3D Fast-Fourier transform of backscatter images and solving of the linear dispersion relationship over an inverted conical ‘shell’ mathematical space.

2.1.3 Laboratory experiments overview and objectives

Thirty-five independent but related experiments conducted in the SURge STructure Atmosphere INteraction (SUSTAIN) wind-wave tank at the University of Miami

Rosenstiel School of Marine and Atmospheric Sciences (RSMAS) provided the laboratory data for this dissertation. Experiments were conducted from July 10-14, 2018 in collaboration with chemists from Wellesley College. With observational gaps limiting progress in improved understanding of bubble dynamics and air-sea gas exchange in hurricane environments, these laboratory experiments were designed to examine the behavior of non-reactive gas invasion and the resulting bubble distributions (see also Stanley, et al., 2009). Furthermore, the joint research involved physically and optically observing the air-water interface and sub-surface water volume; this union of chemical and physical measurements was conducted in the hope of improving or conceiving of parameterizations for bubble behavior in the context of physical forces such as waves.

A specific water temperature, wind speed, and wave conditions were prescribed in each experiment. Wind speeds spanned the range $10.6 - 50 \text{ ms}^{-1}$; one of two wave types, monochromatic or JOint North Sea WAves Project (JONSWAP; Hasselmann et al., 1973) spectral waves, was chosen for each experiment. The duration of each experiment was governed by the noble gas mole ratios and saturation state of the gases, which were monitored throughout each experiment. A gas equilibration period with weak wind and gentle waves was necessary between each experiment. Water temperature set points for the experiments were 20, 26, and 32 degrees Celsius and were monitored at two depths across four locations total within the tank. Noble gases included neon (Ne), argon (Ar), krypton (Kr), and xenon (Xe). Oxygen gas (O_2) was also measured. A full summary of the experimental conditions, including gas saturation state, is provided in Table 2.2.

Exp #	T_w (°C)	U_{10}	Wave Type	f (Hz) or T_p (s)	a or H_{sig} (m)	Gas Saturation
1-8	26	20-50	M	1.00 Hz	0.15 m a	US

9-16	20	20-50	M	1.00 Hz	0.15 m <i>a</i>	US
17	26	35	M	1.00 Hz	0.15 m <i>a</i>	SS
18-24	32	20-50	M	1.00 Hz	0.15 m <i>a</i>	SS
25	26	35	S	0.65 s	0.5 m H_{sig}	US
26	26	40	S	1.00 s	0.5 m H_{sig}	US
27-34	26	10.6-50	S	1.00 s	0.15 m H_{sig}	US
35	32	20	M	1.00 Hz	0.15 m <i>a</i>	SS
EQ	-	10	S	0.65 s	0.15 m H_{sig}	-

Table 2.2 Summary of experimental conditions in SUSTAIN. Wave type is either “M” (monochromatic) or “S” (JONSWAP spectral). Gas saturation is reported as “US” (under-saturated) or “SS” (super-saturated). “EQ” refers to the gas equilibration period.

2.1.4 Laboratory wind-wave tank facility

SUSTAIN is 23-m long \times 6-m wide \times 2-m high with an 18-m test section composed of acrylic wall panels to facilitate optical measurements and flow visualization. The acrylic tank is mounted within a stainless steel frame and concrete, permitting rigid instrumentation installations within and through ceiling panels at specific fetches. Wind is driven by a 1460 horsepower fan and is forced through a flow collimator honeycomb array into the test section via a gently sloping adjustable flap, to avoid jump discontinuities as the wind meets the water surface.

Twelve independently operating HR Wallingford mechanical piston-action wave paddles are situated directly below the wind inlet and are controlled through computer software via Ethernet linkages and a user interface. When in use together, SUSTAIN is capable of producing 10-meter equivalent wind speeds in excess of 100 ms^{-1} (223.7 mph) and single-amplitude (monochromatic), spectral, and dispersive-focused waves with modified along-crest structure or spreading. Additionally, the SUSTAIN facility is equipped with a boiler-fed through-flow pump and heat exchanger that allows for specific set-point water temperatures to be achieved in the tank water volume; this capability was particularly crucial to the experimental design. A quasi-3D schematic of SUSTAIN

including the locations and types of instruments used in these experiments is shown in Figure 2.2.

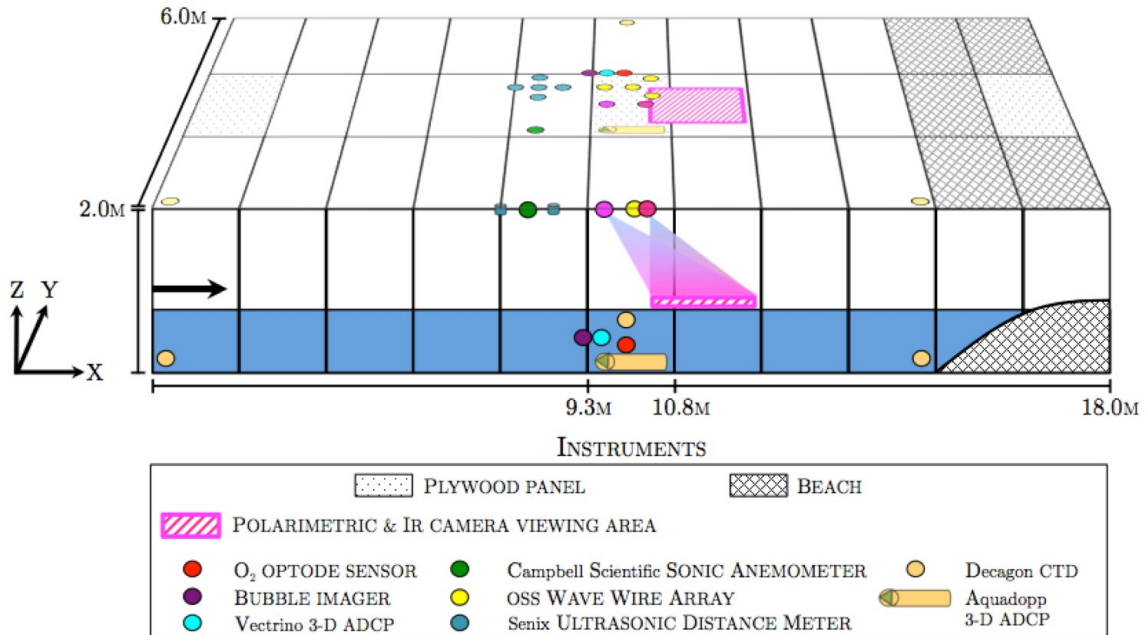


Figure 2.2 Schematic of the test section of the SURge STructure Atmosphere INteraction (SUSTAIN) facility wind-wave tank. The large black arrow on the left side of the schematic indicates the direction of air-flow. The instrument locations are indicated with symbols.

2.1.5 Laboratory data

2.1.5.1 Noble gas mass spectrometry and discrete sampling

Instruments were positioned near the middle of the SUSTAIN tank due to ease of access and to allow for wave development (see Figure 2.2). Noble gas measurements and discrete gas concentration samples were taken from the mid-tank region of the testing section ($\approx 9.10\text{--}10.6$ m fetch) using a gas equilibrator mass spectrometer (GEMS), equilibrator inlet mass spectrometer (EIMS), and an optode oxygen gas sensor. The GEMS and EIMS units were mounted on a crane-suspended platform above the SUSTAIN mid-tank panel to minimize momentum transfer and vibrations. GEMS and EIMS provided continuous noble gas mole ratios (e.g. Ne/Xe, Kr/Xe, etc.) and O₂ /Ar mole ratios, respectively; the two mass spectrometers were continuously routed sub-surface water from

SUSTAIN via a water pump relay system. Discrete noble gas samples for measuring actual concentrations were taken using copper tube sampling. The specific details of the noble gas measurement strategy and instrumentation are outside the scope of this dissertation, however we direct interested readers to Kinjo (2019).

2.1.5.2 Air-side instrumentation and measurements

Inlet-ward of the mid-tank panel, we placed a cross pattern array of 5 Senix ToughSonic ultrasonic distance meters (average fetch of 7.93 m) and at a roughly similar fetch (7.71 m), a Campbell Scientific IRGASON. The UDMs provided time-of-flight water surface elevation data at 10-20 Hz, and the IRGASON sonic anemometer component measured the 3D wind velocities at 20 Hz. The IRGASON was placed so as to not obstruct, or be obstructed in the flow. A series of three full-length (2 m) Ocean Sensor Systems (OSS) WS Type III wave wires were arranged in an equilateral triangular configuration with 0.283 m side lengths at an average fetch of 10.075 m. Each wire unit in the array recorded at 20 Hz sampling frequency and was externally hose-clamped and made taut based on visual necessity before experiments were underway. The triangular arrangement was chosen based on a similar configuration with UDMs aboard R/V *F.G. Walton Smith* during LASER (2016; see Chapter 2.1.2) for implementation of the wavelet directional method (WDM; Donelan et al., 1996) analysis using water surface elevation timeseries. This is discussed further in Chapter 2.2.7.

Above the mid-tank panel, two cameras were focused on a 1.20 m × 0.90 m rectangular region of the water surface, observed through protective thin plastic sheets. Nearer to the wind inlet, a FluxData FD-1665 polarimeter comprised of a beam-splitter and three Basler Scout charge-coupled device (CCD) cameras captured images at 50 frames

per second at 0° , 45° , and 90° linear polarization states for surface slope reconstruction. Details on this camera system, and its' use in the laboratory and the field are described in Laxague, et al. (2017). At the other end of the panel, a FLIR T540 series high-resolution forward-looking infrared camera was mounted to observe the surface skin temperature. The FLIR sampled nominally at about 30 Hz with 464×348 pixels square resolution; images were saved in sequence files using the FLIR Thermal Studio Pro software.

2.1.5.3 Sub-surface instrumentation and measurements

Water temperature was varied throughout the experiments, necessitating continuous measurements at multiple locations to ensure the water volume was homogenized. Four Decagon conductivity-temperature-depth (CTD) sensors were submerged and attached with suction cups in a downward facing orientation to give real-time information on the salinity, water temperature, heat exchanger performance for experiment timing, and depth for tank re-filling. Two CTDs were placed at the fetch extremes (0.05 m and 16.17 m) of SUSTAIN, near the inlet and start of the parabolic beach respectively; the other two were positioned at 9.86 m fetch in the mid-tank region but at heights of 0.125 m and 0.465m above the bottom of SUSTAIN. This arrangement allowed for the calculation of horizontal and vertical gradients.

Three different instruments were submerged and attached to the bottom of SUSTAIN in the mid-tank region using suction cups and lead weights: an oxygen optode sensor, two acoustic Doppler current profilers (ADCPs), and a bubble shadowgraph imager system. The oxygen optode sensor measured O₂ concentrations and was taking measurements at approximately 9.86 m fetch in-line with the vertically staggered CTDs. Both ADCPs were upward-sensing Nortek manufactured units; a four-beam fast-sampling

Vectrino Profiler and a three-beam 2 MHz Aquadopp HR high-resolution full-depth profiler. The Vectrino Profiler provided sub-surface velocity and turbulence data for this study, sampling at 100 Hz at 9.44 m fetch. Velocity and turbulence data were observed over a 0.03 m cylinder at 0.001 m vertical resolution; this field of view was 0.34 m down-fetch of the bubble imager system center.

Originally designed by Cedric Guigand (RSMAS) and used in the Ohmsett national oil spill response research and renewable energy test facility (Leonardo, NJ, USA) outdoor wave tank, the bubble shadowgraph imaging system (bubble imager) was comprised of an adjustable plastic and painted steel mount and two large cylinders encasing the camera and LED light source (see Figure 2.3). The bubble imager was positioned underwater at 9.10 m fetch and its data transmission and power cables were fed through the mid-tank plywood panel to a computer. Shadowgraph images were captured with a Basler avA2300-gm area-scan camera using a telecentric lens at 5 Hz imaging frequency. The telecentric lens removes parallax error that would distort object size in the images. Raw images were captured with 2328×1750 pixels square resolution.

Using a square calibration transparency with 0.001×0.001 meter grids, the raw field of view was translated into 0.0685×0.0515 meters in physical space. Multiplied by the 0.1-meter spacing between the two black cylindrical imager nodes, the bubble imager volume observed was $V_{\text{obs}} = 3.524 \times 10^{-4} \text{ m}^3$. The LED light source was a Luxeon Rebel royal blue (470 nm) emitter; light rays were directed through a collimator before entering the observed water volume.

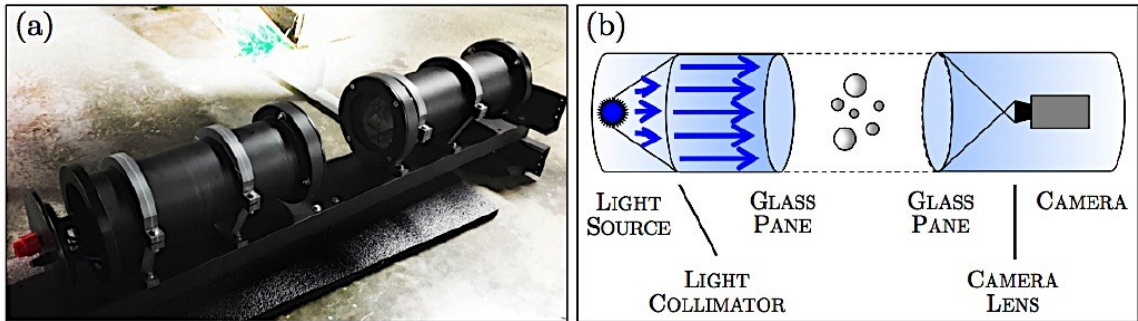


Figure 2.3. The bubble shadowgraph imager unit (a) photograph and (b) schematic diagram of components and operation concept. The blue arrows show the path of light from the LED. The shadowed objects in the center between the nodes are bubbles. Schematic not to scale.

2.2 Analysis methodology

2.2.1 Motion correction for ship data

Although multi-instrument platforms can provide diverse, virtually spatiotemporally synchronous data in otherwise challenging environments, non-stationary platforms introduce spurious energy via accelerations that must be removed. To eliminate platform motion from measurements and their subsequent derived quantities, motion correction pre-processing was performed on the data collected aboard R/V *F.G. Walton Smith*. Motion correction is common practice in the literature, and has been performed on data from aircraft (e.g. Miyake, et al. 1970), ships (Fujitani, 1985), and buoys (Dugan, et al. 1991) using knowledge of the axial and angular motion of the platform or instrument.

Six degrees of acceleration of FGWS (i.e., roll, pitch, yaw, surge, sway, and heave) were measured using the motion measurement package described in Chapter 2.1.2. Fixed-mount instrument data was motion-corrected independent of quality control unique to individual sensors by implementing the oft-cited motion-correction algorithm outlined in Anctil et al. (1994). The relative-to-absolute motion transformation matrix T_{BE} is

$$\mathbf{T}_{BE} = \begin{pmatrix} \cos \theta \cos \psi & \sin \phi \sin \theta \cos \psi - \cos \phi \sin \psi & \cos \phi \sin \theta \cos \psi + \sin \phi \sin \psi \\ \cos \theta \sin \psi & \sin \phi \sin \theta \sin \psi + \cos \phi \cos \psi & \cos \phi \sin \theta \sin \psi - \sin \phi \cos \psi \\ -\sin \theta & \sin \phi \cos \theta & \cos \phi \cos \theta \end{pmatrix} \quad (2.1)$$

where roll ϕ , pitch θ , and yaw ψ are the fundamental accelerations in (2.1) and subscript BE refers to the transformation between the platform B velocities \mathbf{u}_B and Earth reference-frame velocities \mathbf{u}_E . Gravitational acceleration of the platform is included in vector form as

$$\mathbf{g}_B = (0 \ 0 \ -g)^T \quad (2.2)$$

with $g = 9.81 \text{ ms}^{-2}$ and the superscript T denoting the matrix transpose. Using (2.1) and (2.2), the Earth reference-frame corrected velocity \mathbf{u}_E is

$$\mathbf{u}_E = \mathbf{T}_{BE} \mathbf{u}_B + \mathbf{T}_{BE} \int (\mathbf{a}_B + \mathbf{g}_B) dt + \boldsymbol{\Omega} \times \mathbf{T}_{BE} \mathbf{L}_B \quad (2.3)$$

where the angular rotation vector $\boldsymbol{\Omega}$ is

$$\boldsymbol{\Omega} = \begin{pmatrix} -\dot{\psi} & \cdot & \cdot \\ \dot{\theta} & \cdot & \cdot \\ \cdot & \dot{\phi} & \cdot \end{pmatrix} \quad (2.4)$$

with dots indicating the time derivative of the dotted quantity. The cross product $\boldsymbol{\Omega} \times \mathbf{T}_{BE} \mathbf{L}_B$ is the angular acceleration given the physical distance between the motion package and the instrument at the position described by the vector \mathbf{L}_B .

2.2.2 Eddy covariance fluxes and signal decompositions

Having sampled at high-frequency most of the physical state variables (e.g. velocity, temperature, etc.), we were able to capture turbulent motions and compute sensible heat, latent heat, momentum, and energy fluxes using the eddy-covariance method

(Burba and Anderson, 2007). The eddy-covariance method involves a Reynolds decomposition of vertical velocity and the scalar quantity of interest (e.g. temperature), which are de-trended. Reynolds decomposition separates the mean and time-varying perturbation or anomaly fields such that, for example, vertical velocity would be expressed as

$$w(t) = \bar{w} + w'(t) \quad (2.5)$$

where \bar{w} is the time-independent mean and $w'(t)$ are perturbations that vary with time. The covariance is represented by the product of perturbations of the two quantities, which is averaged over a suitable time window. Averages of 10, 15, 30, and 60 minutes are commonly used, however the choice depends on the data and environment so that the claim of stationarity is acceptable (Large and Pond, 1981). Stationarity is a simplifying assumption that the unconditional probability distribution of a stochastic quantity is time-independent. Consequently, the mean and variance are also theoretically constant. A 10-minute averaging window was used when computing fluxes from data collected aboard *FGWS*. Sensible and latent heat fluxes hence are defined as

$$H_S = \rho_a c_{pd} \overline{w' T'} \quad (2.6)$$

$$H_L = \rho_a L_v \overline{w' q'} \quad (2.7)$$

where $c_{pd} = 1004.67 \text{ J kg}^{-1} \text{ K}^{-1}$ is the specific heat capacity of dry air at constant pressure, q is the specific humidity at saturation, T is the air temperature, and $L_v = 2.5 \times 10^6 \text{ J K}^{-1}$ is the latent heat of vaporization. Momentum flux, or Reynolds stress, after Zhang et al. (2011) is

$$\tau = \rho_a (-\overline{w' u'} \mathbf{i} - \overline{w' v'} \mathbf{j}) \quad (2.8)$$

where the units of (2.6), (2.7), and (2.8) are Wm^{-2} , Wm^{-2} , and Nm^{-1} , respectively. Water-side Reynolds stress was calculated by substituting water density ρ_w and the water-side velocities in (2.8). The sign or direction (air-sea or sea-air) of fluxes was determined by the sign of the covariance terms, which for example can yield positive or upward momentum fluxes in swell wave conditions. In strongly wave-forced fluid boundary layers such as the WBL or ocean surface layer (OSL), a wave-coherent component constrained by distance from the air-sea interface should be included in the signal. This ‘triple’ decomposition, using the example of vertical velocity as in (2.5) is,

$$w(t, z, \phi) = \bar{w}(z) + w'(t, z) + \tilde{w} \quad (2.9)$$

adapted from Hara and Sullivan (2015). The wave-coherent component \tilde{w} is extracted through correlation of velocity and water surface displacement $\eta(t)$ spectra and subsequent execution of band-pass filtering over a wave band identified from these spectra following Benilov and Filyushkin (1970). The wave-coherent component includes vertical distance from or depth beneath the air-sea interface z and dependence on wave phase ϕ , while all other terms are the same as in (2.5) except the addition of z . Triple composition is necessary to compute the turbulent kinetic energy (TKE) budget in the WBL, and is important for including physics such as form drag, skin drag, and wave-induced fluxes. Such decomposition has been performed in recent laboratory and numerical modeling studies (Hara and Sullivan, 2015; Buckley and Veron, 2017) to improve turbulence closure and understanding of multi-scale wave-driven physics very near the interface. To highlight the differences between the field and laboratory data, a comparison of velocity signals measured aboard R/V *F.G. Walton Smith* (ASL, 5.90 meters above air-sea interface) and

in the SUSTAIN wind-wave laboratory tank (OSL, 0.30 meters beneath air-sea interface) are shown in Figure 2.4.

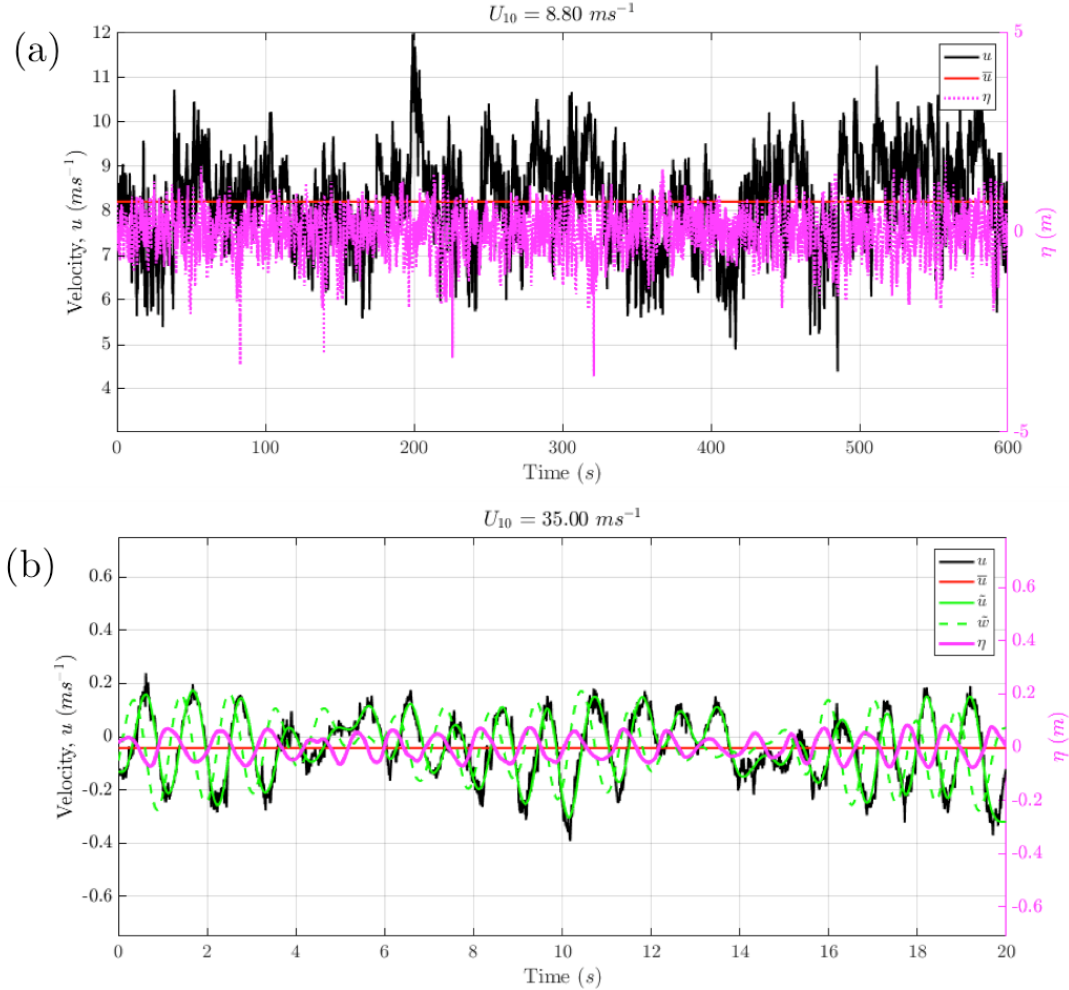


Figure 2.4 (a) Sonic anemometer zonal velocity (starboard tower) and water surface elevation from R/V *F.G. Walton Smith* where $U_{10} = 8.80 m s^{-1}$. Total and mean velocities are in black and red, respectively. Ultrasonic distance meter (UDM) derived water surface elevation, η , is plotted in magenta. (b) Sub-surface zonal and vertical velocity components, and water surface elevations from the SUSTAIN wind-wave tank laboratory. Total and mean velocities are in black and red, respectively. Wave-coherent zonal and vertical velocities are in lime green. Water surface elevation is in magenta. The horizontal axis in each figure is the time in seconds relative to the start of the record.

2.2.3 Turbulence spectra and dissipation rate

2.2.3.1 Atmospheric surface layer

Velocity spectra were constructed from IRGASON and RMY 3D velocity timeseries from the *FGWS* flux towers using the Fast-Fourier transform (FFT); each anemometer had a sampling rate of 16 Hz. FFT transforms the velocity measured in time into frequency space by characterizing the data as a summation of sines and cosines via

$$X_k = \sum_{n=0}^{N-1} x_n \cdot e^{-\frac{i2\pi}{N} kn} = \sum_{n=0}^{N-1} x_n \cdot \left[\cos\left(\frac{2\pi}{N} kn\right) - i \cdot \sin\left(\frac{2\pi}{N} kn\right) \right] \quad (2.10)$$

where x_n is the original data (timeseries), and X_k is the resulting spectral transformation.

Velocity data was de-trended and a Blackman-Harris windowing function $w_{BH}(n)$ was used to minimize side-lobe leakage prior to executing the FFT (2.1),

$$w_{BH}(n) = 0.359 - 0.488 \cos\left(\frac{2\pi n}{N}\right) + 0.1413 \cos\left(\frac{4\pi n}{N}\right) - 0.0117 \cos\left(\frac{6\pi n}{N}\right) \quad (2.11)$$

where N is the total length of the velocity timeseries. The number of elementary frequencies averaged in the construction of the scaling coefficient for the FFT, $N_{FA} = 16$ was chosen based on the sampling frequency of the sonic anemometers to ensure the spectra are sufficiently represented at higher frequencies and to limit noise.

Dissipation rate of TKE is calculated using the inertial dissipation method and application of Taylor's frozen turbulence hypothesis via (1.8) from Chapter 1.1.2. Advection velocity

$U_a = \sqrt{u_a^2 + v_a^2 + w_a^2}$ was calculated from the motion-corrected 3D sonic anemometer velocities and ship velocity measured aboard *FGWS*. Mean horizontal flow velocities u_a and v_a are the mean flow velocities with vessel translation accounted for using GPS-derived ship vessel speed data. The inertial sub-range $\Delta f = 2 - 4$ Hz was prescribed following Zhang (2010). Velocity data were rejected if the mean ship heading minus wind direction (HMWD) exceeded $\pm 70^\circ$ to avoid including

‘shadow zone’ flow distortion induced wakes caused by the instrument (Kaimal 1979; Weiser et al. 2001; Wyngaard 1981; Wyngaard and Zhang, 1985).

Additionally, velocity spectra were quality controlled for universality as compared with the theoretical $f^{-5/3}$ slope (Kolmogorov, 1941), isotropy in the inertial sub-range using the ratio of zonal and vertical velocity spectral density (Ortiz-Suslow et al. 2019), and conformance with Taylor’s frozen turbulence hypothesis (Taylor, 1938, Eq. 7). Spectra with percent errors of less than 25 percent and turbulent intensity to advection velocity ratios of less than 0.2 were retained.

2.2.3.2. Sub-surface laboratory

Sub-surface turbulence and dissipation was measured using the Nortek Vectrino Profiler pulse-coherent acoustic Doppler current profiler (ADCP) over the finite depth cylinder of 0.03 meters at 0.001 meters vertical resolution. The Vectrino ADCP sampled at 100 Hz, sufficient to resolve turbulence. Individual data sequences were merged for each experiment and post-processed to extract the 3D velocity components and signal to noise ratio (SNR). From the velocities, we derived the kinetic energy E_k , TKE, the friction velocity u_{*w} , Reynolds stress τ_w , and shear. SNR is recorded in real-time for each beam (4 total), giving data quality information for u, v, w_1 , and w_2 velocities separately in decibels (dB) as

$$SNR(a) = 20 \log_{10} \left(\frac{\|a\|}{\|a_\epsilon\|} \right) \quad (2.12)$$

for velocity component a with signal amplitude $\|a\|$ and noise amplitude $\|a_\epsilon\|$.

According to the Nortek comprehensive technical manual, SNR values for our Vectrino model take a parabolic shape over the cylindrical volume. At the upper and lower extremes, $SNR \geq 20$ are of good quality, while in the center region of the volume, data with $SNR \geq 30$ are

necessary to pass quality control. Similar to conventional Doppler radar used in weather monitoring, the Vectrino ADCP determines velocities by comparing the constant frequency of sound pulses sent out with the returned apparent frequency due to Doppler effect backscattered by particles or scatterers in the flow (e.g. bubbles). As a result, spikes in velocity data can result from, for example, sound pulses pinging off of large or dense scatterers.

Therefore, a two-step process of quality control was implemented on raw velocity data: (a) removal of low *SNR* values according to a threshold based on distance from the sensor head in the volume, and (b) de-spiking of the remaining velocity data. A 3D phase-space de-spiking algorithm developed by Goring and Nikora (2002) was used for (b). The algorithm enclosed data with a Poincare ellipse constructed from the derivative and Laplacian of the data, and eliminated extremes outside that ellipse. Rapidly changing data, or data with large variance or spread fell outside the ellipse and was flagged as outliers or spikes. Data within the Poincare ellipse was retained, while bad data was eliminated and replaced with a linear interpolation (W.M. Drennan, 2020; personal communication). An example of the effects of this de-spiking procedure is shown in Figure 2.5.

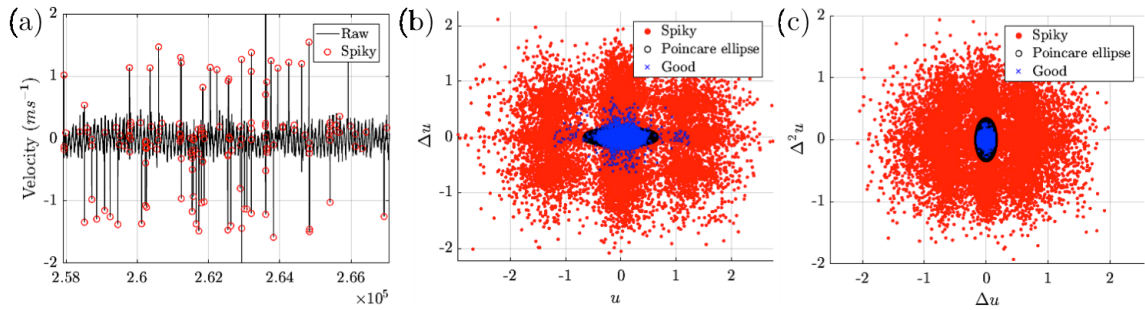


Figure 2.5. Vectrino ADCP de-spiking example using Goring and Nikora (2002) 3D phase-space algorithm. (a) Raw timeseries and spikes identified (b) Velocity versus derivative within the 3D phase space (c) Derivative versus Laplacian of velocity within the 3D phase space. Red values are spiky, blue values are good, and the black circle indicates the Poincare ellipse. Aspect ratio of the figures not to scale.

Turbulence spectra were constructed in the same manner as for the field data from FGWS via implementation of the FFT, taking velocity data within 20 s of the timestamp of observed sub-surface shadowgraph bubble images. Given the sampling rate of the Vectrino ADCP, this yields

2000 values and we use $N_{\text{FA}} = 10$ for this sub-surface velocity data. TKE dissipation rate was calculated in the same manner as was done with field data from *FGWS* via inertial dissipation method, however, a recently developed robust algorithm for determining the inertial sub-range (ARIIS; Ortiz-Suslow, et al. 2019) was used in place of an arbitrarily prescribed Δf . Historically this inertial sub-range Δf has been identified using arbitrary bandwidths or subjective visual inspection of velocity spectra (e.g. Large and Pond, 1981; Fairall and Larsen, 1986; Yelland and Taylor, 1996; Sjöblom and Smedman, 2002). ARIIS alleviates conventional assumptions and ambiguity by identifying the most probable inertial sub-range and its' slope. ARIIS was platform-tested using towered 3D ultrasonic anemometers on R/P *FLIP* during the Coupled Air-Sea Processes and Electromagnetic Ducting Research (CASPER) field campaign. The algorithm has two components: (a) checking for isotropic convergence, and (b) a robust slope fitting of the identified sub-range to $f^{-5/3}$. Isotropic convergence was determined by calculating an isotropy coefficient for each direction of velocity data (Jimenez et al., 1992; Ortiz-Suslow, et al. 2019),

$$I_{ij}(k) = \frac{E_{ii}(k) + k(\partial E_{ii}/\partial k)}{2E_{jj}} \quad (2.13)$$

and the ratio of orthogonal velocity spectra $R_{uw} = S_{uu}/S_{ww}$ as described in Chapter 1.1.2 to satisfy conditions put forth by Kolmogorov (1941). In applying Taylor's frozen turbulence hypothesis $k = 2\pi f U_a^{-1}$, the advection velocity U_a for the sub-surface water velocity field was taken to be $U_{a,L} = \sqrt{\frac{1}{N} \sum_{i=1}^N w_i^2} \cdot \sqrt{2}$ to avoid wave-induced orbital velocity zero net displacement following Terray et al. (1996).

2.2.4 TKE budget in the atmospheric surface layer

Velocity, temperature, humidity, and air pressure data from flux towers aboard *FGWS* were used to construct the TKE budget in the ASL using (1.2). Perturbation and mean potential temperature were calculated using the familiar expression,

$$\theta = T \left(\frac{p_0}{p} \right)^{R_d c_p^{-1}} \quad (2.14)$$

where $p_0 = 1000$ hPa is the reference pressure, $R_d = 287 \text{ J kg}^{-1} \text{ K}^{-1}$ is the dry air gas constant, and $c_p = c_{pd}(1 + 0.84r_v)$ is the specific heat capacity at constant pressure. The water vapor mixing ratio $r_v = 0.622e_v/(p - e_v)$ is a function of total pressure and vapor pressure, e_v . Absolute air pressure was measured by IRGASON pressure cell on each flux tower however, since these measurements were made at only one height on each tower a vertical derivative of turbulent pressure fluctuations could not be calculated and the pressure work term (5) of the TKE budget (1.2) was calculated as the residual

$$P = S - B - T - \varepsilon \quad (2.15)$$

where P is the pressure work (or pressure transport), S is the shear production of TKE, B is the buoyant production of TKE, ε is the dissipation rate of TKE, and T is the TKE transport term,

$$T = - \frac{\partial \overline{w'e}}{\partial z} \quad (2.16)$$

as defined in (1.2), for which the vertical derivative of TKE and vertical velocity were computed using the two upper-most sonic anemometers on the starboard bow flux tower. Monin-Obukhov stability ζ was computed using shear and buoyancy production terms from the TKE budget, as has been common practice in the literature (e.g. Wyngaard and

Cote, 1971; Fairall and Larson, 1986; Edson and Fairall, 1998; Sjöblom and Smedman, 2002) to evaluate the behavior of the individual budget terms in terms of atmospheric stability. In context then,

$$\zeta = z L_\zeta^{-1} = z \left(-\frac{S}{B} \right)^{-1} \quad (2.17)$$

takes the same form as given in Chapter 1.1.1.

2.2.5 Open ocean sea state determination

Subjection of the sea surface to physical forcing by the wind, particularly in the open ocean where fetch may be large and uninterrupted, allows for potentially large energy transfer between the atmosphere and ocean. Roughening of local windsea, the presence of swell, or a mixed sea influences turbulence and TKE dissipation in the ASL. Furthermore, since previous studies have shown TKE budget terms balance and contribute to the budget differently for windsea and swell (e.g. Sjöblom and Smedman 2002; Hogstrom et al. 2009), the sea states are explicitly determined for open ocean field data using water surface elevation spectra from the *FGWS* bow ultrasonic distance meter (UDM) array (see Chapter 2.1.2.2) using a three-step process.

Water surface elevation spectra composed of 10-minute segments of data were quality controlled, then the wavelet directional method (WDM; Donelan, et al. 1996) was implemented, and finally the Pierson and Moskowitz (1964) criterion, $c_p U_{10N}^{-1} > 1.2$ expected for swell, was applied. Discrimination of sea states using wind speed and the Pierson and Moskowitz (1964) criterion is demonstrated in Potter (2015, see their Figure 1). Quality control of the five-UDM array first eliminated data at frequencies less than or equal to 0.0667 Hz, equivalent to wave periods of 15 seconds. Waves of this period were

considered unlikely given the fetch of the Gulf of Mexico where field data was collected (W.M. Drennan, 2017; personal communication).

Given their large separation distance (10.22 meters), a median of port and starboard prow UDM η spectra was used as a truth measurement of wave data not contaminated by signal cross-talk; this cross-talk would corrupt data from UDMs spaced too closely together. A quality control flag was thus used to exclude center truss triplet UDM data with ‘runaway error’ associated with cross-talk before these were fed to the WDM codes. The complete details of WDM are described in Donelan et al. (1996), however, we present the basic steps here. We first de-spiked the three quality-controlled UDM η timeseries, and defined the positions and UDM array geometry.

Spectra constructed from the timeseries were used to create a wave energy amplitude matrix based on the Morlet wavelet. Given a directional resolution of 5° and wavenumber resolution of $0.1 \text{ rad } m^{-1}$, the directional wavenumber-frequency spectrum was constructed based on wave energy and array geometry in the triangular UDM array. The location of the maximum spectral density in the omnidirectional directional (frequency) spectrum provided the dominant wave direction (frequency). Hence, the phase speed of the dominant wave was computed via

$$c_p = gT_p/2\pi \quad (2.18)$$

such that the wave age $\beta_\eta = c_p U_{10N}^{-1}$ could be determined and classified as wind-sea or swell according to

$$\beta_\eta \begin{cases} < 1.2 & \text{Windsea} \\ \geq 1.2 & \text{Swell} \end{cases} \quad (2.19)$$

2.2.6 Laboratory wave crest analysis

Changes in water surface elevation and depth recorded by a triplet array of conductivity-sensitive wave wires produced timeseries of the local sea surface structure. Quality control of the raw wave wire timeseries was executed to remove periodic spurious zero value spikes associated with the data logging system the array was wired into. Subsequently, the signals were de-trended and a moving average was removed to yield the water surface elevation, η . Individual wave crests and troughs were identified in $\eta(t)$ through a combination of searching for positive and negative peaks and finding zero-crossing locations. Careful interpretation of zero-crossing locations relative to peaks and troughs was systematically used to determine whether zero-crossings were ahead of the forward or rear part of a wave in the timeseries. The crests and troughs were paired so that each identified individual wave crest had a single crest, trough, forward edge, and rear edge.

To quantify statistics of the individual waves, we adapted an analysis technique used on wave staff data from the SUSTAIN wind-wave tank predecessor Air-Sea Interaction Saltwater Tank (ASIST) in an earlier laboratory experiment (Babanin, et al. 2007). Each wave was subdivided into four quadrants symbolized by a_1 , a_2 , b_1 and b_2 . Figure 2.6 compares the concept implemented by Babanin, et al. (2007) with an example of the method implementation with SUSTAIN wave-wire array data.

It should be noted that Figure 2.6(a) is adapted from Babanin et al. (2007) Figure 1, and depicts three waves of varying linearity relative to horizontal distance x using the two-dimensional Chalikov-Sheinin model (CSM; Chalikov and Sheinin, 2005) solution to the Euler equation. Conversely, laboratory data shown in Figure 2.6(b) depicts the water

surface elevation timeseries relative to record number, with time proceeding from left to right. The height H , asymmetry A_s , and skewedness S_k of each individual wave was determined by mathematical relationships between the wave crest quadrants, that is,

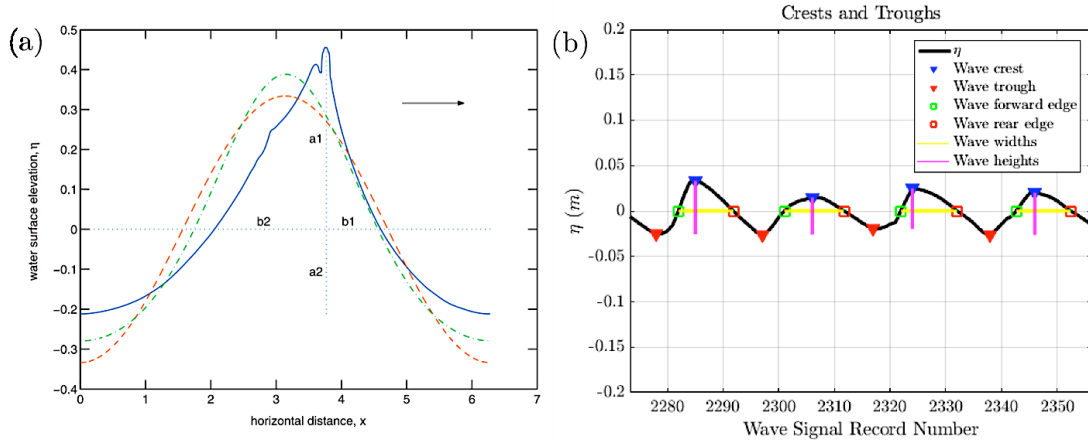


Figure 2.6 (a) Three waves of different non-linearity, where the blue solid line is an incipient breaking wave with asymmetry, skewedness and steepness, c.f. Babanin et al. (2007). (b) Example wave crest analysis from a monochromatic wave case in the SUSTAIN wind-wave tank. Water surface displacement η is in black solid, wave crests and troughs are indicated by blue and red triangles, respectively. Magenta and yellow lines identify the height and width of wave features. Green and red squares are situated at zero crossings in η to denote forward and rear edges of the waves.

$$H = a_1 + a_2 \quad (2.20)$$

$$A_s = (b_1/b_2) - 1 \quad (2.21)$$

$$S_k = (a_1/a_2) - 1 \quad (2.22)$$

where a_1 is the wave positive prominence from zero to most positive η , a_2 is the negative prominence from zero to most negative η , b_1 is the forward part of the wave from crest location to zero crossing, and b_2 is the rear part of the wave from crest location to zero crossing. The dimensionless steepness of each wave is

$$\delta = ak = (H/2)k \quad (2.23)$$

equal to the ratio of wave amplitude or half-height $H/2$ and wavenumber k . The wavenumber was determined iteratively by solving the full gravity-capillary linear dispersion relationship given by (1.9). Surface tension σ was approximated using a quadratic polynomial fit $\sigma(T) \approx -2.91 \times 10^{-4}T - 0.14T + 75.65$ ($R^2 = 0.99$) of data from the International Tables of the Surface Tension of Water (Vargaftik, et al. 1983). By using this individual wave feature analysis across all wind and wave conditions from laboratory experiments, the surface wave characteristics (e.g. $H, k, T, \omega, \delta, L, c$) statistics (e.g. significant wave height H_{sig}) were able to be determined in a robust manner.

2.2.7 Wave growth and directional wave spectra

We acknowledge that the individual wave statistics excluded features that did not cross zero (i.e. the displacement signal did not cross zero up for the crest and down again for the trough) and that quantifying or classifying wave breaking using a local steepness criterion alone would be an arbitrary choice and insufficient given that the theoretical Stokes' limiting steepness $ak = \pi/7 = 0.449$ (i.e. $HL^{-1} = 1/7 \approx 0.143$) is rarely observed in the field (Holthuijsen and Herbers, 1986; Gemmrich, 2010). Therefore, by taking advantage of the fast sampling rate and compact equilateral triangular geometry of the wave wire array, we also computed the two-dimensional directional wave spectra $S_n(\omega, \theta)$ using WDM (Donelan, et al. 1996) described in Section 2.2.5.

Given that wave breaking again may occur across a spectrum of scales (Gemmrich, 2010) and not be accompanied by visual air entrainment or whitecaps (Melville, et al. 2002), the spectrum allowed us to fully characterize the laboratory wave field and its' growth in time (i.e. $\partial S_n / \partial t$ at fetch x). Directional wave spectra were also used to apply

the wave-dependent scaling $\varepsilon H_s/F$ (Drennan, et al. 1996; Terray et al. 1996) to sub-surface TKE dissipation rates ε by calculating the wind input to wave growth F , given by (1.12) as a function of wave growth rate $\beta(\omega, \theta)$ defined in (1.13). The wind speed at half the wave height $U_{L/2}$ is a reference wind speed that was determined using $U(z)$ at the height of the laboratory sonic anemometer, and derived friction velocity u_* via

$$U_{L/2} = U(z) + \left(\frac{u_*}{\kappa} \right) \ln \left(\frac{L}{2z} \right) \quad (2.24)$$

where the von Karman constant $\kappa = 0.4$ and L is the wavelength.

2.2.8 Bubble imaging and feature determination

Sub-surface bubbles were observed using shadowgraphy, wherein the imager system camera captured the visible pattern of illumination variations caused by the obstruction, refraction, and attenuation of light rays caused by these bubbles. The degree of angular deflection of light by a bubble is directly related to its size and composition (i.e. void fraction) via Snell's law of refraction, and resulted in differing presentation of objects on the images; an example of an observed bubble in this context is shown in Figure 2.7.

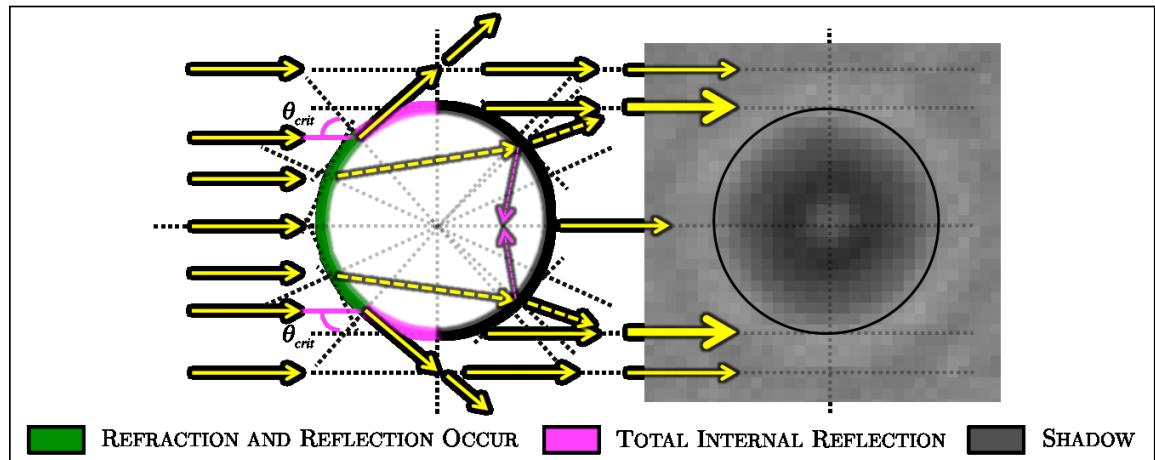


Figure 2.7 Optical physics of light and scattering through spherical bubbles per Snell's Law. A schematic is shown on the left, with a bubble identified from shadowgraph images to scale on the right. Yellow arrows indicate the path of light, with dashed lines indicating

light passing through the bubble. The thickness of yellow arrows indicates the amount of light reaching the location. The angle θ_{crit} is the angle beyond which there is total internal reflection and hence, no refraction or bending of the light.

Illumination (or contrast) gradients in the images (or shadowgrams) were analyzed to identify the boundaries of the bubbles via a circular Hough transform (CHT; Atherton and Kerbyson, 1999), which has been used in previous studies where bubble distribution was optically quantified (e.g. Deane and Stokes, 1999). For each image, the CHT uses a complex (i.e., real and imaginary) 3D accumulator array that gathers votes cast by foreground pixels of sufficient illumination gradient magnitude. A user-defined sensitivity threshold defines whether pixels possess sufficient gradient magnitude to cast votes. Votes are cast in a circle of fixed radius r for and at the location of all eligible pixel pairs (x, y) in the image to determine the circle center (a_x, a_y) . Intuitively, overlap of votes defines the circle center and is the namesake accumulation.

In a second step, the precise radius r is determined using a ‘phase-coding’ technique; briefly, the method involves accumulating in-phase pixels along radial ‘spoke’ lines of varying phase ($0 - 2\pi$) between edge pixels and circle centers. For additional details readers are directed to Atherton and Kerbyson (1993), however for our purposes the CHT provides coordinates of the center of bubble objects and their radii over a span of radius values. Once identified, the volume and surface area were calculated for each bubble using the radius r and spherical formulas,

$$V_b = (4/3)\pi r^3 \quad (2.25)$$

$$A_b = 4\pi r^2 \quad (2.26)$$

Bubble spectra were determined as in previous literature (Thorpe (1982); Deane and Stokes (2002)) by constructing a histogram of bubble statistics across the span of searched radii.

The number of bubbles was normalized by the observed volume $V_{obs} = 3.524 \times 10^{-4} \text{ m}^3$.

Scott's rule was used to determine the bin width dr ,

$$dr = 3.49\sigma / \sqrt[3]{n} \quad (2.27)$$

where σ is the standard deviation of the bubble radii and n is the total number of bubbles observed. Additionally, we constrained the dr to take values no less than the $30.25 \mu\text{m}$ pixel resolution of the imager camera as was done in Deane and Stokes (1999) to avoid improper binning of sub-pixel bubble objects. Using this, we constructed bubble size spectra $N_b(r)$ and bubble volume spectra $V_b(r)$ normalized by bin width with units number (or volume) of bubbles per meters cubed per micrometer radius increment dr .

Probability and cumulative density functions were constructed in a similar manner. CHT algorithm error could be quantified for any bubble image using region property (RP) analysis of individual bubbles to determine bubble centroid, boundary circularity, and equivalent radius. Three types of error existed for this comparison: position error, radius error, and circularity error. These are based on the fact that CHT assumes objects it detects are circular, and that the position and radius are robustly determined. Region property analysis used the CHT-derived center and radius as null hypotheses and used a 0.96 binarization threshold (0 black, 1 white) to isolate and determine the statistics for each bubble in an image space isolated from other bubbles. The position, radius, and circularity errors are expressed as percent errors based on CHT-derived values; that is,

$$\epsilon \quad < 100 \quad (2.28)$$

$$\epsilon \quad \left| \frac{-r_{RP}}{r_{CHT}} \right| \times 100 \quad (2.29)$$

$$\epsilon \quad \left| \frac{\Gamma_{HT} - \Gamma_{RP}}{\Gamma_{CHT}} \right| \times 100 \quad (2.30)$$

where D is the distance between the region property analysis center and the theoretical CHT-derived center, and Γ is the circularity (where 0 a straight line, 1 a perfect circle). Each error metric was fit to measurements of the absolute bubble object gradient $\|\Delta\|$ for a series of 70 images taken beneath an open ocean wave spectrum in the SUSTAIN laboratory wind-wave tank. Position and radius errors were found to decrease with $\|\Delta\|$, that is, errors were reduced for bubbles with greater refraction and therefore more obvious optical differences between the inside and outside of the bubble. Circularity errors were least affected by $\|\Delta\|$, intuitively because bubbles could be non-circular, deform, or interact with other bubbles regardless of the void fraction. After visual inspection of these bubble images, bubbles with $\|\Delta\| < 0.02$ were discarded. Linear fits to the error statistics as mentioned are shown along with R^2 and root-mean-square error (RMSE) values in Figure 2.8.

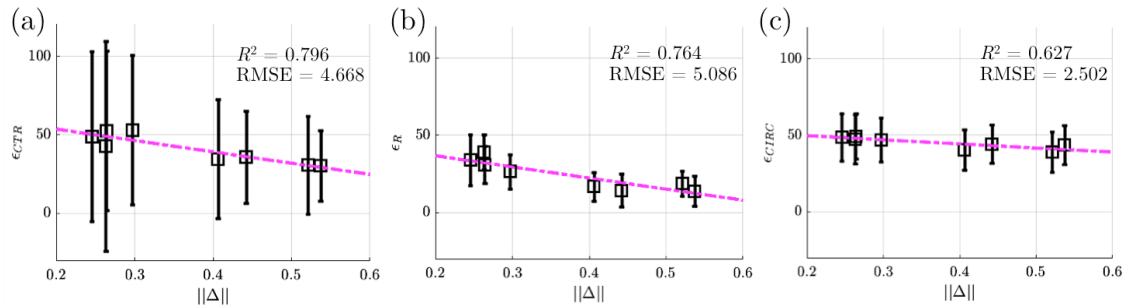


Figure 2.8 Percent error in (a) center position (b) radius, and (c) circularity comparing CHT and RP analysis methods as a function of absolute bubble gradient (interior versus exterior illumination of bubble) from open ocean wave spectrum conditions in SUSTAIN. All errors are percent errors. The magenta line is a linear fit or trend line. The black boxes and error bars indicate the median and standard deviation, respectively.

Ultimately, the default sensitivity threshold of 0.85 was used for CHT bubble identification. A comparison of CHT and region property (RP) analysis is shown with a cluster of bubbles from an example laboratory shadowgraph image in Figure 2.9. A

reference image taken in quiescent conditions was originally used as a background filter, but discarded based on sub-surface observations in high wind conditions that resulted in too much optical disruption of the field of view relative to the reference image.

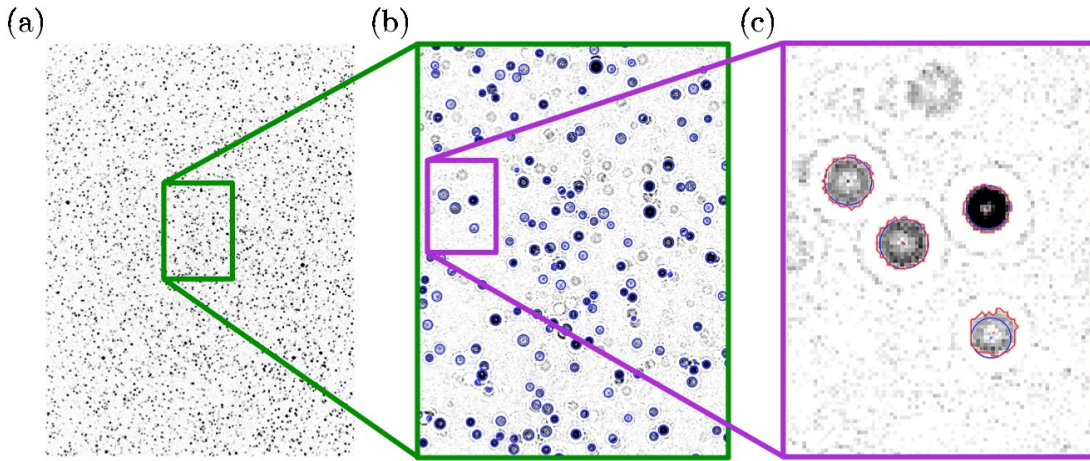


Figure 2.9 Comparison of Circular Hough Transform (CHT) and region properties (RP) analysis, where identified bubble boundaries are given in blue and red for the two methods, respectively. (a) Entire raw image with background filtered using a reference image (b) Zoomed in on a cluster of bubbles identified with CHT (c) Zoomed in further to show a comparison of object boundaries, center positions, and size using CHT and RP analysis.

2.3 Summary

We have used a combination of open-ocean field and laboratory wind-wave tank data to investigate and compare how sea surface structure drives turbulent kinetic energy and its' dissipation in the atmosphere and below the air-water interface. Field data was collected as part of the LASER (2016) field campaign to investigate ocean surface transport, dispersion and the fate of crude oil, and included flux tower wind, relative humidity, temperature, and water surface elevation data. Sea surface temperature, salinity, pressure and Marine Doppler radar data were also used to investigate turbulence and dissipation adjacent to observed submesoscale ocean fronts. Sea surface structure was determined using spectral analysis to construct directional wave-frequency spectra,

identifying peak wave characteristics and surface roughness, and classifying the sea state as windsea or swell using conventions from the literature. The low wind environment and length of the LASER campaign provided an extensive dataset that did not require navigating around instrument error or data quality concerns found in hurricane environments. Laboratory experiments act as a companion to the field data, while also yielding data from hurricane wind-wave conditions in a controlled setting. Mechanically generated wave paddles produced both idealized monochromatic and more realistic JONSWAP spectrum wave fields in addition to equivalent 10-meter hurricane force winds up to 50 ms^{-1} . Field techniques to characterize the two-dimensional wave spectrum, compute TKE, and dissipation rate were implemented in the laboratory using wave wires and sub-surface ADCP. Simultaneous shadowgraph imaging of bubbles was directly linked with water temperature, wave breaking intensity, and surface roughness observed via individual wave crest analysis techniques. Bubble size distributions were constructed using a robust bubble detection algorithm and histogram binning method used in previous studies. In conclusion, this dissertation uses diverse datasets with benefits and drawbacks to address the motivating research questions surrounding sea surface structure and turbulence in surface layers adjacent to the air-sea interface. In particular, the differences in the datasets allow for comparisons to be made concerning the influence of waves in the two environments and to contribute unprecedented data from hurricane conditions in part using a wave field modeled after field open ocean conditions (i.e. JONSWAP wave spectrum).

Chapter 3: Turbulence, Fluxes, and Dissipation in the Atmospheric Surface Layer

3.1 Turbulent kinetic energy observations and ambient conditions

During the LASER (2016) field campaign, R/V *F.G. Walton Smith* traversed segments of the Gulf of Mexico near the *Deepwater Horizon* drilling platform, offshore of southeastern Louisiana, Mississippi, and Alabama (see Figure 2.1). FGWS bow flux towers provided the high-frequency 3D air velocity measurements necessary to calculate the turbulent kinetic energy $e = (\overline{u'^2} + \overline{v'^2} + \overline{w'^2}) / 2$ and its average dissipation rate $\bar{\epsilon}$ for each 10 minute segment as the ship traveled. Figure 3.1 shows an overview of turbulence measurements and ambient conditions during LASER from January 19 2247 UTC to February 14 0907 UTC 2016.

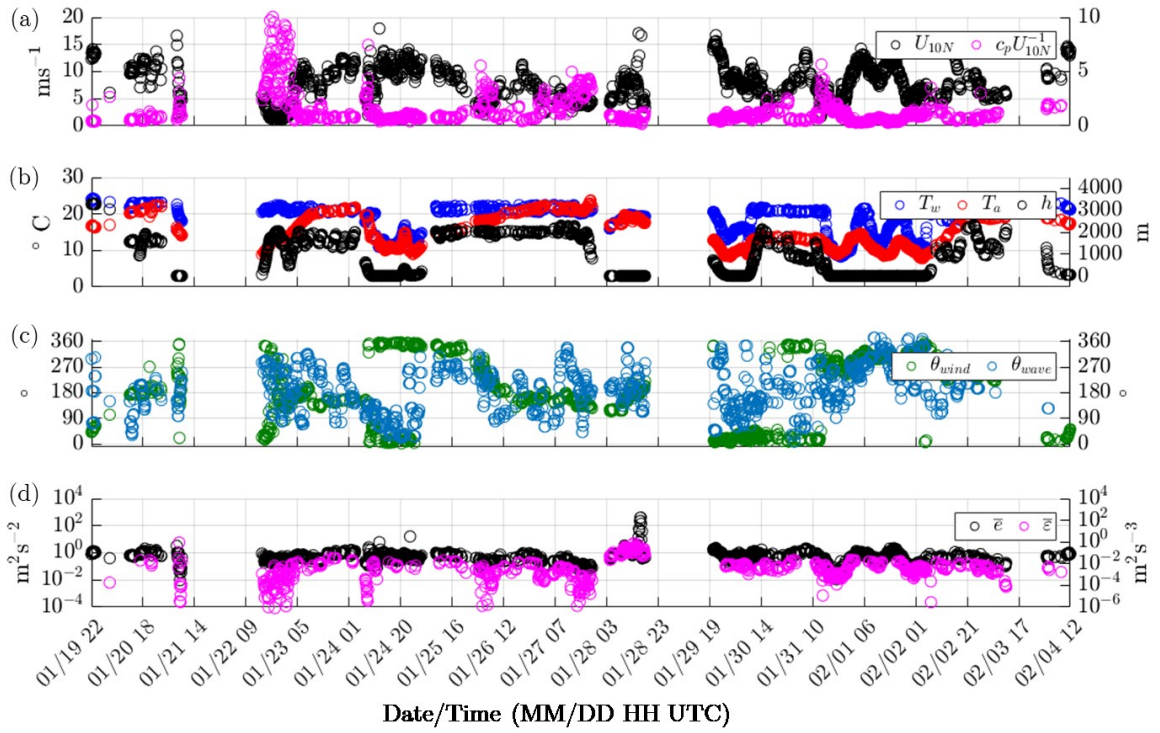


Figure 3.1 Summary of meteorological and oceanographic conditions during the LAgrangian Submesoscale ExpeRiment (LASER) from January 19 2247 – February 14 0907 UTC 2016. (a) 10-meter equivalent wind speed U_{10N} and wave age $c_p U_{10N}^{-1}$ after Pierson and Moskowitz (1964), (b) Water temperature T_w and air temperature T_a and water

depth h , (c) wind and wave direction relative to ship heading, and (d) average TKE (\bar{e}) and average TKE dissipation rate $\bar{\varepsilon}$. All units are given in the figure.

FGWS encountered low to moderate 10-meter equivalent winds of $U_{10N} = 0.71\text{--}13.78 \text{ ms}^{-1}$ (1.4–26.8 knots or 0-6 Beaufort wind scale), over a range of water depth $h = 2\text{--}3308$ meters. Deeper, warmer, and more saline waters ($\bar{T}_w = 21.1 \pm 0.99$ degrees Celsius for $h \geq 500$ meters) were observed over the open ocean in the Gulf of Mexico, whereas fresher, colder ($\bar{T}_w = 15.2 \pm 3.77$ degrees Celsius for $h < 500$ meters) water coming from the Mississippi River outflow was seen in shallower waters.

Sea-air temperature disequilibrium ΔT_{w-a} was positive, or conducive to ocean to atmosphere heat fluxes in both deep ($\Delta \bar{T}_{w-a} = 3.77 \pm 3.81$ degrees Celsius) and shallow ($\Delta \bar{T}_{w-a} = 3.49 \pm 3.16$ degrees Celsius) water. Wind and wave directions were predominantly well aligned, with the absolute difference angle $|\theta_{wind} - \theta_{wave}| = 8.54 \pm 5.57$ degrees. Median wave age given the dominant wave phase speed was $\langle c_p U_{10N}^{-1} \rangle = 0.95 \pm 1.57$, with 65.4 percent of wave fields characterized as windsea ($c_p U_{10N}^{-1} < 1.2$) and 32.7 percent identified as swell ($c_p U_{10N}^{-1} \geq 1.2$; Pierson and Moskowitz, 1963).

Average TKE and dissipation rate (Figure 3.1d) qualitatively agree in behavior as greater TKE supports larger dissipation rates, and the two quantities are well correlated ($R^2 = 0.64$). Both the average TKE and dissipation rate exhibit covariance with wind speed U_{10N} ($R^2 = 0.80$), wave age ($R^2 = -0.46$) and water-air temperature disequilibrium ($R^2 = 0.52$) throughout the timeseries – it is expected that both will respond to eddy fluxes of heat and momentum, which contribute to TKE production whereas their relative

contributions need be ascertained through evaluation of stability. We explore these considerations later in this chapter.

A more thorough evaluation of sea conditions observed during LASER was necessary to quality control water surface elevations and their spectra relative to expected spectral slopes (e.g. f^{-4}) for waves (Pierson and Moskowitz, 1964; Donelan, et al. 1985; Hwang, 2019). Therefore, water surface elevation timeseries were de-spiked, converted to spectra, and plotted according to wave age in Figure 3.2b along with a reference f^{-4} curve. Based on the dominant wave phase speed c_p from each series, a mapping of the wave regime according to depth as shallow ($Lh^{-1} > 20$), intermediate ($20 \geq Lh^{-1} > 2$), or deep ($Lh^{-1} \leq 2$) is shown in Figure 3.2a.

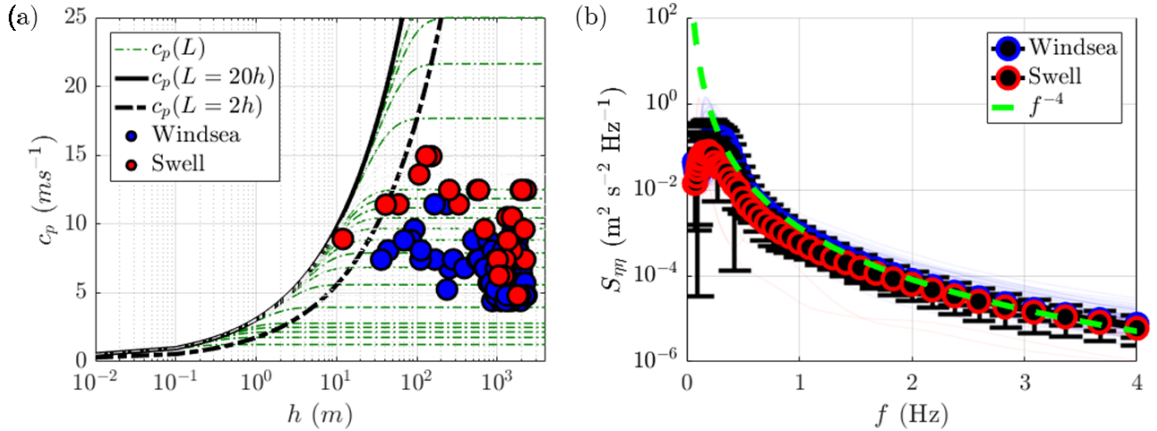


Figure 3.2 Sea conditions during LASER (2016). (a) Dominant wave phase for each wave spectrum as a function of water depth. The green dashed lines correspond to different wavelength values L . The black thick lines segregate shallow, intermediate, and deep water conditions according to dominant wave aspect ratio. (b) Water surface elevation spectra plotted in semi-logarithmic coordinates with their median plotted in the heavy lines. The green dashed curve corresponds to f^{-4} .

From Figure 3.2b, it is clear that the quality-controlled water surface (wave) elevation spectra (one from each 10 minutes of $\eta(t)$ data, with spectra also averaged over windsea and swell conditions) are similar to each other in shape consistent with fully

developed seas as described in Pierson and Moskowitz (1964), with greater variance at frequencies less than $f = 0.5$ Hz. The separation frequency $f_1 = g2\pi^{-1}1.2U_{10N}$ (Potter, 2015) was calculated for each omnidirectional wave spectrum and the ratio of the windsea part (E_w) and swell part (E_s) were also calculated.

Windsea spectra have an average dominant wave frequency of $\bar{f}_{ws} = 0.21 \pm 0.08$ Hz with average significant wave height of 1.57 meters and dominant wavelength of 35.3 meters, while spectra from swell dominant wave conditions have an average dominant wave frequency of $\bar{f}_s = 0.14 \pm 0.05$ Hz, significant wave height of 1.19 meters, and average dominant wavelength of 70.6 meters. Mean 10-meter equivalent neutral wind speed was $\overline{U_{10N,ws}} = 9.28 \pm 2.34$ ms⁻¹ in windsea and $\overline{U_{10N,s}} = 5.84 \pm 1.98$ ms⁻¹ in swell, respectively.

Mean integrated wave spectral density for windsea ($E_w = \int S_{\eta\eta,ws} = 7.54$ m²s⁻²) exceeds that for swell ($E_s = \int S_{\eta\eta,s} = 3.36$ m²s⁻²) by 124.5 percent. The mean spectral slope error for windsea and swell wave conditions is 5.52 and 6.85 percent, respectively. Based on water depth and wavelength, all of the observed waves were, in the context of their dominant wave, in a deep water (58.6 percent), intermediate (31.9 percent), shallow water (8.3 percent) regime. The remaining 1.3 percent of water surface elevation data contained greater than 5 percent (30 seconds worth) not-a-number (NaN) dropout values, thus the entire timeseries segment in such cases and subsequent spectra were not-a-number (NaN).

3.2 Flux observations

Fluxes of momentum and heat were calculated using both eddy covariance (Burba and Anderson, 2007) and bulk algorithms known as the Coupled Ocean-Atmosphere Response Experiment (COARE) version 3.5 (Edson, et al. 2013). Flux ogives (Friehe et al.

1991; French et al. 2007) of the zonal momentum flux were calculated from each 10-minute segment of velocity data from the upper-most starboard sonic anemometer and normalized by the zonal eddy momentum flux ($Og_{uw}/\overline{u'w'}$), which dominates over meridional momentum fluxes by up to an order of magnitude ($|\overline{u'w'}| / |\overline{v'w'}| > 1$ in 82.4 percent of data). These ogives are shown in Figure 3.3a and color-coded according to being from windsea-dominated or swell-dominated conditions. Using the cospectrum information from the calculation of the ogives, the percent of turbulence captured was also calculated and is shown in Figure 3.3b. Both ogives and percent turbulence are given in terms of the period, or length of time, of the data considered in seconds.

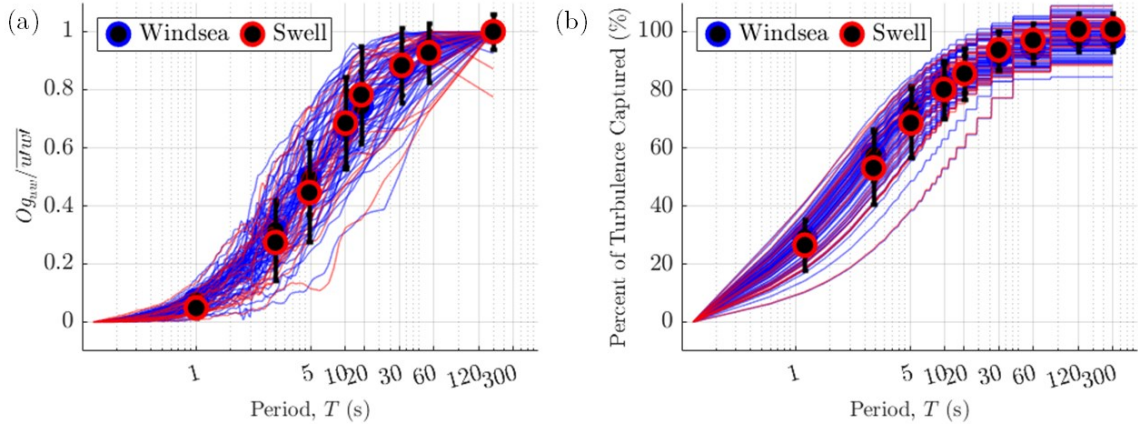


Figure 3.3 (a) Zonal momentum flux ogives for windsea (blue) and swell (red) wave conditions during LASER (2016), with the binned mean and standard deviation according to length of data overlaid (b) Percent of turbulence captured considering the cospectrum of zonal and vertical velocity perturbations, with color-coding as in the left panel.

Based on the ogive analysis, a duration of 2.86 minutes (2 minutes, 52 seconds) was needed to capture 99.9 percent of the turbulence characterized in the velocity cospectra. Considering the ogive represents the cumulative distribution of zonal momentum flux according to scale, the turbulent motions corresponded to a timeframe of 0.99 – 109.1 seconds (5th – 95th percentile of ogives). Clearly, the 10-minute length of each velocity data

segment was sufficient. Ogives that monotonically increased and approach an asymptote near 1.00 were retained (35.5 percent of fluxes from windsea conditions and 25.6 percent of fluxes from swell conditions), while those potentially contaminated by atmospheric mesoscale and wave motions were discarded (e.g. Zhao, et al. 2017; their Figure 2).

Momentum, sensible heat and latent heat fluxes were compared using linear regression similar to Edson and Fairall (1998) (see their Figure 1) in Figure 3.4 below.

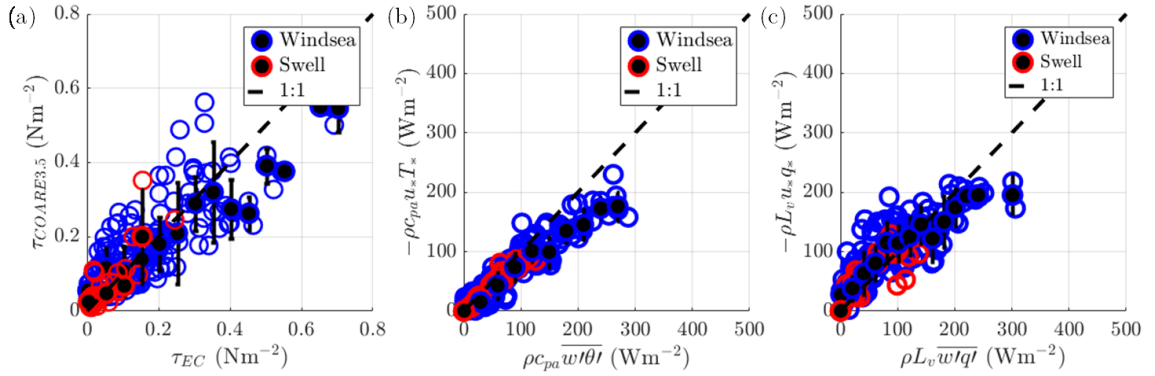


Figure 3.4 (a) Wind stress τ from eddy covariance (EC) method and based on COARE 3.5 bulk algorithm color-coded by wave condition (b) Sensible heat flux and (c) latent heat flux. A black dashed 1:1 line is also given in each plot. Binned mean and standard deviation are included in each plot. Units are Nm^{-2} in (a) and Wm^{-2} in (b) and (c).

Flux comparisons demonstrate fair agreement between EC and COARE 3.5 bulk values, with larger average fluxes in windsea conditions ($\bar{\tau}_{ws} = 0.173 \text{ Nm}^{-2}$, $\bar{H}_{sf,ws} = 75.83 \text{ Wm}^{-2}$, $\bar{H}_{lf,ws} = 73.62 \text{ Wm}^{-2}$) than swell conditions ($\bar{\tau}_s = 0.048 \text{ Nm}^{-2}$, $\bar{H}_{sf,s} = 33.42 \text{ Wm}^{-2}$, $\bar{H}_{lf,s} = 35.03 \text{ Wm}^{-2}$). COARE 3.5 bulk values underestimate measured values of wind stress in shallow water conditions. Linear regression correlation coefficients for wind stress, sensible flux, and latent flux comparisons were $R^2 = 0.80$, $R^2 = 0.96$, and $R^2 = 0.85$, respectively.

3.3 Dissipation rate measurements

TKE dissipation rates were calculated using velocity spectra from each flux tower mounted sonic anemometer aboard R/V *F.G. Walton Smith*, and quality-controlled to eliminate inclusion of turbulent wake eddies instigated by geometric structural flow distortion (Kaimal 1979; Wyngaard and Zhang, 1985; Friebel et al. 2009), velocity spectra sufficiently lacking isotropic convergence to $R_{uw} = S_{uu} S_{ww}^{-1} = 4/3$ over the 2–4 Hz prescribed inertial sub-range, and velocity spectra with inertial sub-range slope errors exceeding 25 percent relative to $f^{-5/3}$. Velocity data was eliminated where ship heading minus mean wind direction (HMWD) was greater than 70° to port or starboard of R/V *F.G. Walton Smith*, and where the isotropic convergence ratio of orthogonal velocity spectra takes values $5/3 < R_{uw} \cup R_{uw} < 3/4$. Satisfaction of Taylor's frozen turbulence hypothesis was evaluated via

$$\sqrt{\bar{u'^2}} / \bar{U}_{adv} < 0.2 \quad (3.1)$$

where the numerator of (3.1) is the root-mean-square (RMS) of the turbulent velocity and the denominator is an advection velocity for the turbulence, or mean flow velocity. After quality-control, 45.3 percent (733 of 1617 spectra) were retained, with 87.5 percent of these being in windsea conditions, and 12.5 percent in swell. Average values for (3.1) were 0.108 ± 0.02 given $\bar{U}_{adv,ws} = 7.82 \text{ ms}^{-1}$ in windsea, and 0.109 ± 0.10 given $\bar{U}_{adv,s} = 4.97 \text{ ms}^{-1}$ in swell. Figure 3.5 shows quality-controlled velocity spectra from the port and starboard flux towers of FGWS relative to the theoretical inertial sub-range slope $f^{-5/3}$ and the Taylor's frozen turbulence ratio from (3.1) as a function of 10-meter drag coefficient.

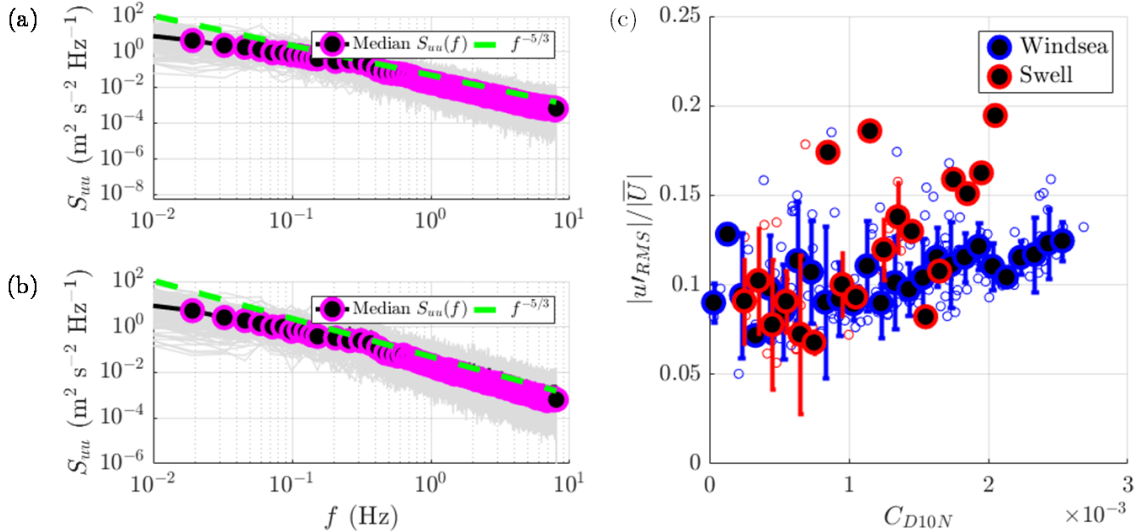


Figure 3.5. Zonal velocity spectra ($\text{m}^2 \text{s}^{-2} \text{Hz}^{-1}$) derived from 10-minute velocity timeseries from the (a) port and (b) starboard sonic anemometers during LASER. The gray solid lines in (a) and (b) show individual spectra. The per-frequency-bin median is shown by magenta circles. The solid lime green line is the $f^{-5/3}$ slope line for the inertial subrange. (c) The Taylor's frozen turbulence ratio given by (3.1) as a function of drag coefficient.

3.3.1 Dissipation rates from different regimes and platforms

TKE dissipation rates measured during LASER (2016) as reported in Smith, Haus, and Zhang (2019) were observed in a low to moderate wind and explicitly non-hurricane environment where $U_{10N} \leq 16.7 \text{ ms}^{-1}$ (37.4 mph). Since eddy momentum fluxes, mean surface layer shear and stability differ substantially in non-hurricane and hurricane environments, we compared our ship-derived low-wind data to NOAA WP-3D Orion aircraft-derived data collected as part of the Coupled Boundary Layers Air-Sea Transfer Experiment (CBLAST; Zhang, 2010) in Hurricanes Edouard, Isidore, and Lili (2002) and Hurricanes Fabian and Isabel (2003). The path of such a reconnaissance flight through Hurricane Fabian (2003) as observed by GOES-12 visible satellite, and the associated measurement altitudes in meters is given in Figure 3.6.

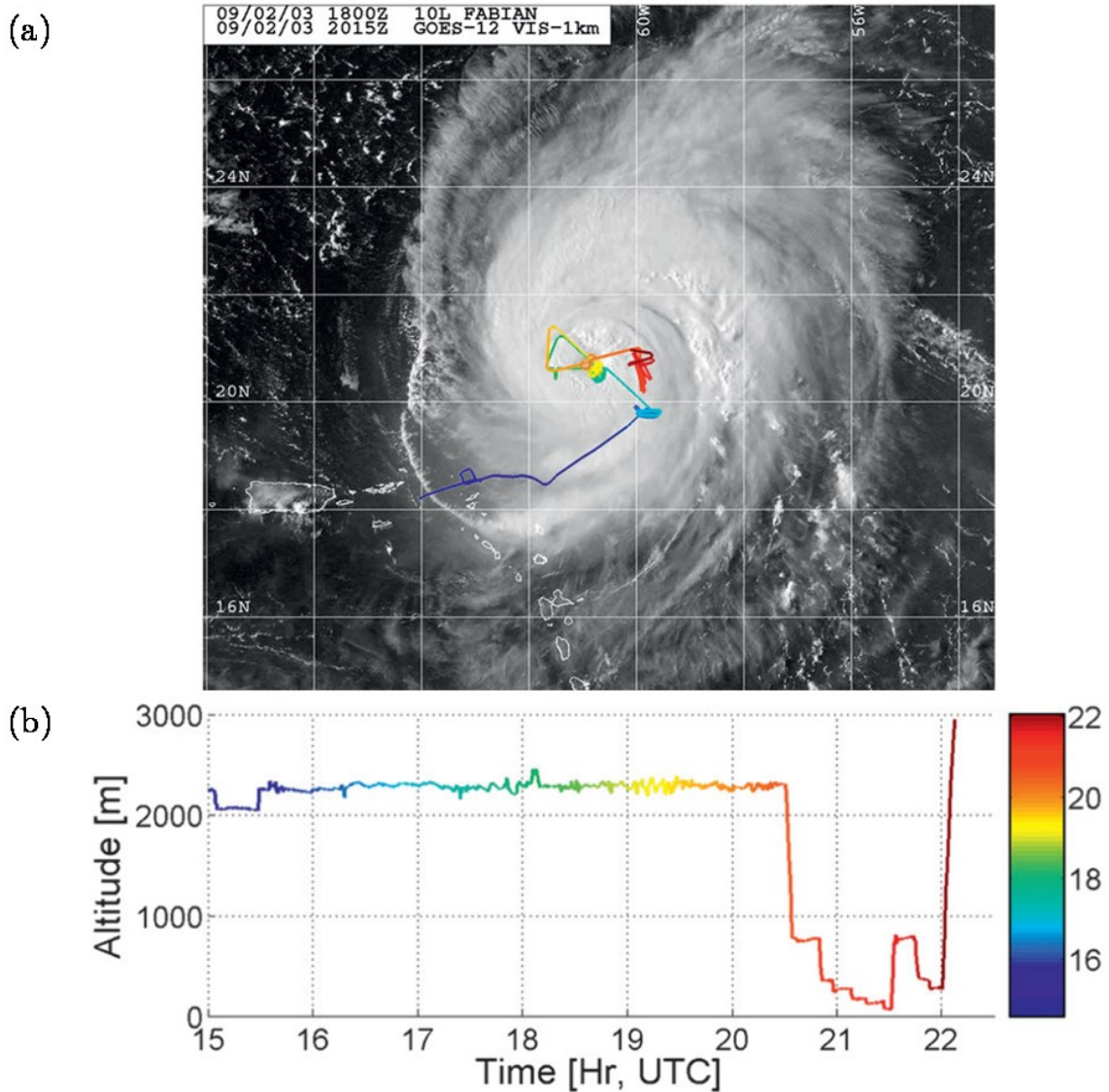


Figure 3.6. Plots of horizontal aircraft track superimposed on top of a *GOES-12* image and the aircraft altitude in color varying with time (UTC). The measurements were taken on September 2003 in Hurricane Fabian. Image is courtesy of the Naval Research Laboratory, Monterey, CA. Figure and caption from Zhang (2010).

Zhang (2010) measured 49 estimates of average TKE dissipation rate $\bar{\varepsilon}$, momentum flux (surface stress) $\tau = \rho(-\bar{u}'w'\mathbf{i} - \bar{v}'w'\mathbf{j})$ and 10-meter neutral drag coefficient C_{D10N} in hurricane atmospheric boundary layers with 10-meter equivalent wind speed $U_{10N} = 11.6 - 28.7 \text{ ms}^{-1}$ ($25.9 - 64.2 \text{ mph}$) at heights $z = 53 - 197 \text{ meters}$ above sea level.

A ‘dissipative heating’ flux term $D_\varepsilon = \rho\bar{\varepsilon}z_1$ was also calculated and is considered in the next section. Wind stress and 10-meter drag coefficient are compared for the two regimes and platforms in Figure 3.7.

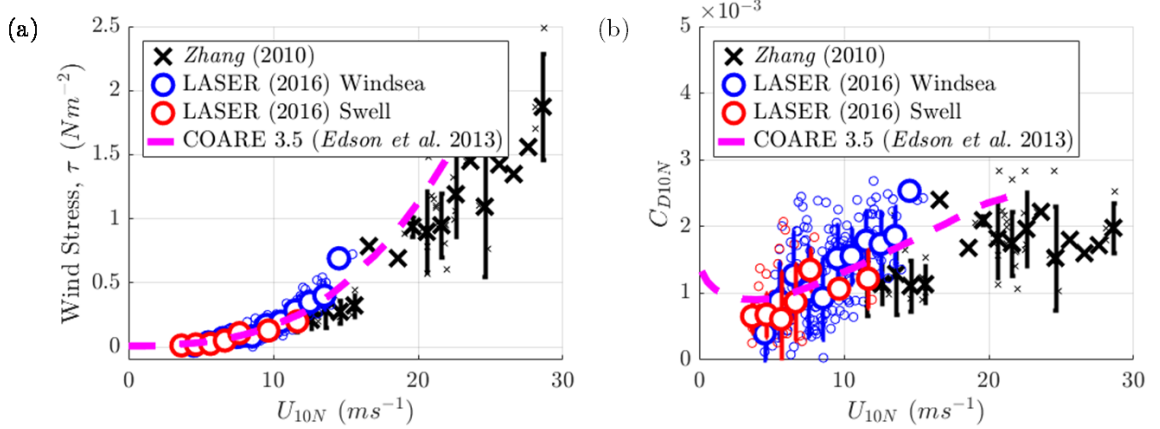


Figure 3.7. (a) Wind stress and (b) 10-meter neutral drag coefficient $C_{D10N} = u_*^2 U_{10N}^{-2}$ from LASER (Smith, Haus, and Zhang, 2019) in circles and CBLAST (Zhang, 2010) in \times s. The magenta lines are the average data from Edson, et al. (2013). Error bars are one standard deviation.

Wind stress $\tau = \rho u_*^2$ and 10-meter neutral drag coefficient from LASER data (Smith, Haus, and Zhang, 2019) were calculated following Donelan (1990) and Anctil and Donelan (1996). From Figure 3.7a, it is clear that measured wind stress from the two experiments jointly occupy a quadratic curve becoming linear for the Zhang (2010) data above approximately $U_{10N} = 20\text{ ms}^{-1}$. Average wind stress in the two datasets is $\bar{\tau}_{SHZ19} = 0.163\text{ Nm}^{-2}$ and $\bar{\tau}_{Z10} = 0.909\text{ Nm}^{-2}$, respectively. Wind stress from LASER (2016) and COARE 3.5 (Edson, et al. 2013) compare well, with $R^2 = 0.97$.

The 10-meter neutral drag coefficient from the combined datasets follows a roughly cubic fit shown in Figure 3.7b from a ‘minimum turbulent’ value of $C_{D10N} = 0.65 \times 10^{-3}$ at $U_{10N} = 3.66\text{ ms}^{-1}$ to a roughly level saturation value of $C_{D10N} = 2.22 \times 10^{-3}$ at

approximately $U_{10N} = 23.6 \text{ ms}^{-1}$. Although this is admittedly a lower a saturation value for the drag than that found in laboratory (Curcic and Haus, 2020) and from GPS dropsonde measurements (Powell, et al. 2003), and in spite of the scatter of the drag in Zhang (2010) data, the behavior of the curve is consistent with aforementioned literature. Regardless, average wind stress and drag coefficient values are larger in windsea than swell wave conditions by 177.1 and 52.9 percent, respectively. As wind stress characterizes the degree of momentum flux and the drag coefficient quantifies the efficiency of such flux, we next compare the average TKE dissipation rate $\bar{\varepsilon}$ measured in the two environments given that the shear production and thus dissipation rate of TKE (through closure) respond to eddy momentum fluxes. TKE dissipation rate is shown for both datasets as a function of 10-meter wind speed and drag coefficient in Figure 3.8.

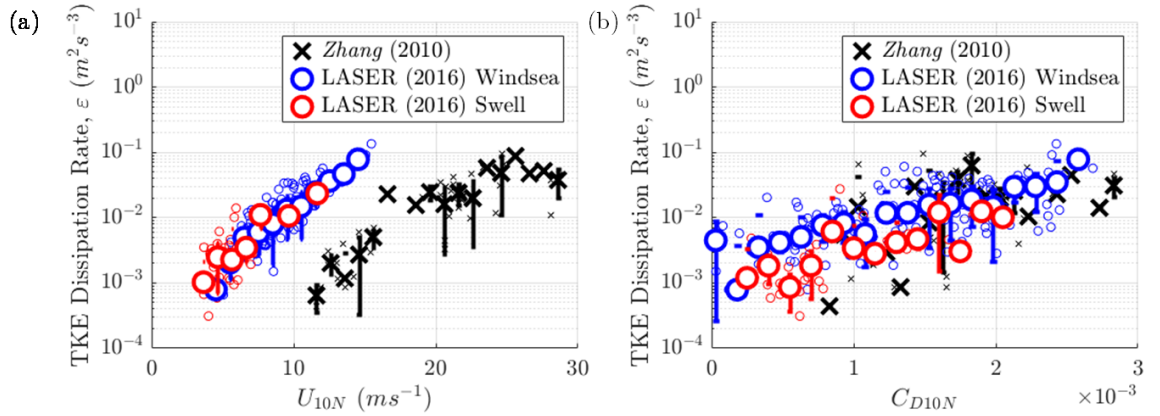


Figure 3.8. Turbulent kinetic energy (TKE) dissipation rate (m^2s^{-3}) as a function of (a) 10-meter neutral wind speed and (b) drag coefficient. Blue and red circles indicate the LASER (2016) windsea and swell condition data, respectively. Large circles indicate binned averages, with error bars giving the standard deviation. Data from Zhang (2010) is given in black \times s as in Figure 3.7. In both panels, the y-axis is plotted in logarithmic scale.

As expected, in Figure 3.8 (a), the TKE dissipation rate values from the lower-wind LASER (Smith, Haus, and Zhang 2019) and the CBLAST hurricane environment (Zhang, 2010) do not overlap given the difference in the wind conditions. However, the behavior

of the scatter where data is sufficient is similar, and the values themselves occupy a similar range. That is, $\bar{\varepsilon}_{SHZ19} \approx 7.9 \times 10^{-4} - 7.8 \times 10^{-2} \text{ m}^2\text{s}^{-3}$ and $\bar{\varepsilon}_{Z10} \approx 4.4 \times 10^{-4} - 6.3 \times 10^{-2} \text{ m}^2\text{s}^{-3}$ with a percent error in those two ranges of values of 24.4 percent.

In juxtaposition, when TKE dissipation rates are shown as a function of 10-meter drag coefficient in Figure 3.8 (b), the two datasets visibly overlap. From the TKE budget (equation 1.2), Shear production of TKE is explicitly governed by the magnitude of eddy momentum fluxes relative to the vertical profile of mean wind; such a comparison is included between turbulence kinetic energy and mean kinetic energy in the drag coefficient as $C_{D10N} = u_*^2 U_{10N}^{-2}$. Average TKE dissipation rates measured over windsea conditions were 236 percent larger than those in swell conditions, where average 10-meter drag coefficient values were 1.4×10^{-3} and 9.2×10^{-4} , respectively. It is clear therefore from the lack of monotonic overlap in LASER and CBLAST data in Figure 3.8(a) that U_{10N} alone is insufficient to parameterize dissipation rate in the two environments, and that the adequate parameterization must include proxies of both eddy flux and mean vertical structure of the surface layer environment.

3.3.2 TKE dissipation as a surface layer heat flux

While the results from a comparison of dissipative heating measurements in explicitly different atmospheric surface layer environments was a motivating impetus for Smith, Haus, and Zhang (2019), the focus of this dissertation is more broadly TKE and its dissipation rate. Nevertheless, we give a brief account of the dissipative heating here as it pertains to hurricanes as context for the comparison of this ‘dissipative heating’ we make between Zhang (2010) and Smith, Haus, and Zhang (2019) datasets in this section. Dissipative heating was first introduced by Bister and Emanuel (1998) and thought to be

an important additional heat flux term in the hurricane energy budget and thereby that dissipation of TKE provided an additional source of heat for hurricane intensification. This model for steady TCs included dissipative heating that was excluded in Emanuel (1986) and extended the model domain toward the surface to include the ASL. The original model had been based on the Carnot cycle model for hurricane energetics, whereby hurricane maximum potential intensity (MPI) is related to the vertical temperature gradient at surface and outflow heights. Dissipative heating was therefore treated as entirely recycled as a heat source by Bister and Emanuel (1998). Their formulation was added to a turbulent enthalpy flux term to balance radial advection of equivalent potential temperature,

$$c_p \psi_b \frac{\partial \ln \theta_e}{\partial r} = \frac{1}{T_S} \left(\tau_{k0} + \frac{1}{g} \int_{p_b}^{p_0} D dp \right) \quad (3.2)$$

and ultimately was parameterized as related to the cube of the 10-meter equivalent neutral wind speed as

$$\frac{1}{g} \int_{p_b}^{p_0} D dp = \mathcal{D} \quad |V|^3 \quad (3.3)$$

In a critical review on the subject of dissipative heating, Kieu (2015) described an equivalent to (3.3) as the full frictional work done when turbulent kinetic energy is dissipated,

$$F_{diss} \approx -2\pi C_D \int_0^{R_0} \rho |V|^3 r dr \quad (3.4)$$

However, Kieu (2015) and Smith, Haus, and Zhang (2019) reaffirm that (3.4) is not equal to the dissipative heating because the ASL uses this work to (1) internally warm the ASL via dissipative heating, (2) contribute to surface ocean wave growth and subsequently sea spray and (3) do work on the upper ocean surface layer such that energy is conveyed to surface currents. An estimate of the fractioning of (3.4) into these sinks is described in Richman and Garrett (1977) and is not

discussed here. As previously stated, Zhang (2010) used the average TKE dissipation rate to compute dissipative heating as an alternative to (3.3) via

$$D_\varepsilon = \rho \bar{\varepsilon} z_1 \quad (3.5)$$

which has units of air density multiplied by energy per time multiplied by z_1 which is a length-scale equivalent to the height of the ASL. Zhang (2010) chose $z_1 = 200$ meters in (3.5) and claim that statistical t-test analysis of $\bar{\varepsilon}$ with height z found no statistical dependence of it with height to 95 percent confidence. However, given that Zhang (2010) measurements were taken in the near-neutral hurricane boundary layer (HBL) environment, this is unsurprising. Nevertheless, given the true ASL height over the Gulf of Mexico sampled during LASER was likely shallower than the HBL sampled during Zhang (2010), we chose $z_1 = 125$ meters based on multi-decadal ECMWF reanalysis climatological-average planetary boundary layer (PBL) heights for December–February (Von Engeln and Teixeira 2013, see their Figure 5). The specific value was taken from the region south of the central Gulf of Mexico near the LASER study site, assuming the ASL height is 10 percent of the PBL height. Dissipative heating is compared between the LASER and CBLAST datasets using both (3.3) and (3.5) in Figure 3.9.

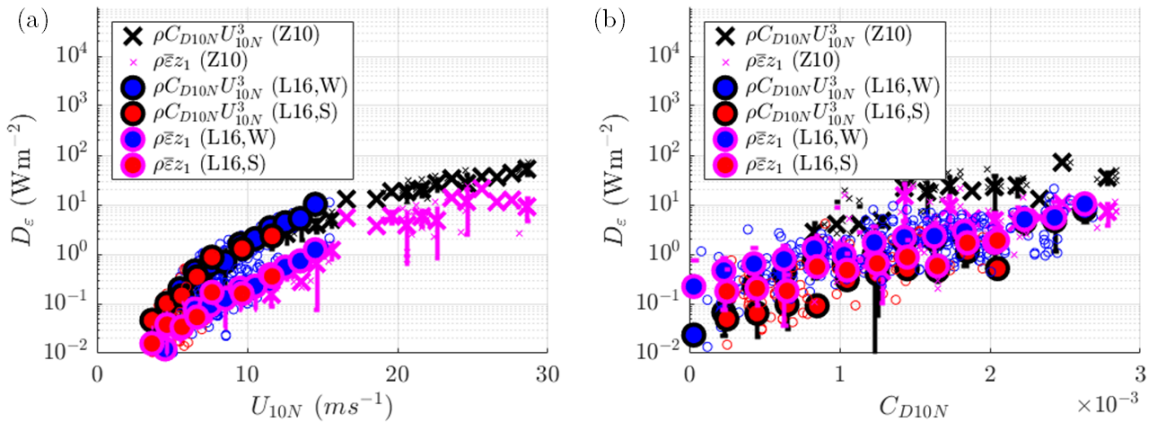


Figure 3.9. Dissipative heating (W m^{-2}) measurements as a function of (a) U_{10N} using the theoretical equation $\rho C_{D10N} U_{10N}^3$ from Bister and Emanuel (1998) and from explicitly measured TKE dissipation rates via $\rho \bar{\varepsilon} z_1$ after Zhang (2010). In both panels, the circles and \times s indicate data from LASER and CBLAST (Zhang, 2010), respectively. Large

markers indicate the median of binned data, with error bars denoting standard deviation. In both panels, the y -axis is plotted in logarithmic scale.

Dissipative heating generally increases with wind speed regardless of the computation method used; however, the magnitude of D_ε is different and larger when the theoretical formulation of Bister and Emanuel (1998; BE98) is used. In Figure 3.9a, considering the combined datasets presented, dissipative heating magnitude via BE98 increases from 0.01 to 52.7 Wm^{-2} over a range of 24.94 ms^{-1} 10-meter equivalent wind speeds, or an energy density rate of $2.11 \text{ Wm}^{-3}\text{s}$ (Jm^{-3}). Conversely, when using dissipation rate explicitly as in Zhang (2010; Z10) over the same range of U_{10N} , the energy density rate is just $0.36 \text{ Wm}^{-3}\text{s}$, a reduction of 82.7 percent. Similar to Figure 3.8, in panel (b) the dissipative heating measurements are compared according to method of calculation with the 10-meter neutral drag coefficient C_{D10N} .

As with TKE dissipation rate, the dissipative heating values overlap more as opposed to separating into two curves based on dataset or calculation method. Dissipative heating per drag coefficient value can be thought of as the heat resulting from the dissipation of TKE given the momentum flux efficiency from atmosphere to ocean. For the LASER data using the explicit TKE dissipation rate formula, $D_\varepsilon \approx 1.297C_{D10N}^3 - 1.6$ while the CBLAST data (Zhang, 2010) follow $D_\varepsilon \approx 1.311C_{D10N}^3 - 1.1$. Slope error between the two datasets is 1.1 percent. Conversely, if one uses the formula from BE98, $D_\varepsilon \approx 1.884C_{D10N}^3 - 3.0$ and $D_\varepsilon \approx 1.381C_{D10N}^3 - 0.23$ for the LASER and CBLAST data, respectively. Slope error between these two linear fits to the data is 26.7 percent.

Although the sample size is smaller and therefore data variance is larger, this suggested to me that parameterizations involving turbulence or dissipation should be

physically constrained as opposed to increasing seemingly unbounded as with $D_\varepsilon = \rho C_D U_{10N}^3$ (see also Businger and Businger, 2001). To that end, threshold percentages for how much theoretical dissipative heating is added back to the atmosphere have been implemented in hurricane numerical weather prediction models such as the Geophysical Fluid Dynamics Laboratory (GFDL) and the Hurricane Weather Research and Forecasting (HWRF; Tallapragada et al. 2013).

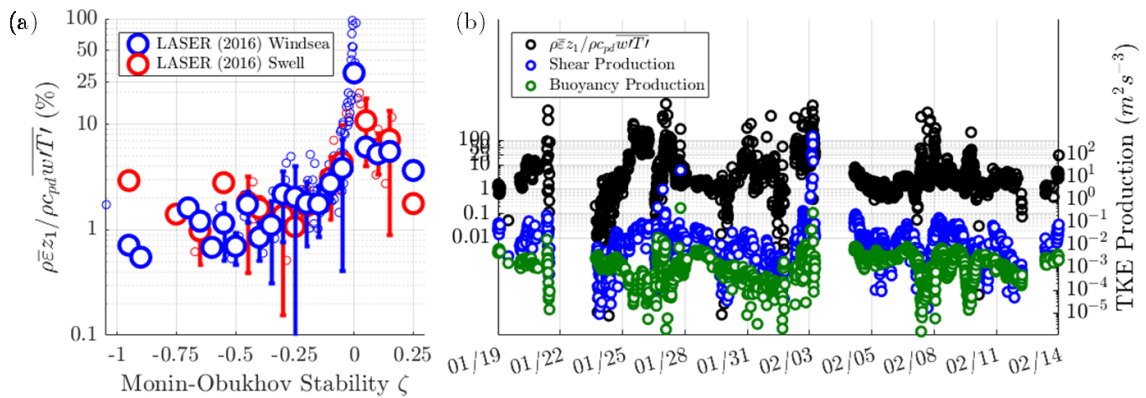


Figure 3.10. (a) Ratio of dissipative heating (heat flux) and sensible heat flux (percentage, %) as a function of Monin-Obukhov stability $\zeta = zL_\zeta^{-1}$ (b) Timeseries depiction of the ratio of dissipative and sensible heat fluxes (black, %), shear production of TKE (blue) and buoyancy production of TKE (green). The TKE production terms are given in $m^2 s^{-3}$. The x-axis is the date (MM/DD).

In Figure 3.10, we examine how dissipative heat flux compares with a typical buoyancy-driven bulk flux such as sensible heat flux. Although under most conditions, it is expected that bulk fluxes of sensible and latent heat have greater magnitude than the heat resulting from TKE dissipation (Zhang 2010; Kieu, 2017), we seek to know what conditions if any would permit the largest contributions from a dissipative heat flux term. A ratio of the dissipative and sensible heat flux, $\rho\bar{\varepsilon}z_1/\rho c_{pd}\bar{w'T'}$, is given in panel (a) above as a function of Monin-Obukhov stability ζ . Clearly, the ratio is small (order of 1

percent) for most values of stability however exceeds 10 percent for $|\zeta| \leq 0.05$ or essentially neutral conditions. In panel (b), the timeseries of the heat flux ratio, TKE shear production and TKE buoyancy production terms are compared to demonstrate the physical correlation between them. Where $\rho \bar{\epsilon} z_1 / \rho c_{pd} \bar{w'} T' \geq 10\%$, the average value of the ratio of shear to buoyancy production ($-L_\zeta$) is 2.53×10^3 . That is, it is apparent that the ratio of heat flux terms favors the largest contributions from dissipative heating when TKE shear production is large and TKE buoyancy production is small. Considering this, we next consider a simplified TKE budget balance and compare low-wind ASL and higher-wind HBL measurements in that context.

3.3.3 Dissipation rates in windsea and swell

As a simplifying assumption, Zhang (2010) and many others have reduced the TKE budget to a balance of shear production and dissipation terms. In so doing, buoyancy production or suppression, turbulent transport, and pressure work are taken to be negligible in the near-neutral stability ASL (or HBL) where stratification and vertical velocity gradients (convection or subsidence) are very small. Hence, the TKE budget in the ASL reduces to

$$-\overline{u'w'} \frac{\partial \bar{U}}{\partial z} = u_*^2 \frac{u_*}{\kappa z} = \frac{u_*^3}{\kappa z} = \varepsilon \quad (3.6)$$

where (3.6) includes the horizontal homogeneity and stationarity assumptions of Monin-Obukhov similarity theory (MOST; Monin and Obukhov, 1954). Although (3.6) and MOST are not expected to be valid in swell conditions (Hogstrom, 1996; Sjöblom and Smedman, 2002; Höglstrom, et al. 2009), we compare the measured TKE dissipation rates from windsea and swell conditions separately to the simplification in (3.6) in Figure 3.11.

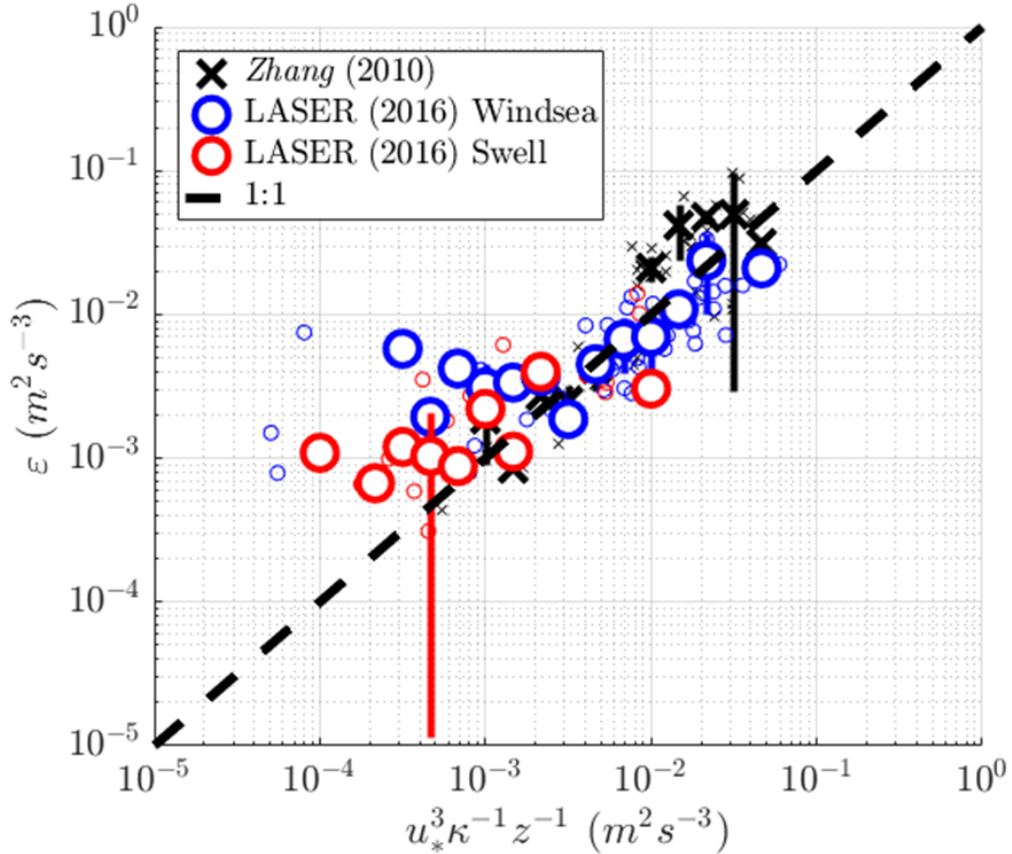


Figure 3.11. TKE dissipation rate (m^2s^{-3}) from LASER as a function of the Monin-Obukhov shear production $u_*^3 \kappa^{-1} z^{-1}$ in windsea (blue) and swell (red) wave conditions. Data from Zhang (2010) is included as black \times s. The 1:1 line where $\bar{\varepsilon} \equiv u_*^3 \kappa^{-1} z^{-1}$ is shown in thick black dashed lines.

Figure 3.11 above is adapted from Zhang (2010) Figure 8, depicting the balance between TKE shear production and dissipation rates at an average physical height of 5.34 meters and 143.8 meters above mean sea level during LASER and CBLAST, respectively. Zhang (2010) found balance between the two terms to occur for $U_{10N} = 10 - 20 \text{ ms}^{-1}$ and an imbalance in which dissipation exceeds production for higher wind speeds, an imbalance which is attributed to the nonlinear horizontal advection term in the TKE budget and thought to be significant to that budget in the HBL. As the LASER data was not collected in the HBL, we did not expect such an imbalance, however, there are imbalances observed.

In swell and low wind conditions (I), dissipation exceeds production and $\langle \varepsilon u_*^{-3} \kappa z \rangle = 3.79 \pm 1.43$. The median wave age is 1.96 for wind speed $\bar{U}_{10N} = 4.5 \text{ ms}^{-1}$. In moderate wind conditions (II), dissipation and production are in approximate balance, with $\langle \varepsilon u_*^{-3} \kappa z \rangle = 1.24 \pm 0.79$. Windsea and swell are observed and the average wind speed is $\bar{U}_{10N} = 7.1 \text{ ms}^{-1}$. Finally, at the high end of wind speeds (III) where $\bar{U}_{10N} = 10.3 \text{ ms}^{-1}$, production exceeds dissipation and $\langle \varepsilon u_*^{-3} \kappa z \rangle = 0.76 \pm 0.45$. Median wave age here is 0.64, where predominantly windsea conditions are observed. Average dissipation rates in windsea and swell conditions observed during LASER were $\bar{\varepsilon}_{ws} = 1.75 \times 10^{-2} \text{ m}^2 \text{s}^{-3}$ and $\bar{\varepsilon}_s = 4.72 \times 10^{-3} \text{ m}^2 \text{s}^{-3}$, respectively. These behaviors are consistent with results from long-term measurements performed in the Baltic Sea by Sjöblom and Smedman (2002).

Although (3.6) equates TKE shear production and dissipation in a neutral stability simplification of the TKE budget, in non-neutral conditions buoyancy production may aid or suppress in the production of TKE. Buoyancy production of TKE is determined by the magnitude of the ambient stratification $g\bar{\theta}^{-1}$ relative to heat and moisture fluxes associated with convection or subsidence. Monin-Obukhov stability parameterizes these physics as a ratio of shear and buoyant production/suppression of TKE such that positive (negative) ζ indicate stable/subsiding (unstable/convective) vertical motion in the ASL. In the three regions (I, II, and III) of Figure 3.11 described earlier, the average Monin-Obukhov stability ζ is -0.571, -0.050, and -0.016, respectively. From Figure 3.10 however, even though the ASL is unstable in 77.2 percent of the data, it is clear that buoyancy production of TKE is much less than the shear production.

To conclude our comparison of TKE dissipation rates in different wave ages, we examine the values in the context of wave-scaled roughness $z_o H_{sig}^{-1}$ using three parameterizations described in Drennan et al. (2005). These will be denoted C55 (Charnock, 1955), D03 (Drennan, et al. 2003), and TY01 (Taylor and Yelland, 2001). The Charnock roughness length (Charnock, 1955) is,

$$z_o = \alpha u_*^2 g^{-1} \quad (3.7)$$

where $\alpha = 0.0112$ is the Charnock parameter, u_* is the friction velocity, and $g = 9.81 \text{ ms}^{-2}$.

Scaling the roughness length in (3.7) by significant wave height characterizes the sea state in terms of the wind stress or momentum flux in the ASL and by a statistical representation of the wave conditions present.

This $z_o H_{sig}^{-1}$ is parameterized for D03 in terms of inverse wave age as $z_o H_{sig}^{-1}_{D03} \approx u_* c_p^{-1}$ and in terms of wavelength of the dominant wave as $z_o H_{sig}^{-1}_{TY01} \approx H_{sig} L_p^{-1}$. Drennan et al. (2005) report $z_o H_{sig}^{-1}_{D03}$ performed better in strongly-forced conditions with dominant windsea conditions, while $z_o H_{sig}^{-1}_{TY01}$ was better suited for mixed seas and dominant swell conditions. A comparison of these two parameterizations using data from LASER (2016) and data from previous field experiments (Drennan et al. 2005; e.g. AGILE, FETCH, HEXOS, SWADE, WAVES, and RASEX) is given in Figure 3.12.

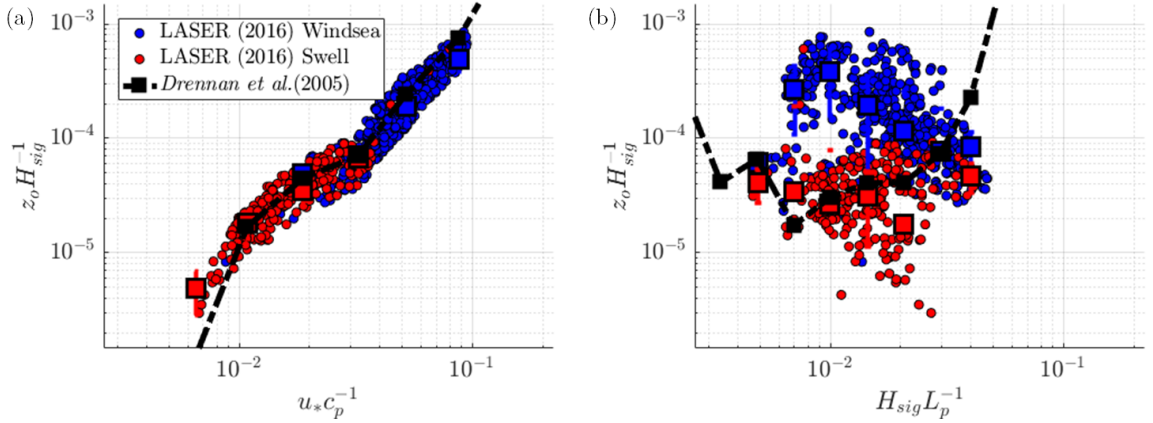


Figure 3.12 (a) Wave-scaled roughness using (3.7; C55) parameterized using the aforementioned D03 wave-age parameterization. (b) As in (a), except using YT01 steepness parameterization. In each panel, the black dash-dot line connects the binned average values (black squares) from Drennan et al. (2005). Blue and red circles indicate the LASER (2016) data in windsea and swell conditions, respectively. Binned average values are in colored squares.

Based on the discussion given in Drennan et al. (2005), we expect the comparison between LASER (2016) and Drennan et al. (2005) values for $z_o H_{sig}^{-1}$ to be of better quality using the wave-age parameterization (D03) for windsea conditions and the steepness parameterization (YT01) for swell conditions. In Figure 3.12(a), the qualitative agreement is reasonable between the LASER and Drennan et al. (2005) data, particularly as windsea values bunch together at high inverse wave age and high wave-scaled roughness. The binned average values have correlation coefficients of $R^2 = 0.98$ and $R^2 = 0.91$ for windsea and swell, respectively. In panel (b), the scatter of the LASER data is larger and the overlap with mean values from Drennan et al. (2005) is better for the swell data, where $R^2 = -0.48$ and $R^2 = 0.73$, respectively.

Dissipation of TKE predominantly created via shear (eddy momentum fluxes acting against the mean wind profile) is expected to be greatest in small wave age where wave-

scaled roughness is large. The evolution of the TKE dissipation rate and wave-scaled roughness parameterizations is shown in Figure 3.13.

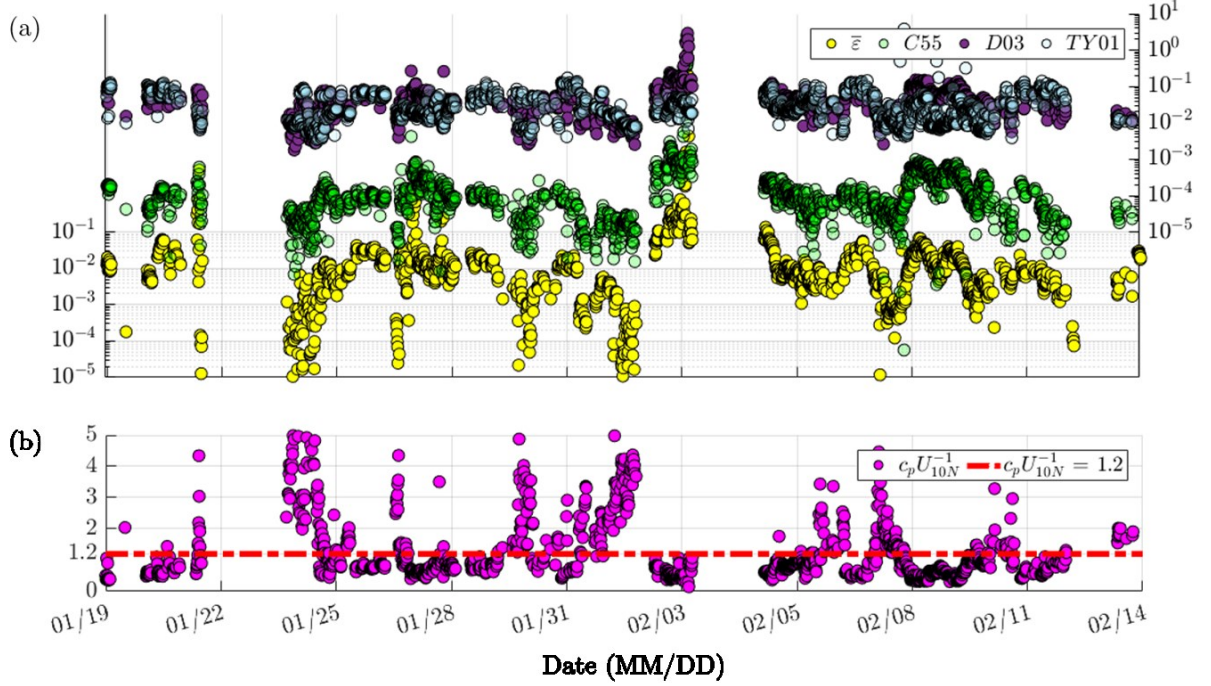


Figure 3.13 (a) TKE dissipation rate ($m^2 s^{-3}$) from LASER (yellow, left axis) and wave-scaled roughness $z_o H_{sig}^{-1}$ (dimensionless; green, right axis) parameterized via (3.7; C55), D03 (purple), and YT01 (steel blue). (b) Wave age with the Pierson and Moskowitz (1964) criterion value of 1.2 marked in red dot-dashed line. The x -axis is the date (MM/DD) of the measurements.

In Figure 3.12, TKE dissipation rates generally correlate with wave-scaled roughness and are inversely proportional to the wave age. Pearson correlation coefficients of $R^2 = 0.89$, $R^2 = 0.63$, and $R^2 = 0.27$ were found between $\bar{\varepsilon}$ and $z_o H_{sig}^{-1}$ for the three parameterizations C55, D03, and YT01, respectively. Average wave-scaled roughness using (3.7; C55) in windsea conditions was $\overline{z_o H_{sig}^{-1}}_{ws} = 1.46 \times 10^{-4}$ where $\overline{H_{sig}^{-1}} = 1.69 \text{ m}$, whereas in swell conditions $\overline{z_o H_{sig}^{-1}}_s = 3.78 \times 10^{-5}$ and $\overline{H_{sig}^{-1}} = 1.31 \text{ m}$. Given that the covariance of dissipation rate and wave-scaled roughness is most similar when using (3.7)

and the correlations of $u_* c_p^{-1}$ and $z_o H_{sig}^{-1}$ indicate good agreement with Drennan et al. (2005), it is clear that eddy momentum flux magnitude is dominating the influence wave heights have on the wave-scaled roughness plotted in Figure 3.13 (a). In the next section, we normalize each term in the TKE budget and discuss each term in the context of wave conditions and atmospheric stability encountered during the LASER (2016) campaign.

3.4 Normalized turbulent kinetic energy budget

Following Monin-Obukhov similarity theory (MOST; Monin and Obukhov, 1954), the TKE budget in the ASL can be normalized such that universal functions of Monin-Obukhov stability ζ alone can be used to parameterize each budget term. The normalization term is the scaling parameter $\kappa z u_*^{-3}$, where $\kappa \approx 0.41$ is the von Karman constant, and the parameter in its' entirety is the inverse of shear production of TKE. By choosing this as the scaling parameter, the buoyancy production of TKE is reduced to ζ and the TKE budget can be written, after Edson and Fairall (1998), as

$$\phi_m(\zeta) - \zeta - \phi_{te}(\zeta) - \phi_{tp}(\zeta) = \frac{\varepsilon \kappa z}{u_*^3} \quad (3.8)$$

Similarity relationships for each term in (3.1) as dimensionless functions of ζ were constructed using turbulent flux and dissipation rate estimates by Edson and Fairall (1998). We apply their relationships as follows to the measured ζ in windsea and swell from the data collected during LASER (Smith, Haus, and Zhang, 2019),

$$\phi_m(\zeta) = \begin{cases} 1 + 6\zeta & \zeta \geq 0 \\ (1 - 15\zeta)^{-1/3} & \zeta < 0 \end{cases} \quad (3.9)$$

$$\phi_{te}(\zeta) = \begin{cases} 0 & \zeta \geq 0 \\ \frac{\kappa}{3} [4(-\zeta)^{4/3} (1 - \zeta)^{-1/3} + \phi_e] & \zeta < 0 \end{cases} \quad (3.10)$$

where $\phi_e = \overline{w'eu_*^3}$ is a dimensionless energy flux function proportional that involves the turbulent kinetic energy flux without the need for measurements at multiple heights. The dimensionless buoyancy flux function for (3.1) is of course, ζ for all conditions, and the dimensionless pressure work ϕ_{tp} is taken to be the residual of all other terms. Lastly, the dimensionless TKE dissipation rate function $\phi_\varepsilon(\zeta)$ is

$$\phi_\varepsilon(\zeta) = \begin{cases} \frac{1+(6-1)\zeta}{(1-\zeta)} & \zeta \geq 0 \\ \frac{(1-\zeta)}{(1-7\zeta)} - \zeta & \zeta < 0 \end{cases} \quad (3.11)$$

where the data to construct these functions is from marine surface layer experiments aboard the stationary R/P *FLIP* and R/V *Columbus Iselin* using similar instruments, data acquisition systems and processing algorithms. R/P *FLIP* was located offshore of Los Angeles, CA; R/V *Columbus Iselin* operated near the Gulf Stream off of Cape Hatteras, NC. Figure 3.14 shows the normalized TKE budget curves from Edson and Fairall (1998) and scatter of LASER (2016) data, both as a function of ζ for each of the terms in (3.1).

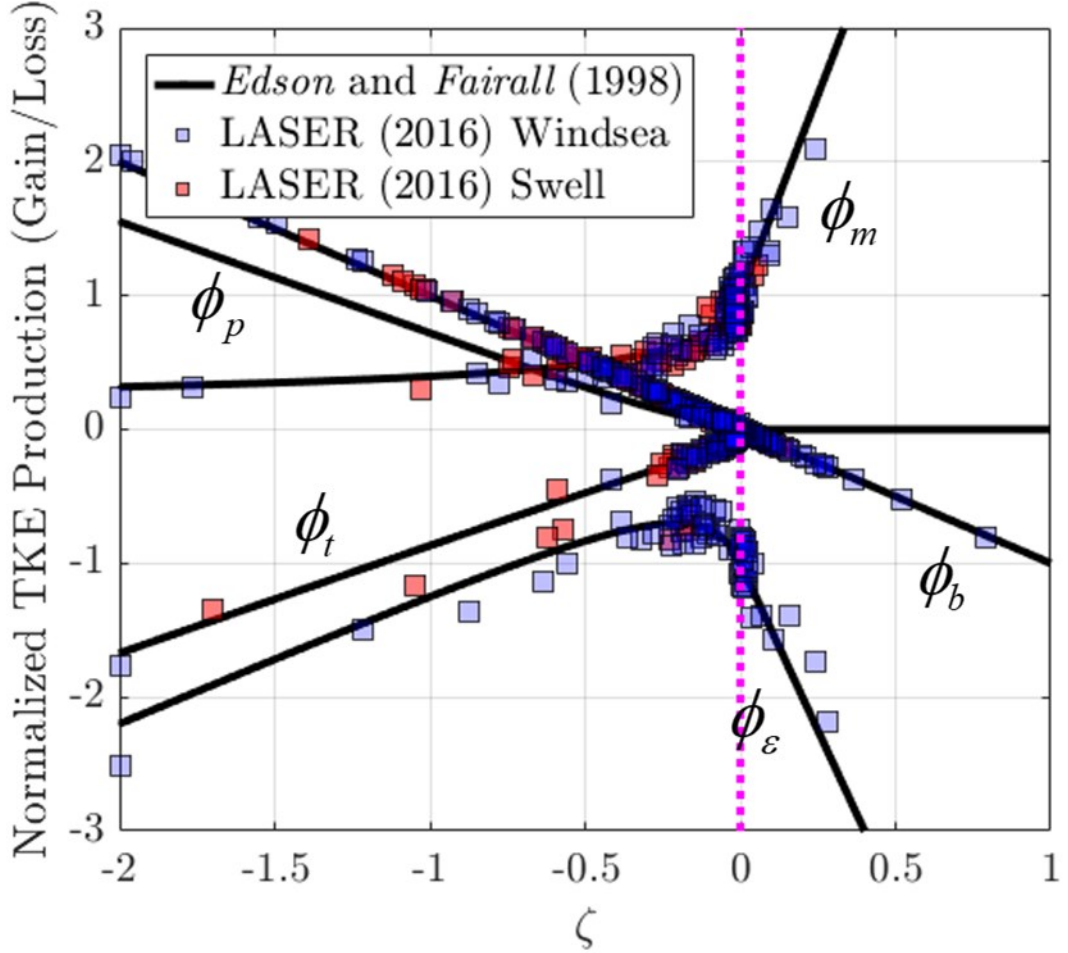


Figure 3.14 (a) Normalized TKE budget as a function of Monin-Obukhov stability, ζ . Curves from Edson and Fairall (1998) are in solid black. For the LASER data, values from windsea are given by blue circles and swell by red squares. Each TKE budget term is labeled. The magenta dotted line indicates $\zeta = 0$

Normalized TKE budget values color-coded by wave age reaffirm windsea observations were made in predominantly near-neutral and neutral stability over the stability range $-0.38 \leq \zeta \leq 0.09$; swell conditions were observed in most often low wind environments over the range $-1.12 \leq \zeta \leq -0.13$. Average normalized TKE shear production in the two wave conditions was $\bar{S}_{ws} = 1.164$ and $\bar{S}_s = 0.482$, respectively. Conversely, the average normalized TKE buoyancy production values were $\bar{B}_{ws} = 0.116$

and $\bar{B}_s = 0.824$. Shear production and buoyancy production are thus the dominant production terms in the observed windsea and swell wave conditions, respectively.

In the unstable ASL, upward vertical velocities can contribute substantially to the TKE flux divergence terms (turbulent transport, ϕ_t and pressure work ϕ_p). These two terms redistribute TKE and can lead to local loss and gain of TKE, respectively. The turbulent transport convects turbulence upward, while the pressure transport is thought to be associated with the downward transport of ‘inactive’ turbulence from the upper part of the boundary layer (Smedman, et al. 1994) in unstable and neutral conditions (Hogstrom et al. 2002), and due to upward momentum transfer from waves in stable conditions (Rutgersson, et al. 2001). In Figure 3.14, turbulent transport losses and pressure transport gains in TKE are largest in magnitude in the more unstable conditions (ζ more negative) where swell is observed. In stable conditions, turbulent transport and pressure work are considered to be negligible in the ASL as the vertical distribution of TKE is constrained by stratification and therefore redistribution of TKE via transport is not necessary to maintain closure of the budget. We conclude this chapter in the next section arriving finally at the parameterization of TKE dissipation rates using the product of Monin-Obukhov shear production and normalized dissipation rate $\bar{\varepsilon} \approx u_*^3 \kappa^{-1} z^{-1} \phi_\varepsilon$ from Ortiz-Suslow, et al. (2020).

3.5 Parameterization of TKE dissipation rate

TKE dissipation rate can be approximated where MOST is valid by rearranging the normalized TKE dissipation rate expression $\phi_\varepsilon = \varepsilon \kappa z u_*^{-3}$. By manipulating this expression to determine the TKE dissipation rate, the resulting values represent the scaling of the eddy momentum flux based on the stability of the ASL. In neutral and stable conditions,

$\bar{\varepsilon} \approx u_*^3 \kappa^{-1} z^{-1}$ (TKE gain via shear production minus TKE loss via dissipation approximately is zero), whereas in unstable conditions dissipation exceeds production (Sjöblom and Smedman, 2002). Figure 3.15 shows a linear regression fit of the observed dissipation rates as a function of the MOST parameterization $\bar{\varepsilon} \approx u_*^3 \kappa^{-1} z^{-1} \phi_\varepsilon$ and compares the timeseries evolution of the two dissipation rate values compared with the wave age.

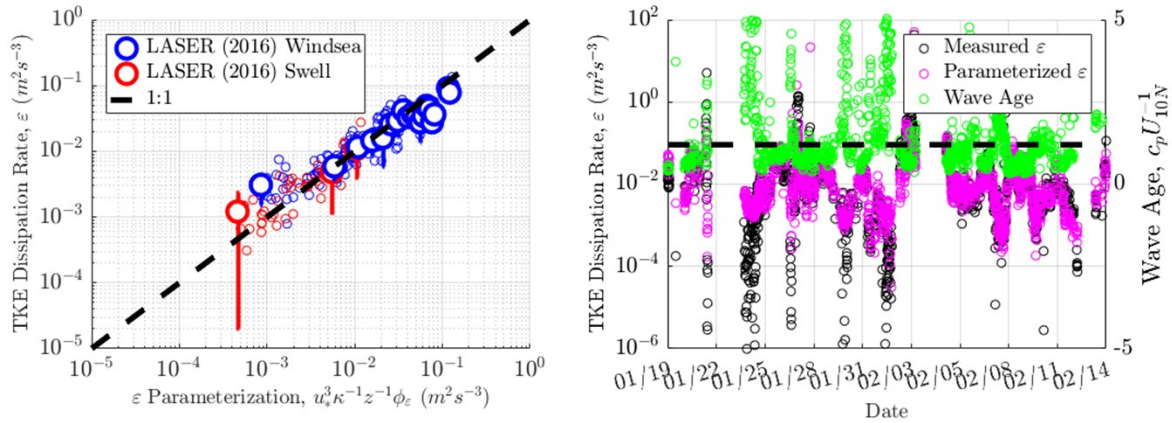


Figure 3.15 (a) TKE dissipation rate as a function of the MOST parameterization (Ortiz-Suslow, et al. 2020) in windsea (blue) and swell (red) conditions. The black-dashed line indicates 1:1. (b) TKE dissipation rate measurements (black), parameterized (magenta), and the corresponding wave age (lime green).

Using the MOST parameterization, the Pearson correlation coefficients of TKE dissipation rate values in windsea and swell were found to be $R^2 = 0.87$ and $R^2 = 0.76$, respectively. In panel (b), comparison between $\bar{\varepsilon}_{\text{meas}}$ and $\bar{\varepsilon}_{\text{param}}$ indicates at higher wave age that the parameterization often under-estimates the TKE dissipation rate. Median values of the ratio $\bar{\varepsilon}_{\text{meas}} \bar{\varepsilon}_{\text{param}}^{-1}$ were found to be 0.98 and 0.63 for windsea and swell conditions, respectively. Using the same parameterization and assuming near-neutral stability in the HBL measured by Zhang (2010), $\bar{\varepsilon}_{\text{meas}} \bar{\varepsilon}_{\text{param}}^{-1} \approx 1.12$ with a correlation coefficient $R^2 = 0.69$.

3.6 Summary

Motivated by discrepancies in theoretical and practical formulations for heat flux contributions to the ASL by the dissipation of TKE taken in the hurricane boundary layer (HBL) during CBLAST (Zhang, 2010), we computed the TKE, its' dissipation rate, and dissipative heating in the explicitly non-hurricane environment in an effort to parameterize dissipation rate and constrain dissipative heating to have a physical limit based on the production of turbulence itself rather than the cube of wind speed as had been originally put forth (e.g. Bister and Emanuel, 1998). We also compared dissipative heating to sensible heat fluxes, and determined that while this ratio is usually small, it may be as large as 0.258 where air-sea temperature disequilibrium and 10-meter equivalent wind speeds are smaller.

Dissipation rates were compared for windsea and swell conditions using the Pierson and Moskowitz (1964) criterion ($c_p U_{10N} > 1.2$) to discriminate them, such that windsea and swell constituted 68.6 percent and 29.4 percent of the field observations, respectively. Dissipation rates were found to be larger in windsea than swell, and deviate from unity with the Monin-Obukhov shear production of TKE as that quantity increases (which occurs with increasing surface stress $-\rho \bar{u}'w'$ and wind speed U_{10N}). Monin-Obukhov stability ζ allowed us to quantify the role of buoyancy production relative to shear production of TKE, and dissipation rates were determined to be largest for windsea in near-neutral (but still unstable) conditions.

Significant wave height and wave steepness were evaluated using the water surface elevation data collected aboard R/V *F.G. Walton Smith* and dissipation rates were compared with these wave parameters to determine their influence on TKE dissipation rates. Increased wave steepness and significant wave height were found to correlate with

larger dissipation rates, however wave height appears to influence dissipation rates in windsea more strongly, while wave steepness does so during swell conditions. This behavior was consistent with parameterization of the sea surface roughness in windsea versus swell conditions using wave-scaled Charnock roughness $z_o H_{sig}^{-1}$, wave age based roughness $u_* c_p^{-1}$, and steepness based roughness $H_{sig} L_p^{-1}$ following Drennan et al. (2005).

Using a set of universal functions of Monin-Obukhov stability coming from Edson and Fairall (1998), we constructed the TKE budget and compared its' terms based on stability measurements in windsea and swell conditions. From the normalized budget values in terms of net gain or loss of TKE, it was clear that a majority of the conditions were taken in unstable ASLs (88.4 percent). Since eddy fluxes of momentum and heat are critical to the production of turbulence by acting against mean shear and stratification in the ASL, we investigated the relationships of these fluxes to wave age and significant wave height. Not surprisingly, fluxes of both were largest at low wave age (windsea) and high significant wave height (more developed, steeper waves and/or higher winds). From a comparison of LASER (Smith, Zhang, and Haus, 2019) and CBLAST (Zhang, 2010) data, we can see that regardless of the wind speed or height of the observations the dissipation rate of TKE is to first-order approximated by the Monin-Obukhov shear production of TKE in each dataset and the two sets of values overlap (Figure 3.11). To that end, a parameterization was constructed using the first-guess balance of shear production and dissipation, to which buoyancy production of TKE was added via stability, taking the form,

$$\bar{\varepsilon} \approx u_*^3 \kappa^{-1} z^{-1} \phi_\varepsilon \quad (3.12)$$

Chapter 4: Laboratory Sub-Surface Turbulence and Dissipation Beneath Hurricane Wind and Wave Conditions

In this section, we present and analyze laboratory measurements of turbulence and bubble behavior beneath a wind-wave tank air-sea interface across a range of wind conditions up to hurricane-force and in two different wave conditions. The goal of the results from this section are to characterize the turbulence and bubble populations produced as a result of evolution of the water surface and the breaking of waves. Simultaneous surface and sub-surface measurements were made to accomplish this. Parameterization of bubble size distributions in terms of non-dimensional turbulence numbers, breaking likelihood, and water temperature (viscosity effects) extend prior literature to sub-surface behavior beneath hurricane-force wind conditions. Turbulent kinetic energy dissipation rates are scaled by wave height and provide insight into how the magnitude of sub-surface turbulence and dissipation vary as surface wave conditions change, roughen and break.

4.1 Surface wave statistics

4.1.1 Wave conditions in the experiments

We present first a summary of wave conditions during the 34 unique experiments, as described by the fundamental parameters of wave length L , wave period T , and wave height H , as well as derived parameters including significant wave height H_{sig} , phase speed $c_p = LT^{-1}$, and steepness $(H/2)k$. Figure 4.1a-b show the water surface elevation spectra colored by increasing wind speed for the two wave types in these experiments, while panels c-e show the changes in wave frequency, wavenumber, and wave steepness as a function of increasing wave height. Table 4.1 gives a summary of wave conditions for all experiments. The length of experiments was dictated by the saturation behavior of noble gases in the water of the SUSTAIN wind-wave tank.

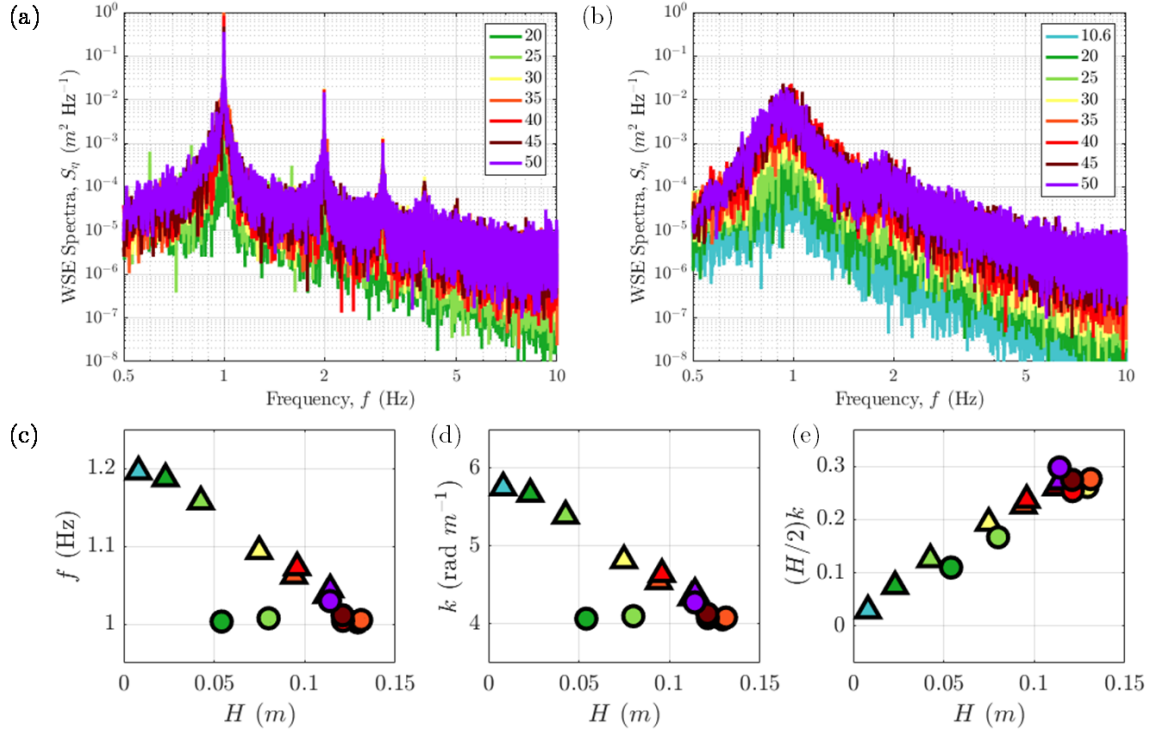


Figure 4.1 Wave spectra and statistics based on individual crest analysis from Babanin (2007). (a) Monochromatic water surface elevation spectra (b) JONSWAP water surface elevation spectrum (c) Median wave frequency (d) Median wavenumber (e) Median wave steepness. In panels (c)-(e), the triangles and circles indicate statistics from the JONSWAP spectrum and monochromatic wave conditions, respectively.

Experiment	T_w (°C)	U_{10}	WC	H_{sig} (m)	f (Hz)	k (rad m $^{-1}$)	(H/2) k
1	25.74	35	M	0.141	1.01	4.09	0.20
2	25.81	20	M	0.078	1.00	4.07	0.11
3	25.72	25	M	0.115	1.01	4.10	0.17
4	25.76	40	M	0.173	1.00	4.08	0.25
5	25.71	45	M	0.178	1.01	4.13	0.27
6	26.00	50	M	0.177	1.03	4.28	0.30
7	25.35	30	M	0.188	1.00	4.06	0.26
8	25.68	35	M	0.191	1.01	4.08	0.28
9	21.19	35	M	0.178	1.01	4.12	0.27
10	20.45	20	M	0.122	1.00	4.05	0.17
11	19.92	40	M	0.196	1.00	4.06	0.28
12	20.16	45	M	0.199	1.01	4.10	0/30
13	20.28	50	M	0.256	0.84	2.91	0.27
14	20.57	25	M	0.150	1.02	4.17	0.23
15	20.49	30	M	0.168	1.01	4.14	0.25
16	20.66	35	M	0.180	1.01	4.13	0.27
17	25.77	35	M	0.189	1.00	4.07	0.27
18	31.62	35	M	0.196	1.00	4.06	0.28
19	31.09	40	M	0.194	1.00	4.06	0.28
20	31.41	45	M	0.189	1.00	4.07	0.28
21	31.91	50	M	—	—	—	—
22	32.41	20	M	0.128	1.00	4.08	0.18
23	32.34	25	M	0.152	1.01	4.08	0.22
24	32.19	30	M	0.154	1.01	4.15	0.23
25	26.02	35	S	—	—	—	—
26	26.53	40	S	0.191	0.95	3.70	0.24
27	26.32	40	S	0.149	1.07	4.64	0.24
28	26.23	45	S	0.172	1.04	4.34	0.26
29	26.14	50	S	0.182	1.04	4.40	0.27
30	25.83	10.6	S	0.019	1.19	5.75	0.03
31	25.83	20	S	0.041	1.19	5.67	0.07
32	25.89	25	S	0.071	1.16	5.39	0.13
33	25.86	30	S	0.117	1.09	4.82	0.19
34	25.81	35	S	0.148	1.06	4.55	0.23

Table 4.1 Wave statistics summary table for the SUSTAIN experiments.

Wave statistics were determined using the individual wave crest analysis procedure described in Chapter 2.2.6. Experiments 1-24 and 35 were conducted with a monochromatic, or single-frequency mechanical paddle wave, whereas experiments 25-34 featured a JOint North Sea WAves Project (JONSWAP) spectrum scaled for the laboratory. Prescribed amplitude and frequency for the monochromatic waves were 0.15 meters and 1.0 Hz, respectively. For the spectrum waves, a significant wave height and peak period were used to define the spectrum. For experiment 25, these were 0.5 meters and 0.65

seconds, respectively. For experiment 26, the peak period was increased to 1 second. For experiments 27-34, values of 0.15 meters and 1 second were used, respectively.

Figure 4.1a-b presents water surface elevation spectra S_η from Experiments 1-8 and 27-34, respectively, chosen for comparison based on similar average water temperature (25.71 °C and 25.96 °C). From visual inspection, it is first clear that the monochromatic and JONSWAP spectrum wave spectral density do not respond to increasing momentum flux from wind at the same rate. Significant wave height, which includes the integral of the wave spectrum, increases by only 0.0033 meters per unit U_{10N} in the former whereas the rate is 0.0054 meters per unit U_{10N} in the latter (+ 63.6 percent). The dominant (peak) frequency of the spectra in the two wave conditions spanned the range 0.998–1.001 and 0.945–1.002 Hz, respectively.

Monochromatic wave energy density per unit area increases rapidly from $E_w(U_{10N} = 25) = 7.7 \text{ Jm}^{-2}$ to $E_w(U_{10N} = 30) = 20.6 \text{ Jm}^{-2}$ followed by a gradual decrease to $E_w(U_{10N} = 50) = 17.9 \text{ Jm}^{-2}$. In contrast, the energy density per unit area of the JONSWAP spectrum waves continually increases from $E_w(U_{10N} = 10.6) = 0.23 \text{ Jm}^{-2}$ to $E_w(U_{10N} = 50) = 19.4 \text{ Jm}^{-2}$, only matching the energy (within 10 percent error) in monochromatic wave cases after $U_{10N} \geq 45$ meters per second. That is, greater wind speed is required for the prescribed JONSWAP spectrum waves to equal the wave energy associated with the monochromatic waves. Additionally, regardless of the wave condition, paddle-generated waves in the SUSTAIN wind-wave tank result in bound harmonics that can be observed in the wave spectra. These harmonics produce larger spikes in the monochromatic wave spectra than the JONSWAP wave spectra due to the single versus

multiple frequency composition and steepness of the paddle wave fields (Plant, et al. 1999; Plant et al. 2004).

Based on individual wave crest analysis, Figure 4.1c-e above shows the differences in the wave conditions in terms of fundamental parameters of wave frequency, wavenumber, and wave steepness. Median wave frequency decreases with increasing wind speed from $f(U_{10N} = 20) = 1.187 \text{ Hz}$ to $f(U_{10N} = 50) = 1.044 \text{ Hz}$ in the JONSWAP spectrum wave conditions, whereas monochromatic wave frequency remains within 2.9 percent of the prescribed 1.000 Hz frequency regardless of wind speed. Despite this, the wave frequency does increase (1.002 to 1.029 Hz) with decreasing wave height (0.129 m to 0.114 m) for monochromatic wave conditions where $U_{10} \geq 30 \text{ ms}^{-1}$.

Median wavenumber $k = 2\pi L^{-1}$ follows identical behavior in the two wave conditions, wherein the length of individual waves increases (therefore k decreases) with increasing U_{10N} . Although we expect increased momentum flux at higher winds to result in steepening and shortening of individual monochromatic waves, the JONSWAP spectrum waves show a decrease in wave frequency towards the prescribed 1.00 Hz frequency and a decrease in wavenumber towards $k = 4.043 \text{ rad m}^{-1}$. Combined with significant wave height measurements, this behavior suggests that as wind speed increases, the wave tendency is a steepening and lengthening individual crests.

Combining the wave height and length, the wave steepness is shown in Figure 4.1e and shows that in both wave conditions, waves steepen between $U_{10N} = 20 - 50 \text{ ms}^{-1}$. Monochromatic waves have greater steepness for a given wind speed covering a range $\delta = (H/2)k = 0.109 - 0.298$, with an average rate of increase of $\partial \delta / \partial U_{10N}^{-1} = 0.0010$. JONSWAP spectrum waves were less steep ($\delta = (H/2)k = 0.075 - 0.272$), however, they

steepened at a more regular interval and greater average rate ($\partial \delta \delta U_{10N}^{-1} = 0.0065$) with increasing wind speed.

In summary, momentum flux from wind to waves is received by a single dominant frequency in monochromatic wave experiments, while it is distributed over the same fetch across different wave frequencies during the JONSWAP spectrum experiments. Consequently, relative to the JONSWAP spectrum waves, monochromatic waves are found to have 18.2 percent greater steepness and 69.5 percent greater wave energy density per unit area on average across the range of wind speeds tested. Although less steep, the JONSWAP spectrum waves are modeled after actual fetch-limited open ocean observations (Hasselmann, et al. 1973) with 86.2 percent greater frequency variance than the monochromatic waves, and they hence respond more gradually and consistently with increasing momentum flux.

4.1.2 Wave breaking

By analyzing individual wave crests as part of water surface elevation timeseries, we are able to assess the structural instability and breaking likelihood of waves in the different wind and wave conditions; this knowledge of wave breaking is crucial to connecting surface waves to the sub-surface turbulence and dissipation. By performing a continuous wavelet analysis, we were able to quantify the energy content of wave crests and distinguish breaking and non-breaking wave crests following Elsayed (2008) and Liberzon, et al. (2019). In this section, we present results of the technique comparing water surface elevations $\eta(t)$ from a monochromatic and JONSWAP spectrum experiment each (Experiments 8 and 34) where $U_{10N} = 35 \text{ ms}^{-1}$ and the average water temperature was 25.7°C and 25.8°C , respectively. Using the phase time method (PTM; Huang, et al. 1992,

Liberzon, et al. 2019), a phase function $\Phi(t) = \tan^{-1}(H(t) / \eta(t))$ was constructed in part by computing the Hilbert transform $H(t) = \pi^{-1}t^{-1} \cdot \eta(t)$ via a convolution operation on the water surface elevation. The phase function was unwrapped to eliminate jump discontinuities and de-trended, and its' time derivative is equal to the instantaneous frequency $F = \partial\Phi/\partial t^{-1}$. A 30-second segment of the $\eta(t)$ and $F(t)$ timeseries for experiments 8 and 34 are shown in Figure 4.2, panels (a) and (b), respectively.

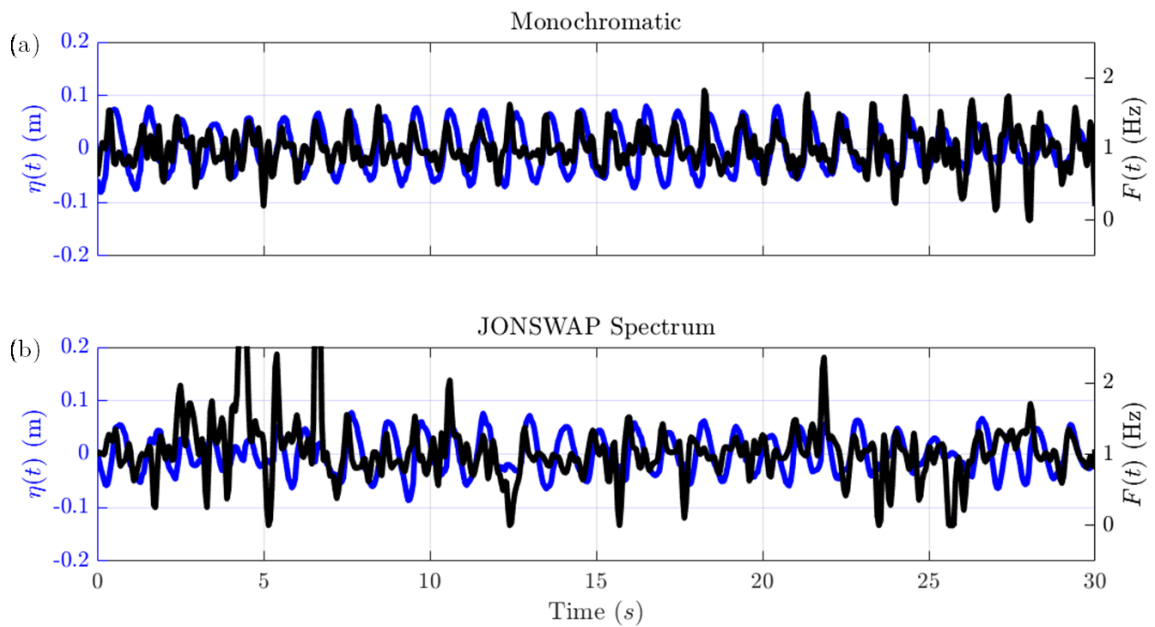


Figure 4.2 Water surface elevation timeseries segment $\eta(t)$ (blue) and instantaneous frequency $F(t)$ (black) for (a) Experiment 8 and (b) Experiment 34.

Average instantaneous frequency for the entire timeseries, a segment of which is displayed in Figure 4.2, are $\bar{F}_M = 1.04 \pm 0.38$ Hz and $\bar{F}_S = 1.07 \pm 0.45$, for Experiments 8 and 34, respectively. For the segments displayed in Figure 4.2, the averages are 1.002 Hz and 1.053 Hz in panels (a) and (b), respectively. Consistent, repeating spikes in $F_M(t)$ occur along with the wave crests approximately 1.00 seconds apart as expected given a

prescribed frequency of 1.00 Hz and their relative magnitudes are more similar than those depicted in panel (b) for $F_s(t)$. A continuous wavelet transform using the Morlet wavelet $\Psi(t) = \pi^{-1/4} e^{i\omega_0 t} e^{-t^2/2}$ (Elsayed, 2008) was performed on $F(t)$ to accurately detect breaking-related patterns and determine breaking statistics for wave crests in each experiment. The wavelet amplitude $\|W_m\|^2(f,t)$ for the same 30-second segments in Figure 4.2 are presented in Figure 4.3 below. Overlaid on top is the integral of the wavelet amplitude with respect to frequency, or the localized total energy, $E_{lw} = \int_f \|W_m\|^2(f,t) df$.

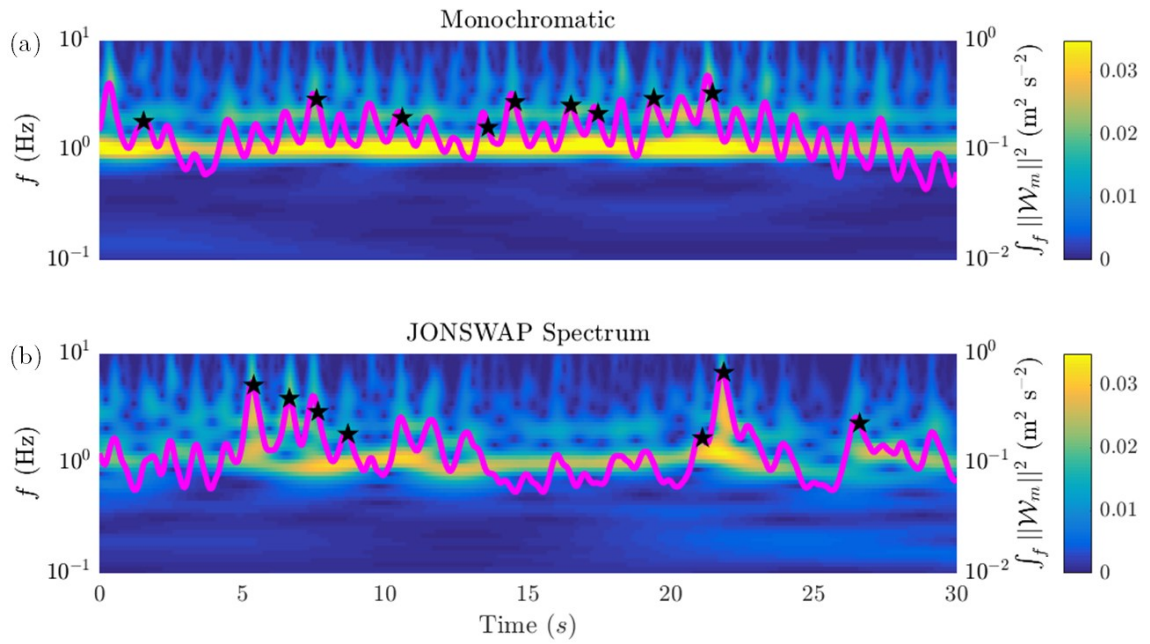


Figure 4.3 Wavelet amplitude segment for (a) Experiment 8 and (b) Experiment 34 as in Figure 4.2. Overlaid in magenta is the localized total energy. The black stars, where present, are the location of wave crests satisfying the wave crest downward acceleration breaking criterion $AF_l^2 \geq \beta_0 g$.

From Figure 4.3, we see the wavelet amplitudes include a dominant signal near the prescribed frequency for each wave type in addition to higher frequency tails at each wave crest. The largest magnitude areas of the wavelet amplitude are generally collocated with higher localized wave energy as well. As the Stokes limiting steepness criterion $HL^{-1} = 1/7 \approx 0.142$ is rarely observed in the field (Gemmrich, 2010), we instead characterized breaking following Liu (1993) and Elsayed (2008). Assuming the linear dispersion relationship, the wave surface critically destabilizes and breaks when the downward acceleration of a crest exceeds the fraction β_0 of the gravitational acceleration according to

$$AF_l^2 = \beta_0 g \quad (3.1)$$

where $A = 0.5H$ is the local wave amplitude, F_l is the local wave frequency, and β_0 is a limiting fraction of the gravitational acceleration. The value of β_0 has been assumed equal to 0.5 in classical studies (Kinsman, 1965), while it has been found to be nearer to 0.4 in laboratory studies (Hwang, et al. 1989) or even less than that (Holthuijsen and Herbers, 1986). Following Liu (1993) and Hwang et al. (1989), we prescribe $\beta_0 = 0.4$. For each localized frequency spectrum $\Psi_i(f) = [W_m(f,t)]_{t=t_i}$ (at each wave crest), the peak of that spectrum is identified and a separation frequency (between low and high frequency contributions to the breaking) α and a high frequency cutoff equal to $0.25 f_{Nyq} = 5.0$ Hz is declared. Similar to Liu (1993) Equation 1 and Elsayed (2008) Equation 6, F_l is defined

$$F_l = \left[\frac{\int_{f_p}^{f_n} f^2 \Psi_i(f) df}{\int_{f_p}^{f_n} \Psi_i(f) df} \right] \quad (3.2)$$

where (4.2) is an average frequency over the high frequency range $\alpha f_p - f_n$ of the localized frequency spectrum. Consistent with Liu (1993), we use $\alpha = 1.35$ denoting the multiple of the peak frequency at which the high frequency range of the spectrum begins. Analysis results of the percentage of breaking crests and the localized wave energy at those crests are both shown as a function of the wind stress (or momentum flux) in Figure 4.4.

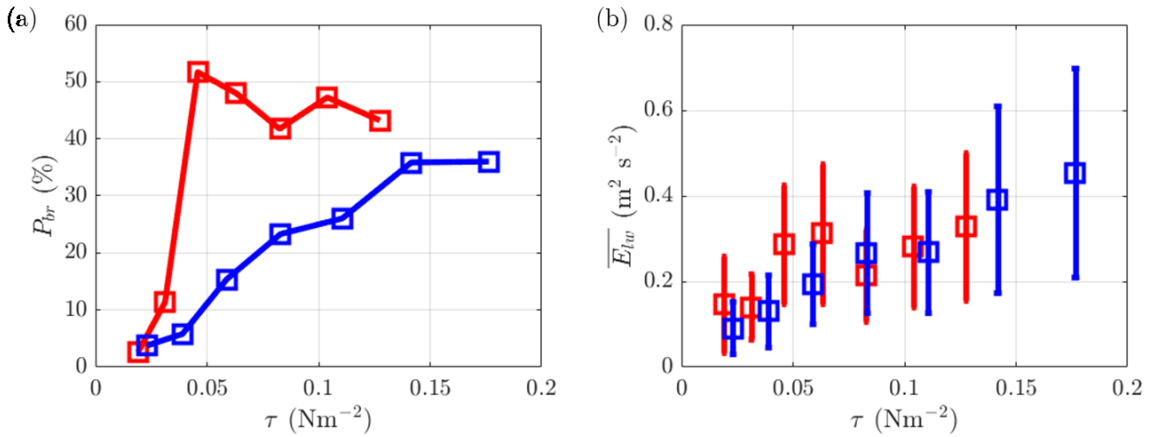


Figure 4.4 (a) Percentage of wave crests satisfying the aforementioned breaking criteria for Runs 1-8 (red) and Runs 27-34 (blue) and (b) Localized wave energy at breaking wave crests in the same experiments and colors, respectively. Error bars denote one standard deviation, and the marker indicates the mean. In both panels, the x-axis is wind stress.

In a manner similar to that of the significant wave height, in Figure 4.4 (a), we see that the percentage of wave crests that break abruptly increases above $U_{10N} = 30 \text{ ms}^{-1}$ in monochromatic wave conditions, after which a decreasing trend is observed. Conversely, the percentage of breaking waves has an increasing trend with wind stress and takes the shape of a logistic sigmoid. Such behavior is common in models of population growth or capacity-limited dynamics, that is, featuring an approximately exponential growth period, followed by a linear growth period, and a saturation or asymptotic behavior (P.F. Verhulst, 1838). Linear regression of H_{sig} and P_b confirms a significant positive trend in both monochromatic ($R^2 = 0.97, p_{0.05} = 0.0000279$) and JONSWAP spectrum (

$R^2 = 0.94, p_{0.05} = 0.00017$) wave conditions. At and above $U_{10N} = 30 \text{ ms}^{-1}$, regression of P_b with τ is statistically significant at the 95% confidence interval in JONSWAP spectrum wave conditions ($R^2 = 0.89, p_{0.05} = 0.01$), but not monochromatic wave conditions ($R^2 = 0.79, p_{0.05} = 0.07$). From panel (a), we observe that the percentage of breaking waves in monochromatic conditions always exceeds that of waves from the JONSWAP spectrum for $U_{10N} > 25 \text{ ms}^{-1}$ ($\tau \geq 0.04 \text{ Nm}^{-2}$), and that the greatest increase in the percentage of breaking for either condition is for $U_{10N} = 25 - 35 \text{ ms}^{-1}$ ($\tau \approx 0.04 - 0.08 \text{ Nm}^{-2}$) including the transition from tropical storm to hurricane force winds (33 ms^{-1}). Therefore, we surmise the percentage of breaking waves that occur in our fetch limited laboratory domain is directly related to momentum flux across the frequency spread of waves and wave-wave interactions. We believe these two factors influence the height, steepness, and downward acceleration of the wave crests, resulting in greater breaking percentages for single-wave conditions subject to the full magnitude of the wind stress.

In Figure 4.4 (b), the local wave energy for breaking wave crests is plotted in terms of the wind stress. Linear regression of the two data series resulted in the fit $\bar{E}_{lw,M} \approx 1.73\tau + 0.10$ for the monochromatic data and $\bar{E}_{lw,S} = 2.38\tau + 0.04$ for the JONSWAP spectrum data. The fits had Pearson correlation coefficients of $R^2 = 0.88$ and $R^2 = 0.96$, respectively. Hence, in the JONSWAP spectrum conditions, the local wave energy (or frequency-integrated wavelet amplitude squared) of breaking wave crests is approximately equal to the momentum flux from the wind to waves. For completeness, a summary of the breaking wave statistics for all experiments is given in Table 4.2.

Experiment	T_w (°C)	U_{10}	WC	P_b (%)	E_{lw} ($m^2 s^{-2}$)
1	25.74	35	M	42.23	0.076
2	25.81	20	M	2.62	0.147
3	25.72	25	M	11.35	0.141
4	25.76	40	M	41.74	0.214
5	25.71	45	M	47.25	0.282
6	26.00	50	M	43.23	0.329
7	25.35	30	M	51.70	0.288
8	25.68	35	M	48.00	0.313
9	21.19	35	M	42.70	0.288
10	20.45	20	M	8.83	0.254
11	19.92	40	M	50.53	0.357
12	20.16	45	M	52.08	0.371
13	20.28	50	M	40.60	0.572
14	20.57	25	M	25.60	0.283
15	20.49	30	M	35.31	0.296
16	20.66	35	M	43.90	0.321
17	25.77	35	M	47.93	0.297
18	31.62	35	M	52.50	0.331
19	31.09	40	M	48.52	0.304
20	31.41	45	M	48.36	0.349
21	31.91	50	M	—	—
22	32.41	20	M	11.90	0.322
23	32.34	25	M	24.01	0.323
24	32.19	30	M	27.55	0.260
25	26.02	35	S	—	—
26	26.53	40	S	27.06	0.410
27	26.32	40	S	26.05	0.269
28	26.23	45	S	35.85	0.393
29	26.14	50	S	36.02	0.454
30	25.83	10.6	S	2.35	0.043
31	25.83	20	S	3.76	0.091
32	25.89	25	S	5.79	0.131
33	25.86	30	S	15.42	0.195
34	25.81	35	S	23.30	0.267

Table 4.2 Breaking statistics summary table for the SUSTAIN experiments.

4.2 Bubble size distributions

Having described wave conditions and breaking statistics for the various experiments, in this section we quantify the statistics, that is, size distributions of bubbles produced as a result of multi-scale wave breaking and subsequent air entrainment. We first present prior field and laboratory data, then compare distributions with the present study, after which we give a parameterization for bubble size distributions in terms of physical variables describing the wind, wave, and ambient water conditions.

4.2.1 Field versus laboratory data

Bubble size distributions have been estimated or quantified by visual, camera-aided optical, and acoustic methods since the mid-20th century, and so here we compare with 10 field, laboratory, and numerical model experiments described in prior literature. Each bubble size distribution comes from a unique set of circumstances including the wind speeds, wave conditions, where the field site was, water temperature, and so forth. First, we summarize the experimental conditions compared to our own study, in Table 4.3.

Publication/Study	Type	Wind (ms ⁻¹)	Waves	Environment	Bubble Sizes (μm)
<i>Blanchard and Woodcock (1957)</i>	F	Onshore, coastal	Breaking, shallow water	$T_w \approx 21^\circ\text{C}$	80-100
<i>Medwin (1970)</i>	F	-	$H \approx 0.5\text{m}$ (WMO 1-2)*	$T_w \approx 17 \pm 0.1^\circ\text{C}$	20-125
<i>Medwin (1977)</i>	F	3.3-6.1	$H \approx 0.6-2.0\text{m}$	-	25-250
<i>Johnson and Cooke (1979)</i>	F	8.0-13.0	$H \approx 2.0\text{m}; T \approx 3-4\text{s}$	$T_w \approx 3^\circ\text{C}$	75-200
<i>Thorpe (1984)</i>	N	-	-	-	30-180
<i>Deane (1997)</i>	F	3.0-5.0	$H \approx 0.9\text{m}; T \approx 7\text{s}$	$T_w \approx 18^\circ\text{C}$	50-1000**
<i>Deane and Stokes (1999)</i>	F	3.0-5.0	$H \approx 0.9\text{m}; T \approx 7\text{s}$	$T_w \approx 18^\circ\text{C}$	200-1100
<i>Deane and Stokes (2002)</i>	L	None	$H \approx 0.1\text{m}; PB MWP$ $WPF \approx 0.73 \pm 1\text{ Hz}$	-	100-1000**
<i>Callaghan, Stokes, and Deane (2014)</i>	L	None	PB sheet-like jets	$T_w \approx 5-30^\circ\text{C}$	40-500
<i>Deane, Stokes, and Callaghan (2016)</i>	L	None	MWP SB, PB $H \approx 0.2-0.8\text{m}$ $H \approx 0.15\text{m}, T \approx 1.0\text{s}$ (mono)	Natural pumped seawater	200-4000
Present study	L	10.6-50	$H \approx 0.15-0.5\text{m}, T \approx 0.65-1\text{s}$ (spectrum)	$T_w \approx 19.9-32.4^\circ\text{C}$ Natural pumped seawater	30-1500

Table 4.2 Brief summary of field and laboratory studies involving the measurement of bubble size distributions. Units are given in the table. Here, *F* denotes field studies, *L* denotes laboratory studies, and *N* refers to numerical model studies. WMO 1-2 refers to Sea States 1-2 as used by the World Meteorological Organization. Double asterisks indicate the number represents the majority of observed bubble sizes (usually 90% or greater).

From Table 4.3, the majority of older studies are field experiments in coastal locations, offshore of beaches, from research vessels or platforms; more recent work has been conducted in laboratory settings. More recent studies have expanded the upper range of bubble radii observed, likely as a result of additional fetch and the contained nature of a laboratory tank environment. Our study includes the highest range of wind speeds and the only to attain hurricane-force intensity, two distinct types of waves (the use of mechanical paddles is not unique to our study), and natural seawater as in Deane, Stokes, and Callaghan

(2016). We also observed a wide range of radii in the bubbles seen, taking advantage of a sub-surface optical system and bubble counting methodology (Atherton and Kerbyson, 1999) used in Deane and Stokes (1999) and Riquelme et al. (2013).

In Riquelme et al. (2013), the authors fit observed bubble size distributions to the lognormal distribution based on success in this approach from prior studies (Chen et al. 1998; Grau et al. 2005; Majumder et al., 2006). Maximum likelihood estimation (MLE; Dempster, et al. 1977) was then used to identify the most likely mean and variance for the lognormal distribution fits of each bubble size distribution. The example fit of a histogram of bubble sizes and the estimated lognormal PDF from Riquelme et al. (2013) is shown in Figure 4.5 (their Figure 5).

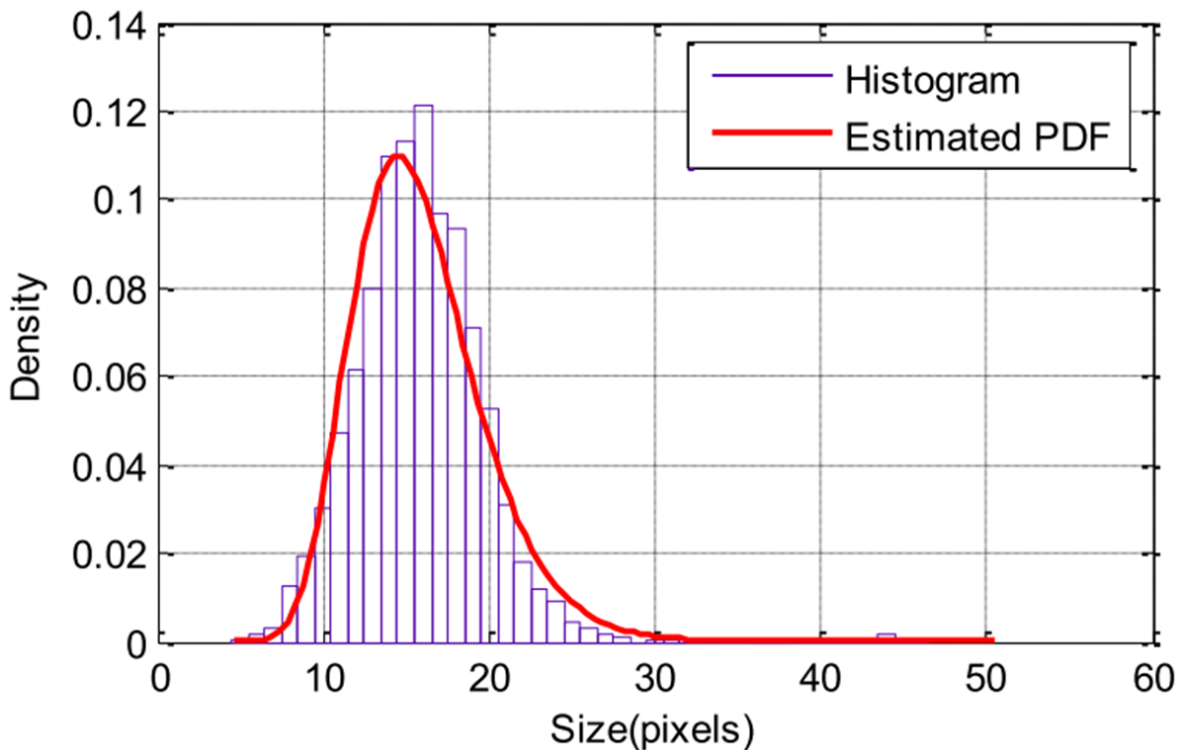


Figure 4.5 Histogram of a bubble size distribution (blue border bars) in terms of bubble size in pixels contrasted with the lognormal distribution (red). Figure and caption adapted from Riquelme et al. (2013).

The lognormal distribution is a prudent choice for bubble size distributions considering the values are always positive in x (radius or size) and are negatively skewed (smaller bubbles more common than large). In Figure 4.5, the bubble size distribution and lognormal fit have $R^2 = 0.97$ and root mean square error (RMSE) of 0.009. Following this strategy, each of the bubble size distributions reported in the prior studies outlined in Table 4.2 was normalized in radius and bubble density and parameterized using a lognormal distribution of the form

$$f(x) = a \exp\left[-(\ln[x - \mu])^2 / (2\sigma^2)\right] \quad (3.3)$$

where a is the peak of the bubble size distribution, x are the corresponding bubble radii for each observation, and μ and σ are the mean and standard deviation of the logarithm of the bubble size distribution, respectively. The mean gives a statistical indication of prevalent size, and the standard deviation indicates the relative diversity or variety of bubble sizes. A comparison of the normalized bubble size distributions and their lognormal fits is shown in Figure 4.6.

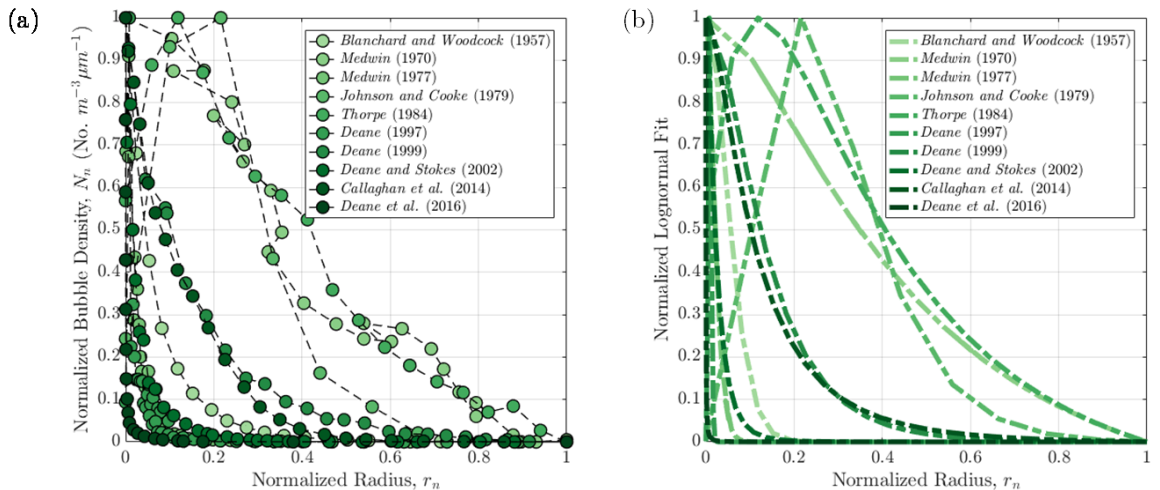


Figure 4.6 (a) Normalized bubble size distributions from prior field, laboratory, and numerical model studies listed in Table 4.3. (b) Normalized lognormal fits corresponding to each distribution given in panel (a).

Lognormal distributions in Figure 4.6 have Pearson correlation coefficients covering the range $R^2 = 0.85 - 0.99$ ($\bar{R}^2 = 0.96 \pm 0.05$) relative to the bubble size distributions they represent. The lowest two R^2 values were found with the data from Johnson and Cooke (1979) and Deane (1997), where the correlation coefficients were 0.85 and 0.88, respectively. In these cases, a poorly defined low radius peak to the distribution and scatter in a moderate radius range of the distribution were responsible for reduced agreement, respectively.

4.2.2 Monochromatic versus spectrum wave conditions

In the present study, bubble size distributions were constructed from a series of 10 shadowgraph images of bubbles taken beneath the water surface in each experiment. We focus here on the bubble density per radius observed beneath monochromatic ($a = 0.15\text{ m}$, $f = 1.00\text{ Hz}$) and JONSWAP spectrum ($H_{sig} = 0.15\text{ m}$, $T_p = 1.00\text{ s}$) waves subject to 10-meter equivalent wind speeds $U_{10N} = 20 - 50\text{ ms}^{-1}$. Specifically, we refer to Experiments 1-8 and 27-34, respectively. Average water temperature was 25.72°C and 26.01°C in the two series, with average percent error of 1.08 and 0.71 percent relative to the prescribed water temperature of 26.00°C , respectively. Bubble size distributions include radii spanning $30\text{-}1500\text{ }\mu\text{m}$ (1-50 pixels radius), and omit bubble density values less than one bubble per volume per radius micron. The probability distribution $P(r)$ of bubbles from the combined bubble populations in the 10 images are shown along with the lognormal distribution fits in Figure 4.7.

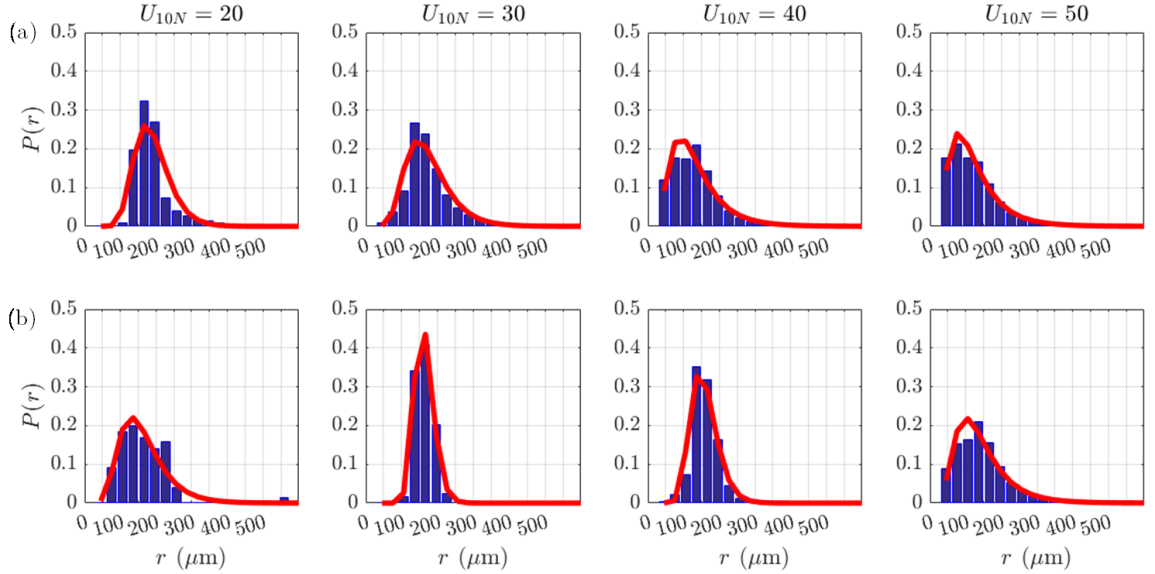


Figure 4.7 Probability distributions $P(r)$ for bubble size distributions (blue) and the lognormal distribution fit obtained using the maximum likelihood method (MLM, red) for (a) monochromatic wave conditions from Runs 2,7,4, and 6 from left to right (b) JONSWAP spectrum wave conditions from Runs 31,33,27, and 29 from left to right. Bubble radius is binned into 49 bins $dr = 30.25 \mu\text{m}$ equal to 1 square pixel from the images.

Probability distributions in Figure 4.7 were constructed by normalizing binned histograms of the bubble radius r from the analysis of each set of shadowgraph images via the aforementioned Circular Hough Transform (CHT; Atherton and Kerbyson, 1999). The lognormal distribution fit (plotted in red in Figure 4.7) follows the form of Equation 4.3 except that the peak value (height of the tallest bar) is the ‘most probable bubble’ radius. Pearson correlation coefficients between the distribution and the fits were $R^2 = 0.966$, $R^2 = 0.977$, $R^2 = 0.972$, and $R^2 = 0.987$, from left to right respectively for the monochromatic series (Figure 4.7a). Similarly, the R^2 values for the JONSWAP spectrum series were 0.954, 0.996, 0.989, 0.972.

From Figure 4.7, we see that for $U_{10N} \geq 30 \text{ ms}^{-1}$, regardless of the wave condition, the peak radius and mean of the distribution μ decreases (average bubble radius smaller) and the variance of the distributions (proportional to σ) increases as the wind speed

increases. Average wave breaking probability P_b for JONSWAP conditions less than $U_{10N} < 30 \text{ ms}^{-1}$ was 4.77 percent (versus 7.56 percent for monochromatic conditions) under 3.25 percent lower average wind stress magnitude. Considering this, we surmise that as the probability and intensity of wave breaking increases, turbulent shear forces break apart bubbles into those of smaller radius and/or the more forceful breaking events increase the penetration depth, and therefore pressure forces acting on the exterior of the bubble surfaces. Furthermore, only in JONSWAP spectrum cases does the distribution mean μ increase at low wind speeds, indicating the increasing presence of larger bubbles. Differences in the bubble distribution response with wave conditions are likely due to a combination of insufficient breaking frequency or magnitude, and the fact that momentum flux from wind contributing to the growth and steepness of any high frequency short waves riding the longer paddle waves is distributed across multiple wave frequencies that comprise the spectrum rather than transferred to waves of a single frequency as in the monochromatic wave conditions.

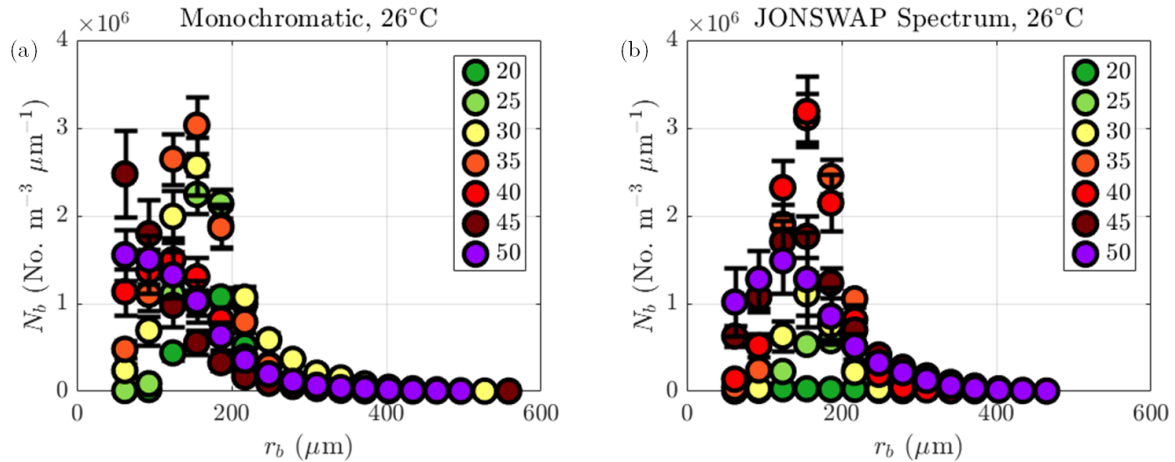


Figure 4.8 Bubble size distributions for (a) monochromatic (Experiments 1-8) and (b) JONSWAP spectrum waves (Experiments 27-34), color-coded by U_{10N} . Colored circles indicate the bin average, and error bars show 1 standard deviation.

Bubble size distributions have been commonly reported not in terms of probability distributions, but as a bubble density or number of bubbles per volume per radius micron $N_b = \text{No. m}^{-3} \mu\text{m}^{-3}$ (see prior studies listed in Figure 4.6). In Figure 4.8, an average of bubble size distributions by radius bin in micron are shown for the monochromatic and JONSWAP spectrum experiments with water temperature approximately 26°C (Experiments 1-8 and 27-34, respectively). Each average per radius bin is composed of the data from the 10 shadowgraph images mentioned earlier. Each bubble size distribution is also scaled to reflect the bubble density that would be observed for a volume of $V = 1 \text{ m}^3$ (in SUSTAIN observed volume was approximately $0.068 \times 0.052 \times 0.1 = 3.52 \times 10^{-4} \text{ m}^3$).

In Figure 4.8, both sets of average distributions show an increase in bubble density from $U_{10N} = 20 - 35 \text{ ms}^{-1}$, followed by a decrease in bubble density and decrease in the radius at which the greatest number of bubbles are seen at the highest wind speeds. The distribution means decrease according to the linear approximation $\mu_M \approx -3.5U_{10N} + 260$ and $\mu_S \approx -1.8U_{10N} + 220$ in monochromatic and JONSWAP spectrum conditions, respectively. Hence, average bubble size decreases 94.4 percent more rapidly with monochromatic waves given the same wind speed range as compared with the JONSWAP spectrum conditions. Additionally, in terms of the variation of bubble sizes observed, linear fits for the two series are $\sigma_M \approx 0.019U_{10N} + 0.8$ and $\sigma_S \approx 0.024U_{10N} + 0.4$, respectively.

Wind speed, wave state, and ambient water conditions are each important parameters when evaluating air-sea gas transfer and the production of bubbles at and beneath the sea surface (Brumer et al. 2017). In addition to the bubble size distribution itself, with statistics of the bubbles known (e.g. radius, volume, surface area, etc.), we can

express bubble populations in terms of physical parameters (wind, waves, water viscosity). Whitecap fraction, a proxy for wave breaking and indicative of bubble production, was parameterized by Brumer et al. (2017) using the wind-wave Reynolds number,

$$\text{Re}_{Hw} = u_* H_{sig} \nu_w^{-1} \quad (3.4)$$

a non-dimensional turbulence number comparing accelerations associated with the roughness and height of waves with the resistance of the water volume to penetration (e.g. by breaking waves) due to density and surface tension. In (4.4), u_* is the friction velocity, H_{sig} is the significant wave height, and ν_w is the water viscosity.

Significant wave height used in (4.4) was calculated in the typical manner described in Brumer et al. (2017) using the omnidirectional wave spectrum determined from the water surface elevation timeseries $\eta(t)$ such that $H_{sig} = 4 \times \sqrt{\int S_\eta(f) df}$. Although Reynolds numbers such as (4.4) were originally defined for windsea conditions, other studies have computed them with wave statistics from the full spectrum (Norris et al. 2012; Goddijn-Murphy et al. 2011), as we do here. Since the initial bubble size distribution is created as a consequence of wave breaking (generating turbulence), we take (4.4) and relate surface roughness and wave conditions in each experiment to the total integrated bubble volume (indicative of air entrainment), number of bubbles, and radius of bubbles observed in Figure 4.9.

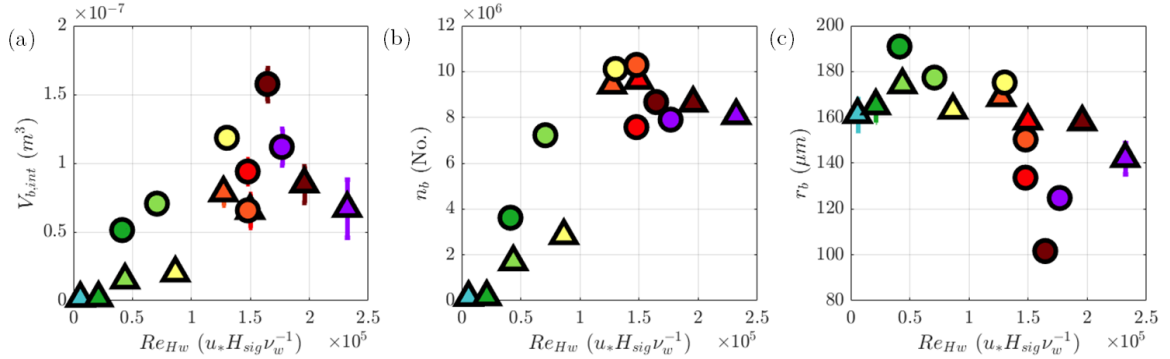


Figure 4.9 Bubble statistics as a function of wind-wave Reynolds number Re_{Hw} . (a) Total integrated bubble volume (b) number of observed bubbles and (c) bubble radius.

The total integrated bubble volume shown in Figure 4.9a increases with wind-wave Reynolds number for both wave conditions, with larger variance at higher wind speeds and a noted decrease in bubble volume at $U_{10N} = 50 \text{ ms}^{-1}$. Bubble volume data indicates air entrainment increased with wind stress but also responded to decreasing significant wave heights at higher winds that was seen in the monochromatic wave conditions (see Table 4.1). Separating the wave conditions and comparing the behavior however, we find substantial differences in the statistical correlation of wind-wave Reynolds number and total integrated bubble volume. Combined, the total integrated bubble volume increases linearly with Re_{Hw} with $R^2 = 0.49$ and root-mean square error (RMSE) 3.24×10^{-8} , however correlation coefficient increases to $R^2 = 0.65$ with RMSE of 2.22×10^{-8} when only considering the JONSWAP spectrum wave cases.

A similar disparity is seen when considering how the total integrated bubble volume changes with the percentage of breaking waves observed P_b . When doing so, the total integrated bubble volume increases linearly as a function of P_b with $R^2 = 0.68$ and $R^2 = 0.79$ when considering the monochromatic and JONSWAP spectrum wave conditions, respectively. The number and size of bubbles exhibit generally opposite

behaviors with increasing Re_{Hw} . Bubble number increases first over a range $\text{Re}_{Hw} = 5.8 \times 10^3 - 1.5 \times 10^5$, and then decreases in high wind conditions (Figure 4.9b). More (less) bubbles are seen in monochromatic wave cases at low (high) Re_{Hw} , and vice versa for the JONSWAP spectrum wave cases.

Bubble radius exhibits a similar dichotomy, with monochromatic (JONSWAP spectrum) waves resulting in larger (smaller) bubbles at low Re_{Hw} and the opposite trend for high Re_{Hw} (Figure 4.9c). The shift in behavior of both number and size of bubbles occurs in both wave conditions near $\text{Re}_{Hw} = 1.5 \times 10^4$, which occurs for both wave cases between $U_{10N} = 30 - 35 \text{ ms}^{-1}$. Consequently, although the total entrained volume of air increases with greater wind-wave turbulence number, there exists a critical region in Re_{Hw} near the transition between tropical storm and hurricane force wind speeds where bubbles shift from increasing in number and size to decreasing in number and size. In Figure 4.10, we show a series of colorized shadowgraph images with increasing Re_{Hw} for both wave conditions to highlight the differences the camera captured in the size and distribution of the bubbles in the images.

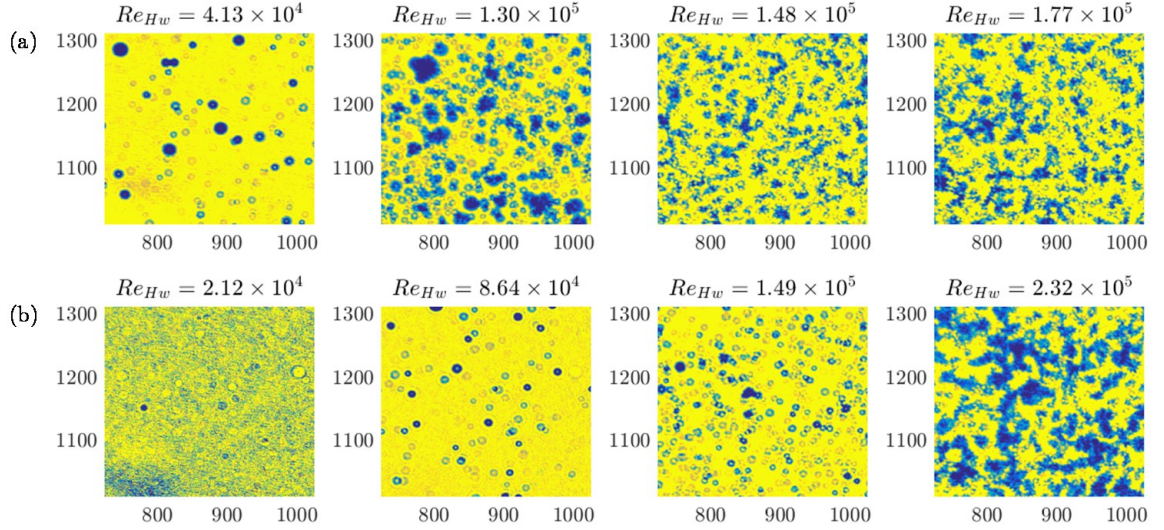


Figure 4.10 Colorized bubble shadowgraph images from (a) monochromatic experiments 2,7,4, and 6 from left to right and from (b) JONSWAP spectrum experiments 31,33,27, and 29, respectively. All images have the same color axis from 0 to 255, where darker/coolier values are closer to black and yellow/warm values are closer to white in the original images. Each image's dimensions are in pixels.

Each column in Figure 4.10 corresponds from left to right with increasing U_{10N} of 20, 30, 40, and 50 ms^{-1} , respectively. In both wave conditions, bubbles are at first spaced apart in the images and some larger bubbles which are the minority can be clearly seen. As the wind speed and Re_{Hw} increase, the smaller bubbles become more numerous, and groups of bubbles are seen clumping together. By the time the maximum wind speed is reached in either wave condition, the bubble image field is composed of groups of bubbles together and irregular fragments of dark and light area are seen in the images. By this point, bubbles are interacting with each other below the water surface and the images are saturated with bubble clusters. This behavior of the bubbles as seen in the images in Figure 4.10 may be responsible for shift in trend in bubble volume, number, and size of bubbles from low Re_{Hw} to high Re_{Hw} .

Now, in Figure 4.9, Re_{H_w} includes the effects of roughness from wind stress, wave height, and water viscosity – but which term is most responsible for the behavior seen with the total integrated bubble volume, number and radius of bubbles? In an effort to answer this, we computed correlation coefficients and associated p -values at the 95% confidence level between each term in the wind-wave Reynolds number and each observed bubble statistic for each wave condition. In monochromatic wave conditions, total integrated bubble volume was most strongly correlated with H_{sig} ($R^2 = 0.94, p = 0.0029$) while weaker correlations were seen with u_* ($R^2 = 0.69, p = 0.024$) and ν_w ($R^2 = 0.26, p = 0.163$). Bubble number was most strongly correlated with H_{sig} ($R^2 = 0.91, p = 0.0047$) with smaller correlations were seen in u_* ($R^2 = 0.45, p = 0.040$) and ν_w ($R^2 = 0.13, p = 0.191$). Lastly, the bubble radius was most strongly correlated with u_* ($R^2 = -0.93, p = 0.0021$). Significant wave height and water viscosity had lesser agreement, with $R^2 = -0.64, p = 0.05$ and $R^2 = 0.28, p = 0.229$, respectively.

For the JONSWAP spectrum wave conditions, the same terms have the highest correlation coefficients – significant wave height with total integrated bubble volume and number of bubbles, and friction velocity with bubble radius. The correlation coefficients and p -values were $R^2 = 0.87, p = 0.0039$, $R^2 = 0.85, p = 0.0049$, and $R^2 = -0.91, p = 0.024$, respectively. Water viscosity ν_w had correlations of $R^2 = -0.46$, $R^2 = -0.55$, and $R^2 = 0.61$ with total integrated bubble volume, number of bubbles, and size of bubbles, respectively.

Given these results, we posit that larger significant wave heights result in a greater initial volume of air being entrained and/or a greater initial downward acceleration of

newly created bubbles into the viewing area of our camera. The wind stress present above the surface and subsequent intensity and frequency of breaking events result in the breakup of the initial volume into smaller bubbles on average. Similar to Figure 4.9, we conclude this subsection by relating the percent of breaking wave crests P_b directly to the bubble statistics in Figure 4.11.

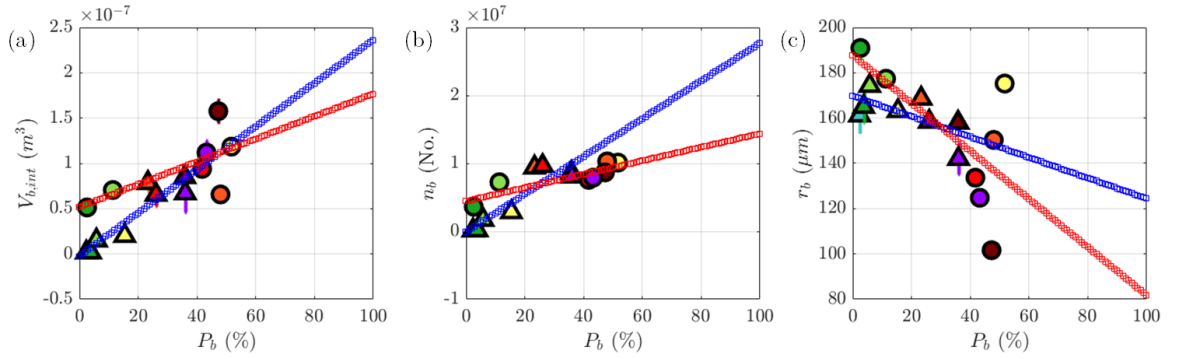


Figure 4.11 Bubble statistics as a function of the percentage of breaking wave crests P_b . (a) Total integrated bubble volume (b) number of observed bubbles and (c) bubble radius. Linear polynomial fits are overlaid in each panel for monochromatic (red) and JONSWAP spectrum (blue) wave conditions. As in Figure 4.9, circles and triangles indicate monochromatic wave and JONSWAP wave spectrum data, respectively.

From Figure 4.11, we can see that the behavior of the bubble statistics is similar to that shown in Figure 4.9, with larger integrated bubble volume, more bubbles, and smaller bubbles being observed where the percentage of breaking wave crests is larger. However, here we have overlaid linear polynomial fits to the data to illustrate how the rate of change of bubble statistics is different in the two wave conditions. Notably, the rate of increase in the number and total volume of bubbles is larger in JONSWAP spectrum wave conditions (slopes are 47.6 and 64.3 percent steeper than monochromatic wave data fit, respectively), but bubble radius does not decrease as rapidly with greater wave breaking prevalence.

Conversely, the bubble radius decreases quite rapidly in monochromatic wave conditions (134.1 percent steeper slope than JONSWAP spectrum wave conditions). That

is, increased wave breaking prevalence results in more air entrainment and more bubbles beneath JONSWAP spectrum waves but they are not as small; conversely, although monochromatic waves break more frequently, reduction in average radius is the dominant effect. Therefore, greater wave-breaking induced turbulence and breakup of bubbles is likely beneath monochromatic wave conditions whereas more bubbles are likely to persist in the field of view in JONSWAP spectrum wave conditions. In the next subsection, we develop a parameterization for bubble size distributions that takes into account the effects of wind, waves, and water temperature.

4.2.3 Bubble size distribution parameterization

To generalize the linkage between the dynamic air-sea interface and sub-surface bubbles, we parameterized observed bubble size distributions using the lognormal distribution,

$$p(r) = a \exp\left[-(\ln[r - \mu])^2 / (2\sigma^2)\right] \quad (3.5)$$

following Riquelme et al. (2013) as previously discussed. In (4.5), $p(r)$ is the probability that any bubble of a given population of size r microns is observed, a is the probability at the peak of the distribution, μ is the mean of the bubble distribution, and σ is the variance of the bubble size distribution. The three parameters of the lognormal distribution a , μ , and σ were determined for both monochromatic and JONSWAP spectrum wave conditions and expressed in terms of wind-wave Reynolds number Re_{H_w} in Figure 4.12.

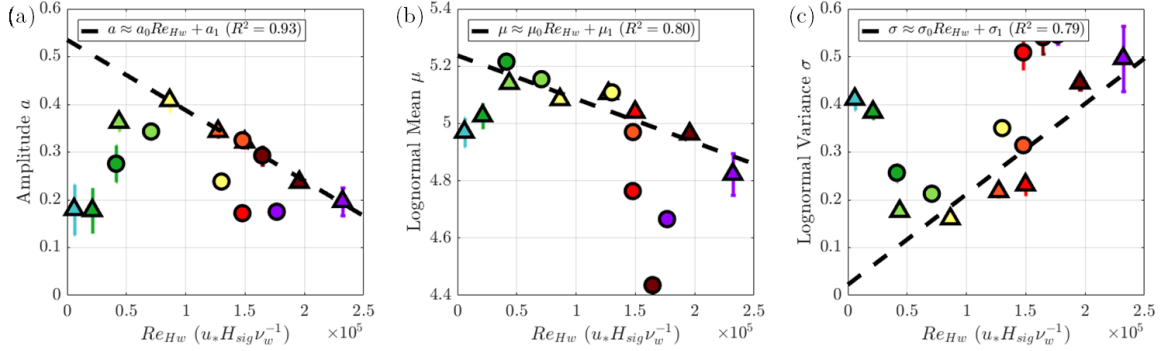


Figure 4.12 Lognormal distribution parameters and their relationship to the wind-wave Reynolds number Re_{Hw} . (a) Distribution amplitude a (b) mean μ and (c) variance σ . Colors indicate the 10-meter neutral wind speed U_{10N} and as previously, circles and triangles represent the data from monochromatic and JONSWAP spectrum wave conditions.

In Figure 4.12, there are three different types of behavior the parameters show as a function of Re_{Hw} , which we refer to as growth, occasional clustering, and saturated clustering phases. For $Re_{Hw} \leq 0.75 \times 10^5$ a and μ with wind speed and σ decreases, the average number and size of bubbles increase however the bubble population is still relatively narrow (growth phase). Occasional clustering occurs for $0.75 \times 10^5 < Re_{Hw} \leq 1.25 \times 10^5$, where some groups of larger bubbles can be seen grouped together in clusters however may individual bubbles remain free or separate in the field of view. Here, regardless of wave condition, the bubble size distribution broadens to include more bubble radii and increasingly smaller bubble sizes (μ decreases and σ increases). Furthermore, the likelihood of observing a particular size of bubble decreases (a decreases). At values of $Re_{Hw} > 1.25 \times 10^5$, depending on wave condition, the field of view of the bubbles becomes brighter and quite saturated (see Figure 4.10). Here, the bubble size distributions continue to broaden and the average bubble size continues to decrease.

We posit that the degree of clustering and image saturation are directly related to the presence of wave-induced sub-surface turbulence shearing apart bubbles and subsequent cohesion of the small bubbles. In Figure 4.12, the black dashed lines show the linear fit to JONSWAP spectrum wave conditions exclusively and intentionally. We choose this because a spectrum of waves is more consistent with open ocean wave observations (Hasselmann, et al. 1973; Holthuijsen and Herbers, 1986) and wave breaking occurs at multiple scales not just at a single wave frequency (Gemmrich, 2010). In the next section, we validate the bubble size distribution parameterization and discuss the distributions resulting from its use.

4.2.4 Validation of bubble size distribution parameterization

The parameterization inputs were found to depend on the magnitude of the wind stress and wave height relative to penetration resistance due to water viscosity, as conveyed by the wind-wave Reynolds number Re_{Hw} . For each JONSWAP spectrum wave experiment, the parameters of the bubble size distributions were compared with the parameterized fits,

$$a_{\text{param}} \approx a_0 \text{Re}_{Hw} + a_1 \quad (3.6)$$

$$\mu_{\text{param}} \approx \mu_0 \text{Re}_{Hw} + \mu_1 \quad (3.7)$$

$$\sigma_{\text{param}} \approx \sigma_0 \text{Re}_{Hw} + \sigma_1 \quad (3.8)$$

where in (4.6), $a_0 = -1.475 \times 10^{-6}$ and $a_1 = 0.54$. In (4.7), $\mu_0 = -1.514 \times 10^{-6}$ and $\mu_1 = 5.24$ and in (4.8), $\sigma_0 = 1.895 \times 10^{-6}$ and $\sigma_1 = 0.022$. The variance in the observed parameters across bubble distributions from each set of 10 shadowgraph images relative to the parameterized values are shown in Figure 4.13 below.

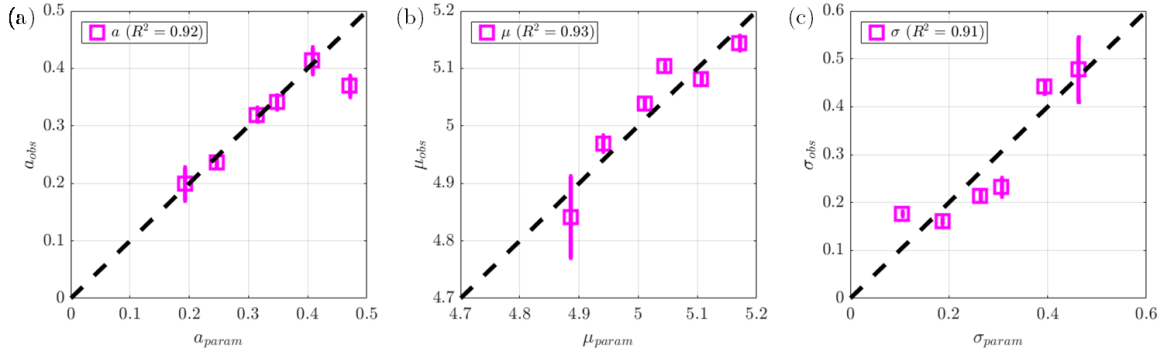


Figure 4.13 Linear regression fit between parameterized and observed lognormal distribution variables (a) a (b) μ and (c) σ from the JONSWAP wave spectrum experiments. The magenta squares give the mean value across 10 bubble size distributions from each experiment. The black dashed line is 1:1. Error bars are 1 standard deviation. Pearson R^2 values are given in each panel, respectively.

Variance in the observed lognormal distribution parameters was of order $O(10^{-4} - 10^{-3})$ and the largest values were seen in Experiment 29, where the wind speed was largest and bubble size distributions may have varied in conjunction with wave breaking occurring at the surface. Nevertheless, the parameterizations in (4.6), (4.7), and (4.8) yield correlation coefficients of 0.92, 0.93, and 0.91, respectively. Runs 30 and 31 were omitted from Figure 4.13 based on examination of the bubble images, which are sparsely populated to the degree that shadowgraph lens imperfections, streaks from deposited water droplets and other objects yield poorly defined distribution peaks and discontinuous radius bins.

To further quantify the error of observed and parameterized bubble size distributions, the average of the 10 distributions from each experiment (derived from 10 shadowgraph images) was compared with a constructed lognormal distribution using expected amplitude a_{param} , mean μ_{param} , and variance σ_{param} values from equations (4.6), (4.7), and (4.8). Histograms of the observed distributions are overlain with the parameterized lognormal PDF along with R^2 values in Figure 4.14.

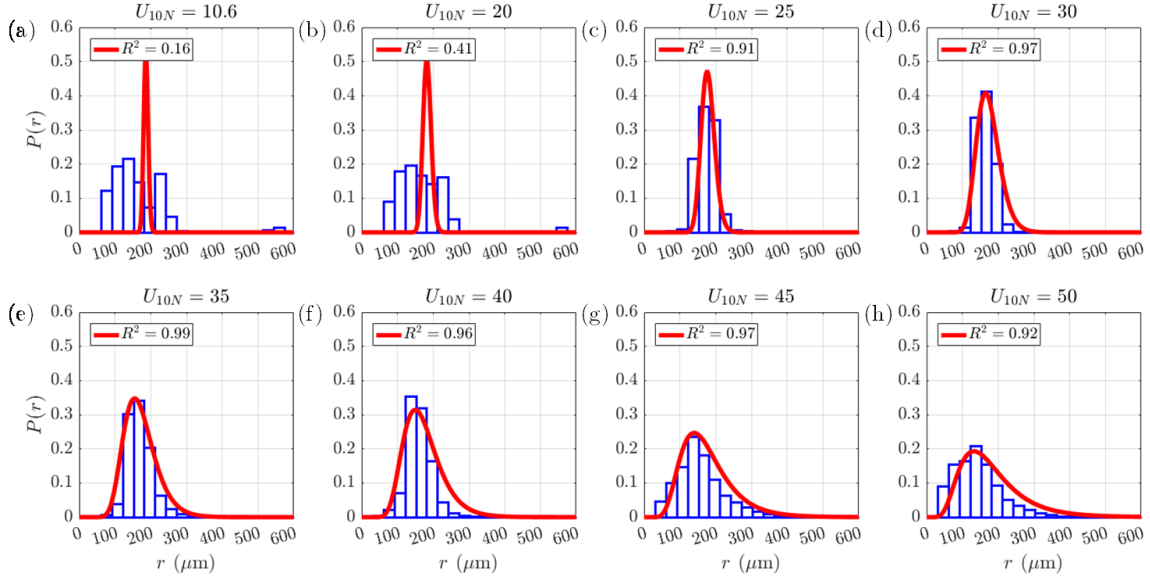


Figure 4.14 Observed and parameterized bubble size distributions in the JONSWAP spectrum wave conditions. Histograms depicting the observed distributions are in blue bars, the parameterized distribution is plotted in red. Pearson correlation coefficients for each are given in each panel. The title indicates the wind speed in each panel (a) – (h).

In Figure 4.14, we see that the parameterized bubble size distributions agree well with the average observed distributions for wind speeds $U_{10N} \geq 25 \text{ ms}^{-1}$, with $R^2 > 0.90$ in those cases. The most probable radius observed as indicated by the peaks in $P(r)$ decreases from $r = 176 \mu\text{m}$ to $r = 133 \mu\text{m}$ as wind speed increases from $U_{10N} = 25 \text{ ms}^{-1}$ to $U_{10N} = 50 \text{ ms}^{-1}$ with bin width $dr = 30.25 \mu\text{m}$ in each panel of Figure 4.14. The agreement is poor in the low wind speeds (panels (a) and (b)) and the distributions (blue bars) are almost identical ($R^2 = 0.97$ between distributions in Figure 4.14(a) and (b)) because wind stress and subsequent wave heights are insufficient to entrain many bubbles at all, which impacts the brightness gradients in images and the separation of foreground and background involved in the bubble identification process.

Although we chose to construct and validate bubble size distribution parameterizations using data from JONSWAP wave spectrum experiments, in Figure 4.12 we could have linearly fit the data from the monochromatic wave experiments instead as

any bubble size distribution could be characterized using a lognormal distribution (Riquelme et al. 2013). In such case, the slopes a_0, μ_0, σ_0 would have been steeper. The differences in these slopes compared with JONSWAP wave spectrum conditions reflects the more intense and frequent wave breaking occurring in monochromatic wave conditions, resulting in a more rapid decrease in average bubble size and more rapid increase in bubble size variance. To that end, we fit to the monochromatic data and find $a_0 = -1.719 \times 10^{-6}$, $\mu_0 = -3.938 \times 10^{-6}$, and $\sigma_0 = 3.397 \times 10^{-6}$. Applying these coefficients to Equations (4.6), (4.7), and (4.8), we compare observed and parameterized distributions in monochromatic conditions in Figure 4.15.

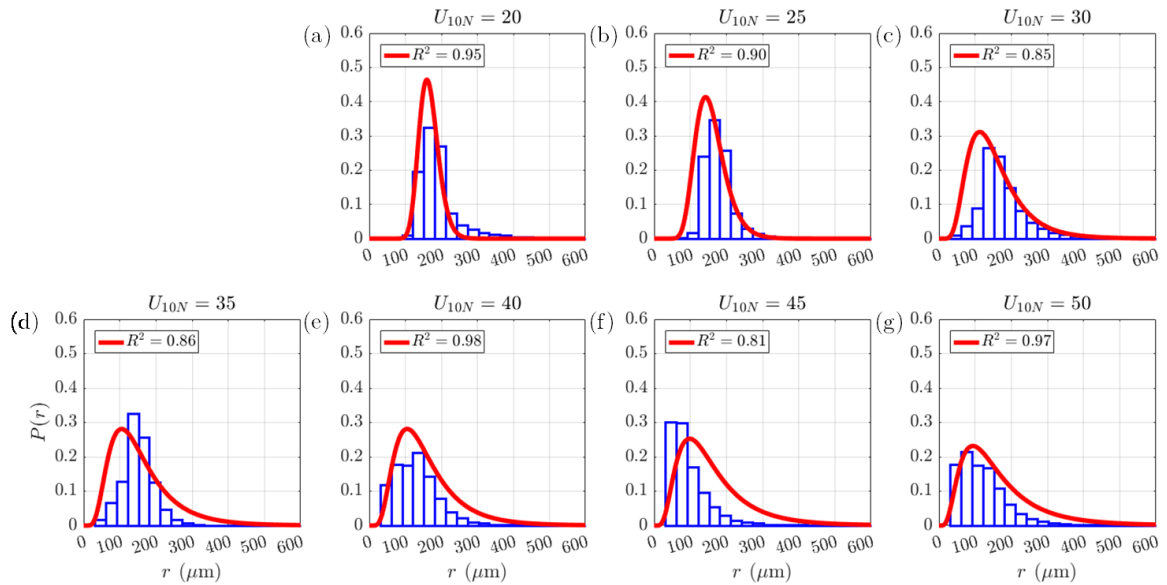


Figure 4.15 Observed and parameterized bubble size distributions in the monochromatic wave conditions. Histograms depicting the observed distributions are in blue bars, the parameterized distribution is plotted in red. Pearson correlation coefficients for each are given in each panel. The title indicates the wind speed in each panel (a) – (g).

As in JONSWAP wave spectrum conditions, bubble size distributions broaden with increasing wind forcing and the average bubble size decreases. In Figure 4.15, we see the parameterization-derived distributions have lower R^2 values than those in the JONSWAP

cases (excepting Experiments 30 and 31); nevertheless, the correlation coefficients are 0.80 or greater. In both JONSWAP spectrum and monochromatic wave conditions, the bubble loss rates $\partial P(r) \partial r^{-1}$ decrease with increased wind stress as simultaneously the average distribution mean μ decreases (bubble size decreases). This loss rate decreases because the average bubble size shifts towards smaller radii, which bubble images indicate occurs at the same time bubbles are not only observed to be smaller but as they cluster together and interact. Since wave breaking and the turbulent kinetic energy flux associated with it are integral to the production and separation of bubbles across a variety of radii, in the next subsection, we complete the connection between sea surface structure and subsurface turbulence using surface wave and sub-surface ADCP data.

4.3 Wave-scaled sub-surface turbulence dissipation

In this section, we report laboratory measurements of subsurface turbulence and dissipation as measured by high-frequency 3D ADCP in the aforementioned monochromatic and JONSWAP spectrum wave conditions, extending previous data to the hurricane-force wind environment. Terray et al. (1996) and Drennan et al. (1996) used a wave-scaling of dissipation rate measured beneath a fixed tower in Lake Ontario adjacent to the Canada Centre for Inland Waters (CCIW) and underway vessel R/V *Frederick G. Creed*, respectively. Here, we apply this method to the laboratory data collected in the SUSTAIN facility, in which dissipation rates were measured at similar fetch and near to the bubble imager system we previously described. The wave-scaled dissipation rate term from Drennan et al. (1996) is

$$\frac{\varepsilon H_{\text{sig}}}{F} \quad (3.9)$$

where ε is dissipation rate of TKE, H_{sig} is significant wave height, and F is the rate of energy input from wind to waves,

$$F = g \int \beta S_\eta d\omega d\theta \quad (3.10)$$

where g is the gravitational acceleration, β is the wave growth rate, and S_η is the water surface elevation spectrum. The subsections which follow report the results of computation of β , F , and $\varepsilon H_{sig} F^{-1}$, respectively.

4.3.1 Wave growth rate in monochromatic and spectrum waves

For each experiment, wave growth rate was calculated following Equation (1.13) originally defined by Donelan and Pierson (1987) and described in Donelan and Plant (2009). Wave phase speed, wavenumber, and angular frequencies were determined from the individual wave crest analysis of water surface elevation data collected via the laboratory wave wire array. Wind speed at half wavelength height $U_{L/2}$, which is needed to compute β was estimated using Equation (2.24). Although the water was heated or cooled to predetermined temperatures prior to each experiment using the laboratory heat exchanger, this system was turned off during experiments. To account for the effects of water temperature via water viscosity, we also calculated the ‘measured’ growth rate by subtracting viscous dissipation,

$$\beta_m = \beta - 4\nu_w k(\omega, \theta)^2 \quad (3.11)$$

where ν_w is the water viscosity (m^2s^{-1}) and k is the wavenumber. First, we present β_m as a function of the angle θ relative to the wind (which was coming from 0 degrees in the coordinate system of the wave wire array, from the tank inlet) as well as the average wave growth rate in each wave condition versus U_{10N} in Figure 4.16.

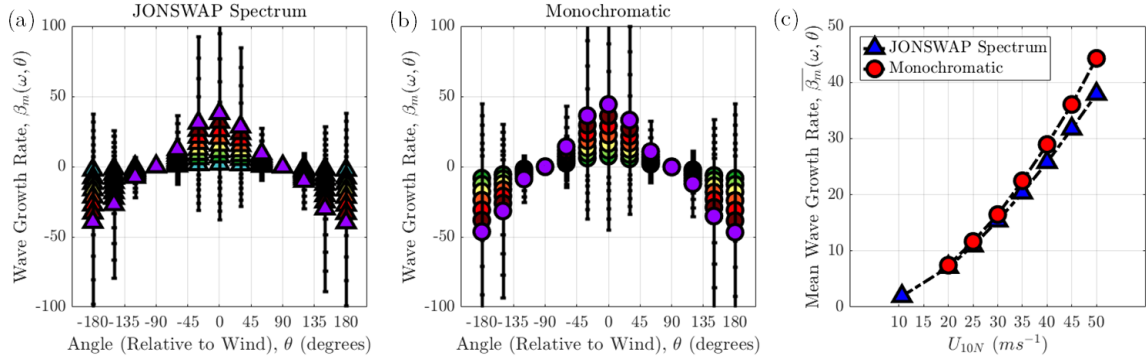


Figure 4.16 Measured wave growth rate $\beta_m(\omega, \theta)$ in (a) JONSWAP wave spectrum conditions during Experiments 27-34 and (b) monochromatic wave conditions during Experiments 1-8. Average wave growth rate (across angular frequency ω for $\theta=0$) as a function of wind speed is given in panel (c). In panels (a) and (b), the mean wave growth rates are indicated by triangles or circles colored by U_{10N} . Black error bars indicate 1 standard deviation.

Wave growth rates shown in Figure 4.16 above have units rad s^{-1} , that is, radians (i.e. of a circle) elapsed per unit time. Hence, what is depicted by the growth rate is the change in steepness of wave crests of different frequencies based on the angle the associated wave crests have relative to the wind direction. Regardless of the wave condition, the growth rate is positive when $\cos \theta > 0$ ($\theta = (-90, 90)$) and zero or negative otherwise. Variance in β_m is largest for $\theta \Rightarrow n\pi \in n=0,1,2$ as these are angles closer to being aligned with or opposed to the wind. Taking the values of β_m where $\theta \equiv 0$ (aligned with the wind), the average wave growth rate increases by 0.48 rad s^{-1} per $\text{ms}^{-1} U_{10N}$ in JONSWAP spectrum wave conditions and 0.80 rad s^{-1} per $\text{ms}^{-1} U_{10N}$ in monochromatic wave conditions. These differences can be seen clearly in Figure 4.16 (c), where wave growth rates are larger per unit wind speed in monochromatic conditions than JONSWAP spectrum wave conditions, however most noticeably for $U_{10N} \geq 30 \text{ ms}^{-1}$ where growth rates in the former exceed the latter by between 10.4 and 16.7 percent. Additionally, the average

wave growth rate has a quadratic relationship with wind speed, consistent with theory (Jeffreys 1924; Miles 1957) and measurements from prior literature (Plant, 1982).

4.3.2 Wind input to waves

Directional wave spectra $S_n(\omega, \theta)$ constructed via WDM (Donelan, et al. 1996) using the triangular array of wave wires are plotted in polar coordinates for both JONSWAP spectrum and monochromatic experiments in Figures 4.17 and 4.18, respectively. These spectra are then multiplied by wave growth rate and integrated for F .

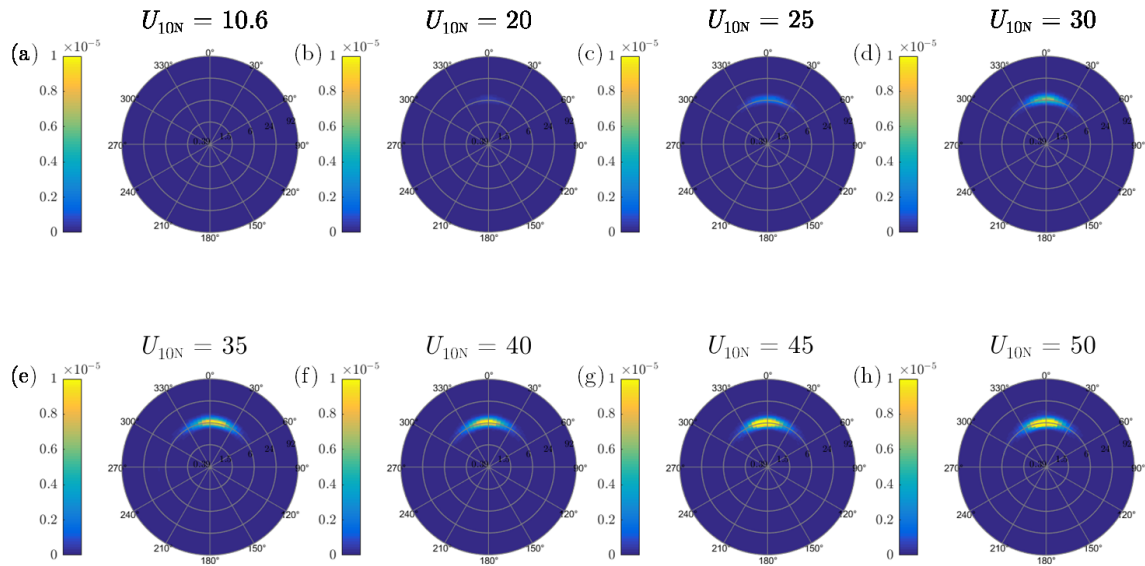


Figure 4.17 Directional wave spectra for JONSWAP spectrum conditions in Experiments 27-34 plotted in polar coordinates. Each polar plot has the same value axis, and the wind speed is given above each plot.

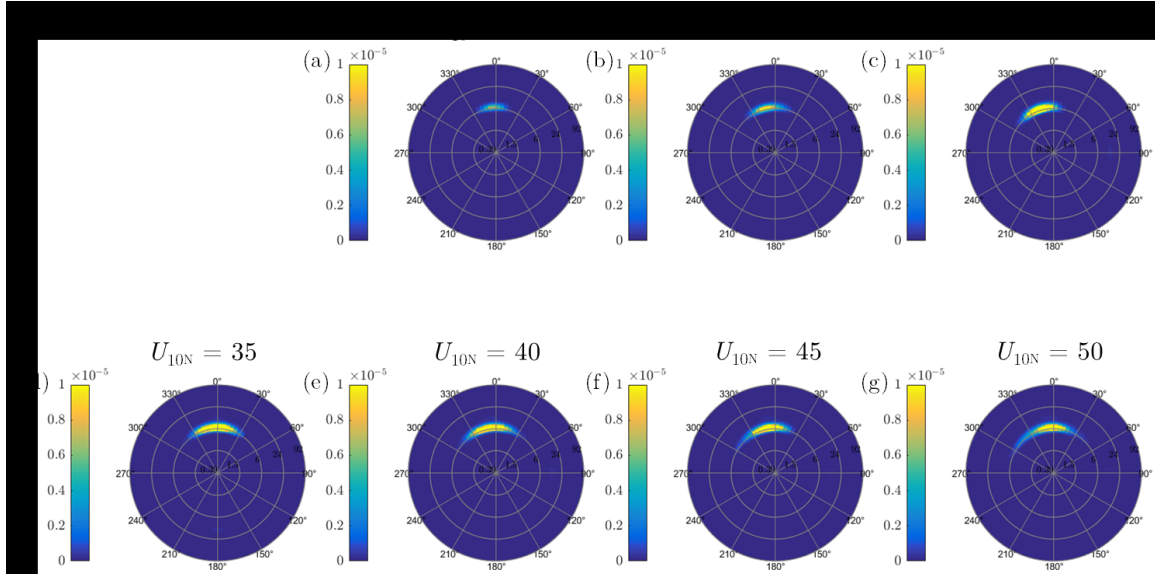


Figure 4.18 Directional wave spectra for monochromatic conditions in Experiments 1-8 plotted in polar coordinates. Each polar plot has the same value axis as in Figure 4.17, and the wind speed is given above each plot.

In both wave conditions, the wave energy increases in magnitude and/or radial spread with increasing wind speed and is predominantly observed within $\pm 60^\circ$ of the wind direction. Most wave energy, particularly at high winds, is confined even more narrowly to within $\pm 30^\circ$ of the wind direction, and is noticeably broader-banded in the JONSWAP spectrum plots (e.g., compare Figure 4.17h, Figure 4.18g). Since the wave wire array is fixed and stationary throughout all experiments, we believe deviations in wave energy bands from being oriented towards the wind direction are caused by either reflections or tension issues on the starboard wave wire (e.g. Figure 4.18b, c, e, f). Taking slices from the directional spectra along the 0° angle, the wave energy band ranges from $df = 0.835 - 1.636$ Hz wide in JONSWAP spectrum conditions and $df = 0.835 - 1.034$ Hz wide in monochromatic conditions, respectively, as the wind speed increases.

To verify the directional wave spectra conform to expected magnitude, the significant wave height calculated from the water surface elevation data were compared

with manual calculation via $H_{sig} = 4 \times \sqrt{m_0}$ where $m_0 = \int S_\eta(\omega, \theta) d\omega d\theta$ is the first statistical moment of the wave spectra. The results of the linear fit of the two significant wave height measurements are given in Figure 4.19.

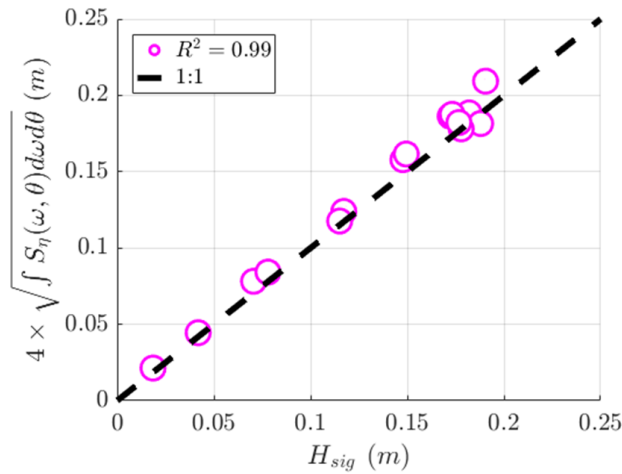


Figure 4.19 Significant wave height calculated from wave-wire water surface elevation timeseries compared with manual calculation using the directional wave spectra constructed using wavelet directional method (WDM). Plot includes both JONSWAP spectrum and monochromatic wave values from Experiments 27-34 and Experiments 1-8.

From Figure 4.19, the significant wave heights calculated by the two methods agree with a Pearson correlation coefficient $R^2 = 0.99$ and satisfy us that the magnitude of the energy in the directional wave spectra is accurate. Given this, we now present the projection of wave growth rate onto the surface wave directional spectrum $\beta S_\eta(\omega, \theta)$ as a function of angular wave frequency ω and θ ; this projection shows the frequency and direction at which the greatest energy input from wind to waves would be observed and is given in Figure 4.20.

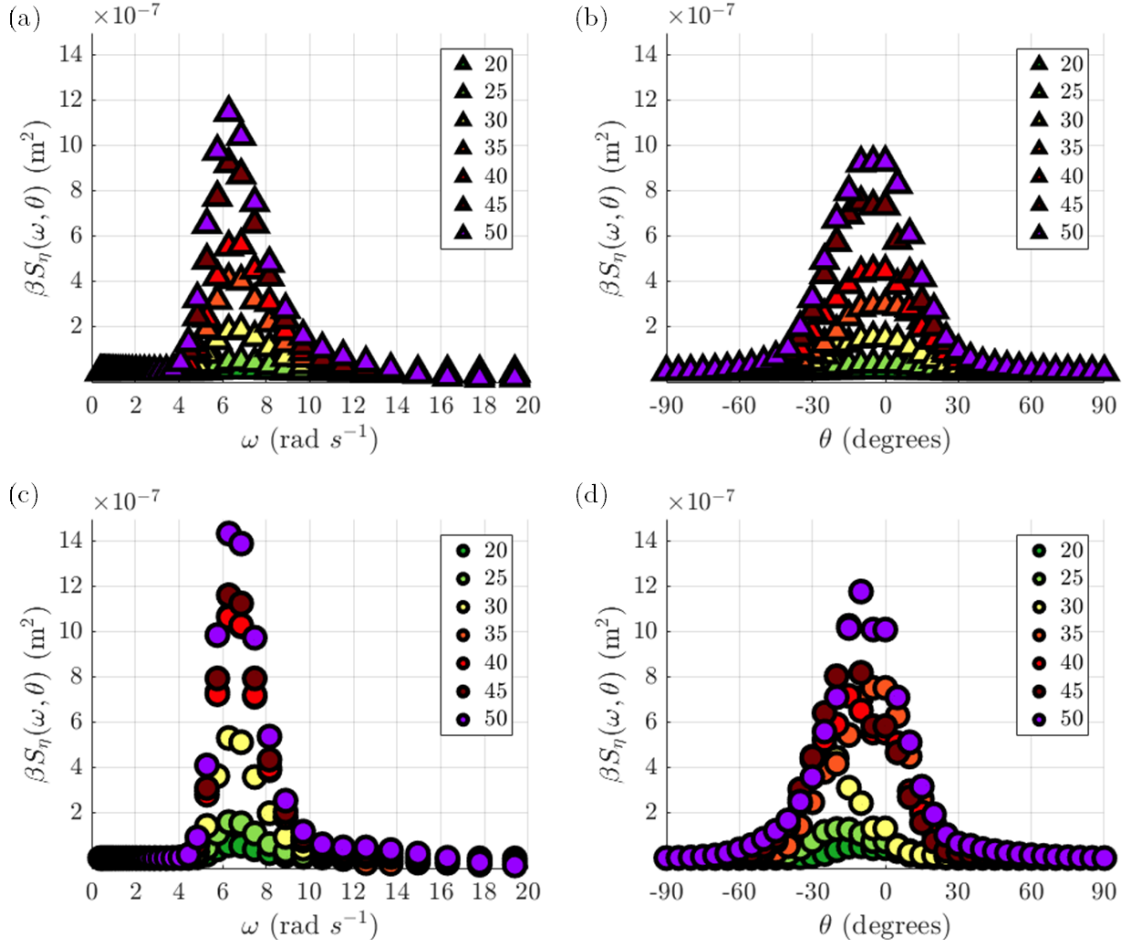


Figure 4.20 Product of wave growth rate and directional wave spectrum averaged over angular wave frequency (a, c) and wave direction (b, d) from (a, b) JONSWAP spectrum experiments 27-34 and (c, d) monochromatic experiments 1-8. Data are colored by U_{10N} indicated in the legends.

Averages of the product of wave growth rate and directional wave spectra in Figure 4.20 show the energy input from the wind was largest near the peak angular wave frequency $\omega_p \approx 6.283 \text{ rad s}^{-1}$ and in the direction of the wind within about $\pm 30^\circ$. Energy input to waves resulting from double integration of Figure 4.20 (a, c) has greater magnitude in the monochromatic wave conditions (25.2 percent larger than JONSWAP spectrum values) but is spread over a narrower range (20.9 percent smaller range) of angular wave frequencies. Based on U_{10N} , wind stress τ , and angular frequency ω measurements in the

two wave conditions, we quantified the wind stress per unit angular wave frequency $\tau\omega^{-1}$ as a function of U_{10N} .

For JONSWAP spectrum wave conditions, the approximate linear fit is $\tau\omega^{-1} \approx 1.09 \times 10^{-3} \text{ kg m rad}^{-1} \text{ s}^{-1}$ monotonically increasing with $R^2 = 0.99$. In monochromatic conditions, for wind speeds $U_{10N} < 35$ the linear fit has a very similar slope, $\tau\omega^{-1} \approx 0.98 \times 10^{-3} \text{ kg m rad}^{-1} \text{ s}^{-1}$ ($R^2 = 0.99$); however, for higher wind speeds the stress per wave frequency decreases as $\tau\omega^{-1} \approx -0.08 \times 10^{-3} \text{ kg m rad}^{-1} \text{ s}^{-1}$. Therefore, although the division of wind stress across wave frequencies is similar in the two wave conditions at low to moderate winds, at high winds monochromatic waves are subject to less wind stress and a higher range of wave angular frequencies ω . Finally, we performed double integration to calculate F and compared the values observed in the laboratory to those from open ocean ship measurements given in Drennan et al. (1996), which are shown in Figure 4.21.

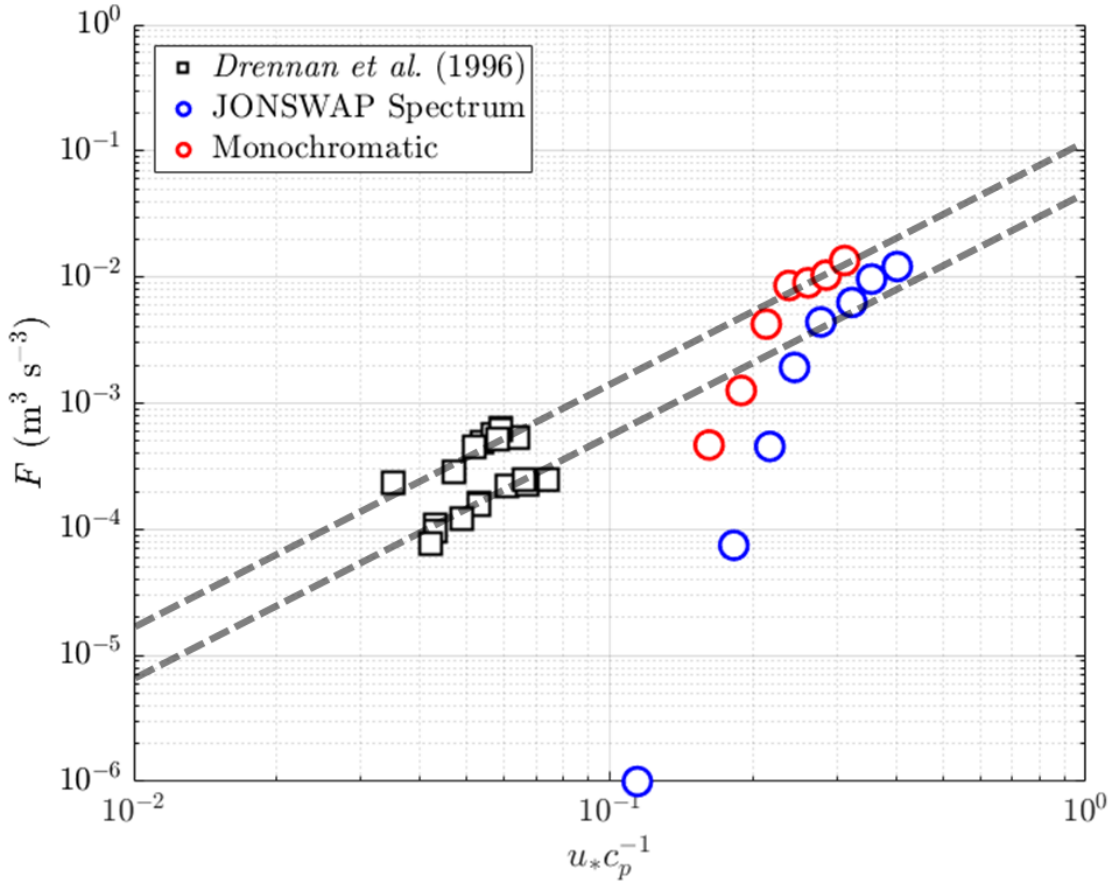


Figure 4.21 Energy input from wind to waves F as a function of inverse wave age $u_* c_p^{-1}$ from Drennan et al. (1996) in black squares, and from the SUSTAIN wind-wave tank in circles. Wave condition is indicated by the color and legend. The black dashed lines correspond with $F \approx \alpha_F (u_* c_p^{-1})^2$ where $\alpha_F = 0.132$ in the upper dashed line and $\alpha_F = 0.076$ in the lower dashed line.

In Figure 4.21, the energy input from wind to waves F is plotted on logarithmic axes as a function of the inverse wave age $u_* c_p^{-1}$. F responds to inverse wave age through β and such a relationship has been discussed in prior studies that calculate F (Terray et al. 1996; Drennan et al. 1996). Two distinct groups of F can be seen in Figure 4.21 for both the data from Drennan et al. (1996) and from the laboratory in our study. The separation in magnitude (y-axis) is due to the significant wave height differences in each set of data. The two datasets from Drennan et al. (1996) have average significant wave heights

$\bar{H}_{sig} = 1.93 \pm 0.4$ meters (upper dashed line in Figure 4.21) and $\bar{H}_{sig} = 1.04 \pm 0.20$ (lower dashed line) meters, respectively. In the respective datasets, the average peak wave frequency f_p was 0.176 Hz and 0.255 Hz, respectively. The two datasets from the SUSTAIN laboratory were of course, monochromatic and JONSWAP spectrum wave cases. Average significant wave height in these laboratory cases was 0.11 meters and 0.16 meters, respectively.

Comparing inverse wave age values from Drennan et al. (1996) Table 1 with our laboratory values, we see that the latter are on average 4.6 times larger than the former, as the laboratory included wind speeds up to $U_{10N} = 50 \text{ ms}^{-1}$, whereas the largest 12-meter wind speed from Drennan et al. (1996) was 11.99 ms^{-1} . Drennan et al. (1996) also have lower peak frequency than the waves observed in the laboratory, which were near 1 Hz. Hence, the two dashed lines in Figure 4.21 fit data from waves with greater wave height, lower peak frequency, and larger wave age (upper line) and another set where waves have a smaller significant wave height, higher peak frequency, and smaller wave age.

We pause to address the discrepancies in F observed for $U_{10N} < 30 \text{ ms}^{-1}$ in Figure 4.21, where values are much smaller than the dashed line fits would yield. In the laboratory, we produce background mechanical paddle waves on which wind operates. Given that the wave breaking and bubble statistics already suggest that $U_{10N} \approx 25 - 35 \text{ ms}^{-1}$ is a transition region for breaking and turbulence-driven bubble breakup (see Figures 4.4, 4.12), we hypothesize that differences in slope $\partial F \partial u_* c_p^{-1}$ between our data and Drennan et al. (1996) at lower winds are the result of paddle-driven laboratory waves having less roughness and

height compared with open ocean, purely wind driven waves. As a consequence, F is under-estimated in our laboratory data at low winds. In the next subsection, we use ADCP data to report sub-surface turbulence and dissipation rates. These dissipation rates allow the wave-scaled quantity in (4.9) to be calculated.

4.3.3 Sub-surface turbulence and wave-scaled TKE dissipation rates

A Nortek Vectrino II 3-D acoustic Doppler current profiler (ADCP) placed directly down-fetch of the bubble imager and forward-most full-length wave wire captured sub-surface velocities over a 0.03-meter vertical profile approximately 0.30 meters below the SUSTAIN laboratory air-water interface. In accordance with Nortek manufacturer guidance, velocities and subsequent derived data were taken from a 0.012-meter section of the data profile including the center-most point, where signal to noise ratio (SNR) is near its maximum. As previously described, the ADCP velocity data were de-spiked using a 3D phase space algorithm described in Goring and Nikora (2002). The average water velocity

$$\bar{U}_w = \sqrt{\bar{u}_w^2 + \bar{v}_w^2 + \bar{w}_w^2}, \text{ water-side friction velocity } u_{*w}, \text{ and average SNR from each wave}$$

condition are given in Figure 4.22

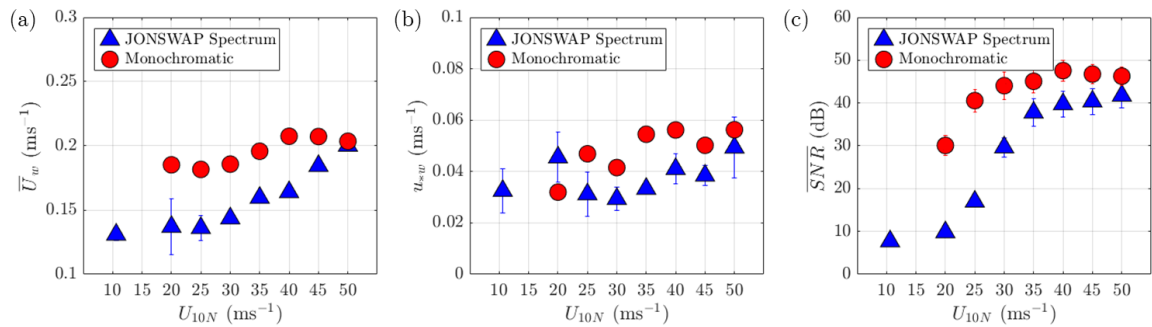


Figure 4.22 Vectrino II 3-D ADCP derived (a) mean water velocity, (b) water-side friction velocity, and (c) signal to noise ratio (SNR) in JONSWAP spectrum (blue triangles) and monochromatic (red circles) wave conditions. Each point is an average taken over the 0.012-meter region of the measurement profile. Error bars are indicated in each figure.

From Figure 4.22, we observe larger average water velocity, friction velocity, and SNR in monochromatic wave conditions, each increasing up to $U_{10N} = 40 \text{ ms}^{-1}$. Average values in these monochromatic conditions exceed JONSWAP spectrum values by 23.1 percent, 50.7 percent, and 65.6 percent for velocity, friction velocity, and SNR, respectively. Larger values of friction velocity and SNR in monochromatic wave conditions are consistent with more frequent and intense wave breaking and the subsequent introduction of more bubbles acting as scatterers. Consequently, SNR is larger in the monochromatic wave conditions, however disparity in the values between wave conditions becomes smaller for all variables depicted in Figure 4.22 at high winds.

In monochromatic wave conditions, we notice a decrease in \bar{U}_w , u_{*w} , and SNR at and above $U_{10N} = 40 \text{ ms}^{-1}$ which we attribute to intense winds tearing off the tops of wave crests, thus reducing the intensity of breaking and the entrained air volume that follows. Again, based on Nortek guidance for use of the Vectrino II ADCP, the SNR should be a minimum of 30 dB throughout the profile region we take our data from. Based on Figure 4.22(c), SNR was lower than or near recommended guidelines in JONSWAP wave conditions where $U_{10N} \leq 30 \text{ ms}^{-1}$ and similarly insufficient in monochromatic wave conditions where $U_{10N} \leq 20 \text{ ms}^{-1}$. Therefore, we expect linkage between the surface waves, bubbles and sub-surface turbulence to be difficult or untenable in these conditions given the instrument and measurement limitations (see also Figure 4.21).

Velocity timeseries $u_w(t)$, $v_w(t)$, and $w_w(t)$ were used to calculate the turbulent kinetic energy (TKE) dissipation rate ε as previously discussed in Chapter 2 (Sec. 2.3.2) by invoking Taylor's frozen turbulence hypothesis (Taylor, 1931) and following Equation (1.8). Each velocity timeseries was decomposed into wave-coherent, turbulent, and noise

components, and the velocity spectra were used to determine the inertial sub-range with the Algorithm for Robust Identification of the Inertial Sub-range (ARIIS) (Ortiz-Suslow, et al. 2019). Figure 4.23 and Figure 4.24 show the results of adapting ARIIS to these sub-surface velocity spectra in the JONSWAP and monochromatic wave conditions, respectively.

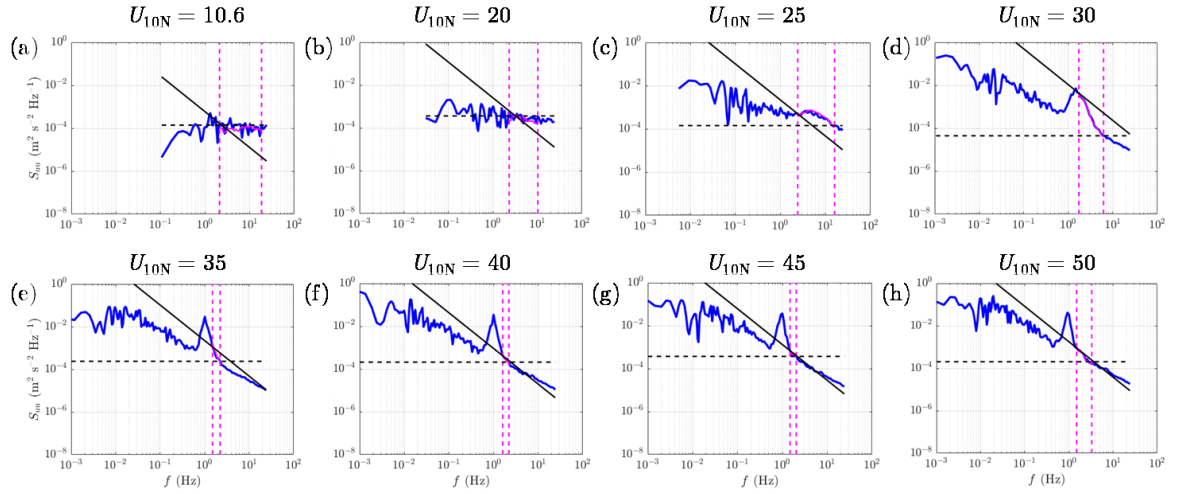


Figure 4.23 Vectrino II 3-D ADCP derived zonal water velocity spectra $S_{uu}(f)$ and isotropic region identified by ARIIS for JONSWAP wave spectrum conditions, experiments 27-34. Spectra are shown in blue, the solid black line is $f^{-5/3}$, the dashed black line is zero slope, and the magenta lines bound the identified inertial sub-range. Wind speed is given above each figure.

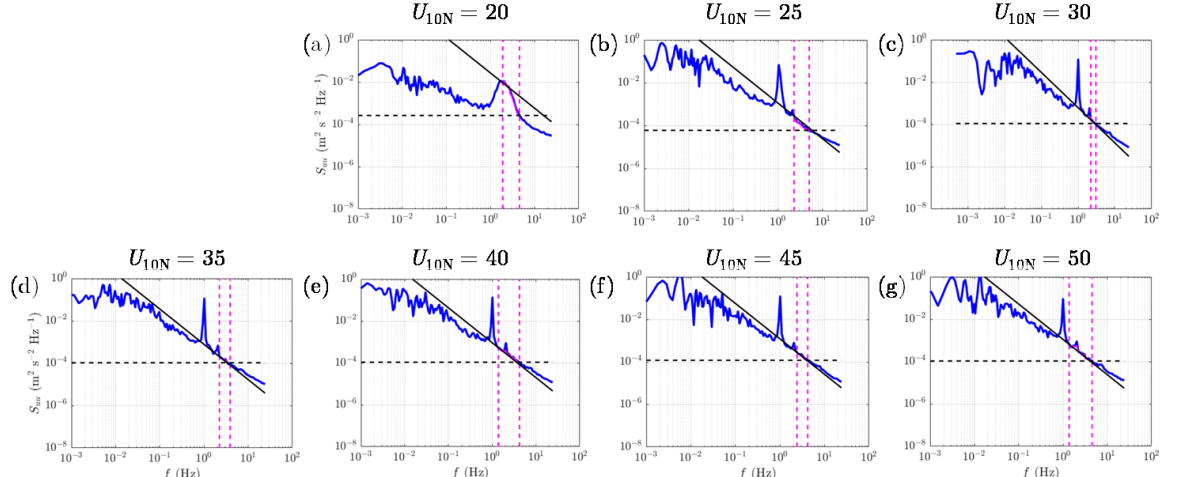


Figure 4.24 Vectrino II 3-D ADCP derived zonal water velocity spectra $S_{uu}(f)$ and isotropic region identified by ARIIS for monochromatic wave conditions, experiments 1-

8. Spectra are shown in blue, the solid black line is $f^{-5/3}$, the dashed black line is zero slope, and the magenta lines bound the identified inertial sub-range. Wind speed is given above each figure.

When executing ARIIS, the isotropic frequency band was first identified as a region to search, followed by iterative robust fitting to determine the inertial sub-range corresponding to a slope of $f^{-5/3}$. In Figure 4.23, panels (a)-(d) show the identified inertial sub-range Δf was larger ($\overline{\Delta f} = 10.54 \text{ Hz}$ for $U_{10N} \leq 30 \text{ ms}^{-1}$ versus $\overline{\Delta f} = 0.92 \text{ Hz}$ for $U_{10N} > 30 \text{ ms}^{-1}$) and the spectra, particularly for (a) – (c) were flat or near flat at frequencies lower than the expected peak near $f \approx 1.00 \text{ Hz}$. Spectra throughout the figure show evolution of the wave band, whose peak shifts from $f_p = 4.30 \text{ Hz}$ to $f_p = 0.93 \text{ Hz}$ as wind speed increases from panels (c) to (h). The inertial sub-range slopes for velocity spectra where surface wind speeds $U_{10N} \geq 35 \text{ ms}^{-1}$ were -2.05,-1.73,-1.67, and -1.67, respectively. At wind speeds less than this, the portion of the turbulence spectra determined to be isotropic includes wave band energy contributions.

For comparison, we show the evolution of velocity spectra and inertial sub-ranges beneath monochromatic waves in Figure 4.24. At the lower wind speeds, again the dominant wave band may be part of the identified inertial sub-range as in panel (a). The wave band is also broader for $U_{10N} \leq 25 \text{ ms}^{-1}$, whereas for higher winds the band is consistent in width and shape. Spectral density is notably greater below the dominant wave frequency and the average inertial sub-range bandwidth is also larger (2.35 Hz versus 0.92 Hz) beneath monochromatic versus JONSWAP spectrum wave conditions where the wave band is clearly separated from the inertial sub-range ($U_{10N} > 35 \text{ ms}^{-1}$). Lastly, the average area beneath the turbulent spectra spanning the inertial sub-ranges were compared,

revealing the turbulent kinetic energy to be $5.65 \times 10^{-4} \pm 6.4 \times 10^{-4}$ m²s⁻² in high-wind ($U_{10N} > 35$ ms⁻¹) JONSWAP spectrum conditions and $1.001 \times 10^{-3} \pm 6.2 \times 10^{-4}$ m²s⁻² beneath monochromatic conditions – a difference of 76.9 percent. Based on these ARIIS results, we expect larger TKE dissipation rates beneath monochromatic wave conditions where the isotropic turbulence in the inertial sub-range extend to higher frequencies than those in spectrum wave conditions.

To conclude this sub-section, we calculated the TKE dissipation rates and scaled them via Equation (4.9), plotting the values as a function of wave-scaled depth zH_{sig}^{-1} as in Drennan et al. (1996) in Figure 4.25.

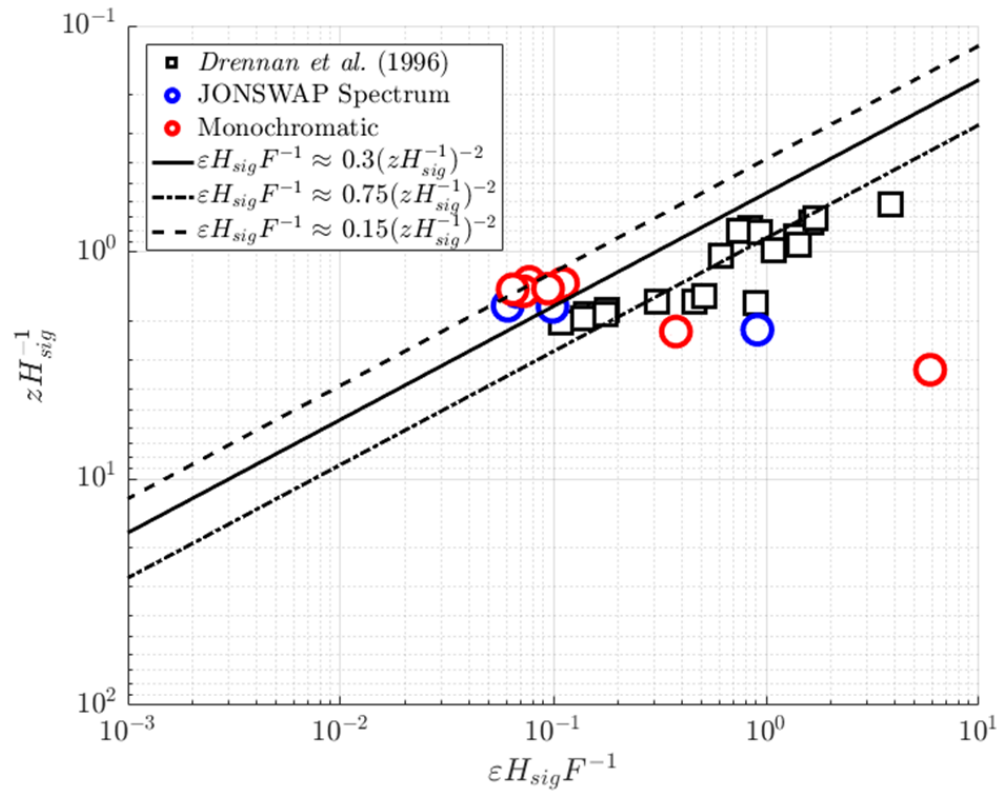


Figure 4.25 Wave-scaled dissipation rate $\varepsilon H_{sig} F^{-1}$ as a function of wave-scaled depth $z H_{sig}^{-1}$ as measured in Drennan et al. 1996 (black squares) and in the SUSTAIN wind-wave laboratory tank (circles). The black solid line is the best fit of WAVES data (Terray

et al. 1996) as depicted in Drennan et al. (1996) Figure 5. The other dashed lines are fits to the data from SWADE (Drennan et al. 1996) and SUSTAIN laboratory data.

In Figure 4.25, the wave-scaled dissipation rates from WAVES (Terray et al. 1996), SWADE (Drennan et al. 1996), and the SUSTAIN laboratory data are shown along with linear fits of the form $a(zH_{sig}^{-1})^{-2}$ coming from Drennan et al. (1996). Average significant wave height in SWADE, WAVES, and SUSTAIN laboratory data presented in Figure 4.25 were 1.44 meters, 0.22 meters, and 0.13 meters, respectively; consequently, the value of a in each linear fit reflects this. Laboratory outliers deviate from the expected fit because of low values of energy input term F and larger than realistic dissipation rate values due to low SNR in the Vectrino II ADCP data as previously discussed. Nevertheless, the TKE dissipation rates measured in the laboratory were compared against wind speed U_{10N} and energy input to waves F . Both are discussed below, and the latter is shown in Figure 4.26.

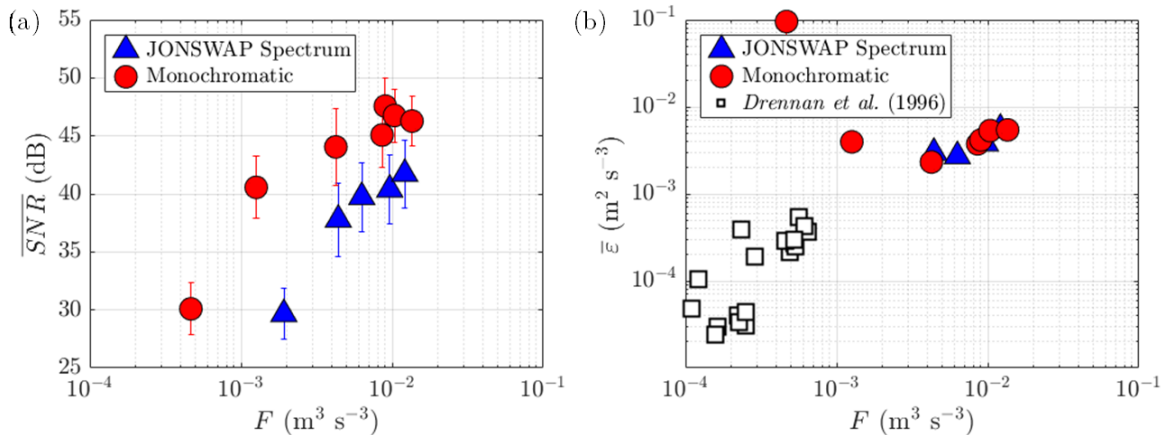


Figure 4.26 (a) Signal to noise ratio and (b) TKE dissipation rate averaged over the center of the Vectrino II 3-D ADCP profile. Blue triangles and red circles indicate the data from the laboratory wave conditions indicated in the legends. Dissipation rates derived from zonal sub-surface velocity spectra in Drennan et al. (1996) are shown in black squares in panel (b). Error bars are one standard deviation.

Considering aforementioned instrument limitations and observed SNR, we focus on the TKE dissipation rates measured where $U_{10N} \geq 30 \text{ ms}^{-1}$. TKE dissipation rates

spanned the range $\bar{\varepsilon} = 2.7 \times 10^{-3} - 5.6 \times 10^{-3} \text{ m}^2\text{s}^{-3}$ beneath JONSWAP spectrum waves and $\bar{\varepsilon} = 3.8 \times 10^{-3} - 5.4 \times 10^{-3} \text{ m}^2\text{s}^{-3}$ beneath monochromatic waves, respectively. Linear fits of dissipation rates with wind speed yielded slopes of $0.00018U_{10N}$ and $0.00012U_{10N}$ in JONSWAP spectrum and monochromatic conditions, respectively, indicating larger dissipation rate values but that increase more gradually. In Figure 4.26 (a), we see larger SNR is observed with increasing energy input from the wind (i.e. higher H_{sig} and inverse wave age). Subsequently, panel (b) shows the TKE dissipation rates from the laboratory and SWADE field observations (Drennan et al. 1996) as functions of F . Where the ADCP data quality is good, dissipation rates increase with additional wind input to waves (momentum flux) resulting in greater sub-surface shear production of TKE and ultimately its dissipation. Combining field and laboratory data, dissipation rates in Figure 4.26 (b) follow a power law fit $\bar{\varepsilon} \approx 0.19F^{0.82}$ with $R^2 = 0.98$.

4.4 Bubble spectra response to sub-surface turbulence

In prior literature from field studies (Blanchard and Woodcock, 1957; Medwin 1970, 1977; Johnson and Cooke 1979 and others) and laboratory experiments (Koga, 1982; Hwang, et al. 1991; Deane and Stokes 2002; Gemmrich and Farmer, 2004; Rensen, Luther and Lohse, 2005 and others), acoustic and optical techniques have been used to capture bubbles and connect the observed size distributions to surface wave conditions or sub-surface velocity and turbulence measurements. Here, we extend that effort in reporting linkage between sub-surface turbulent velocity spectra and bubble size distributions beneath an air-water interface composed of different wave conditions up to hurricane force wind conditions. We do this by identifying an estimate for the bubble Hinze scale (Hinze

1955; Deane and Stokes, 2002) in each set of conditions and relating this to ADCP-derived TKE dissipation rates.

4.4.1 Hinze scale

The bubble Hinze scale (c.f. Hinze, 1955), giving the approximate maximum radius surface tension maintains a bubble intact against the opposing turbulent shear forces is, as given in Deane and Stokes (2002),

$$a_H = 2^{-8/5} \varepsilon^{-2/5} (\gamma We_C / \rho)^{3/5} \quad (3.12)$$

where a_H is the Hinze scale in meters, ε is the TKE dissipation rate, γ is the surface tension, $We_C = 4.7$ is the critical Weber number, and ρ is the water density. Figure 4.27, adapted from Deane and Stokes (2002), puts Equation (4.12) into the context of bubble size distributions.

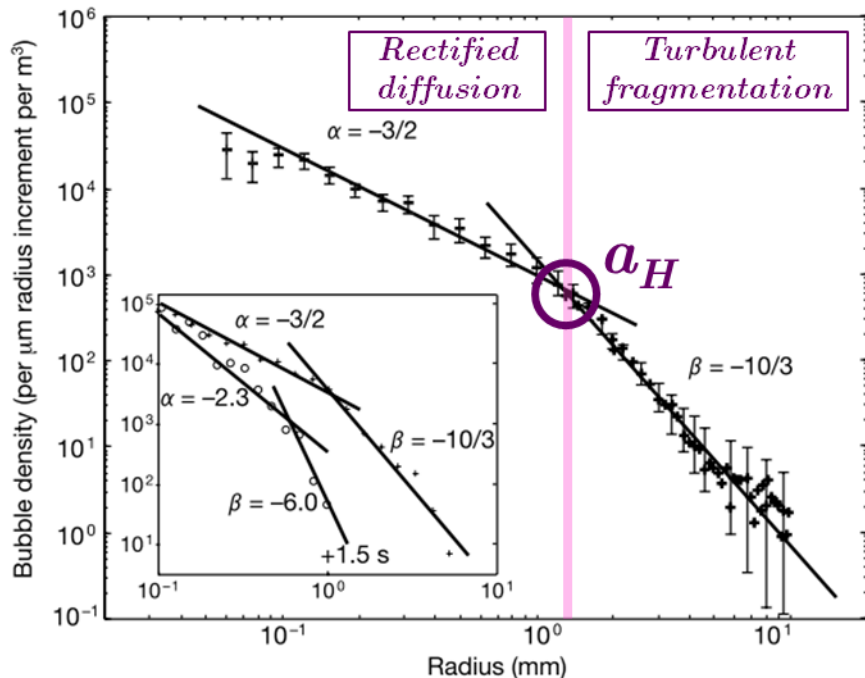


Figure 4.27 Average bubble size distribution estimated from 14 breaking events during their acoustic phase. Error bars show one standard deviation. The inset shows the bubble size distribution 0 seconds (crosses) and 1.5 seconds into the quiescent phase (open circles). The Hinze scale is identified in this figure by the purple circle and magenta line at the bubble radius where the slope changes.

In Figure 4.27, we have highlighted the Hinze scale a_H at the intersection of two linear fits to the average bubble size distribution. At radii smaller than the Hinze scale, $N_b(r) \sim r^{-3/2}$ surface tension is important at maintaining bubble integrity and bubbles are stable enough to continue growing by rectified diffusion. Above the Hinze scale, bubbles are unstable and prone to fragmentation due to shear turbulence. As shown by comparing the main and inset panels in Figure 4.27, the slope of the two regions of the bubble size distribution depends upon the time elapsed since the entraining breaking event. Each slope is a bubble loss rate that gives clues as to the wave, ambient environment, and bubble-bubble interaction physics the bubbles experience (Deane and Stokes, 2002). Average bubble size distributions and Hinze scale estimates from the SUSTAIN laboratory experiments are shown in Figure 4.28 below.

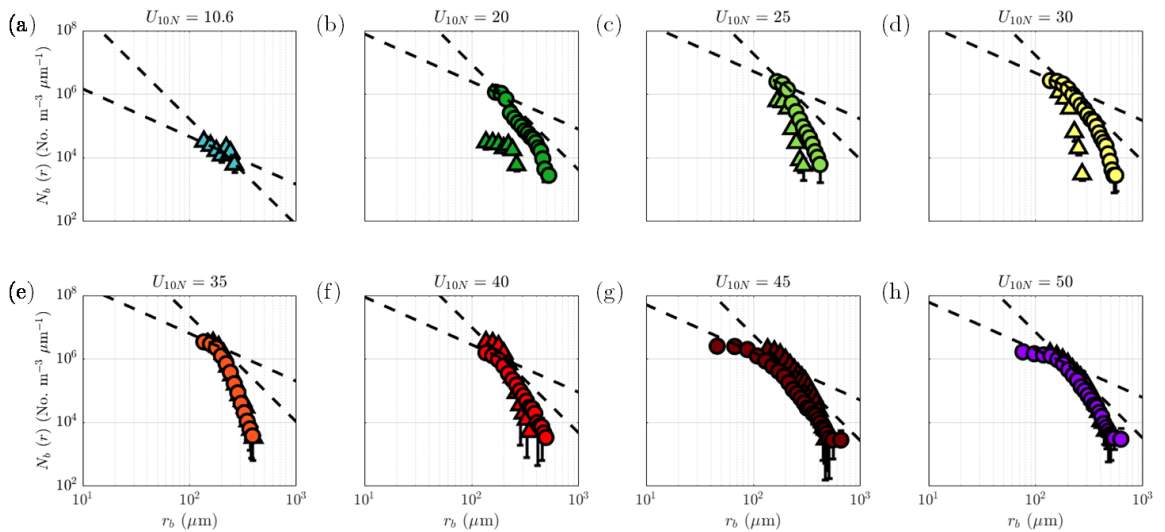


Figure 4.28 Average bubble size distributions $N_b(r)$ from the 10 shadowgraph images from JONSWAP wave spectrum experiments 27-34 (triangles) and monochromatic wave experiments 1-8 (circles). The magenta line is the Hinze scale estimate, and the black dashed lines, c.f. Deane and Stokes (2002), are $r^{-3/2}$ and $r^{-10/3}$. Error bars indicate one standard deviation.

Average bubble size distributions shown in Figure 4.28 show steeper slope with radius for JONSWAP wave spectrum conditions at lower wind speeds, and a decrease in the slope of distributions above the Hinze scale regardless of the wave condition. Deane and Stokes (2002) associate the slope of the bubble size distribution at radii below a_H to jet and drop air entrainment, while the slope at radii greater than a_H is related to collapse of the air cavity of waves in plunging-type breaking. Steeper slopes observed in JONSWAP spectrum conditions at low winds indicate weaker breaking, less air entrainment through cavity collapse and a more rapid bubble loss rate. At higher winds ($U_{10N} \geq 35 \text{ ms}^{-1}$), more frequent breaking and greater sub-surface turbulence result in shallower slope to the bubble size distribution above a_H particularly beneath monochromatic wave conditions, as well as a greater number of small bubbles.

Finally, we use the Hinze scale estimates and connect them with local wave energy \bar{E}_{lw} calculated from surface wave wire data, and the TKE dissipation rate $\bar{\varepsilon}$. We expect a reduction in a_H as greater local wave energy and breaking probability result in larger breaking-induced sub-surface turbulence. More frequent and intense breaking, particularly with air cavity collapse result in greater shear turbulence and larger TKE dissipation rates even at a distance from the air-water interface. Changes in Hinze scale with \bar{E}_{lw} and sub-surface shear production of TKE according to MOST ($u_{*w}^3 \kappa^{-1} z^{-1}$) are shown in Figure 4.29. Additionally, we compare the theoretical and measured dissipation rates from the laboratory and the SWADE field experiment (Drennan, et al. 1996) in Figure 4.29 (c).

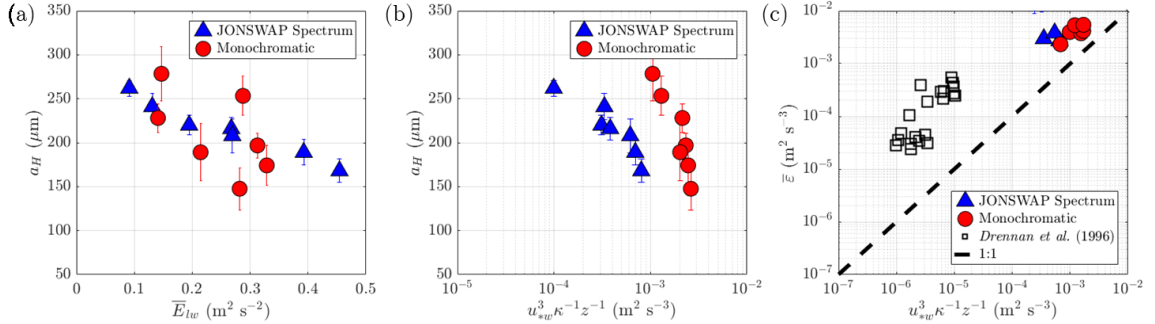


Figure 4.29 Average estimates of the Hinze scale based on bubble size distributions as a function of (a) local wave energy and (b) Monin-Obukhov (wall-layer) theory shear production of TKE in JONSWAP wave spectrum (blue triangles) and monochromatic wave (red circles) conditions. In panel (c), wall-layer shear production of TKE (proxy for dissipation rate in MOST balance) is compared with measured TKE dissipation rates. Data from Drennan et al. (1996) taken during SWADE is included in black squares. The dashed black line is 1:1, where $\varepsilon_{meas} = \varepsilon_{wall} = u_*^3 \kappa^{-1} z^{-1}$.

Where sub-surface velocity spectra permitted quality calculation of TKE dissipation rates, the Hinze scale is seen to decrease with greater local wave energy and higher shear production of TKE. More intense and frequent breaking, resulting in greater sub-surface wave-induced and shear turbulence reduce the size bubbles can attain by growth before turbulent fragmentation. TKE dissipation rates calculated from sub-surface velocity spectra are found to be larger than wall-layer theory in both field and laboratory studies by $O(10^1 - 10^2)$ and $O(2 - 4 \times 10^0)$, respectively.

4.5 Summary

Laboratory experiments focusing on bubble dynamics and air-sea gas transfer conducted in the SUSTAIN wind-wave tank involved simultaneous and approximately co-located measurements of surface waves, sub-surface turbulence, and bubbles entrained by jet, drop, and air-cavity collapse wave breaking events. Monochromatic and JONSWAP spectrum waves were shown to respond differently to the same wind conditions, with the

latter increasing in wavenumber and height gradually and a slower increase in wave spectral density. Significant wave heights were also larger in monochromatic conditions.

Statistics of the probability and intensity that prescribed wind-wave conditions resulted in breaking demonstrated an increased likelihood occurs above $U_{10N} = 30 \text{ ms}^{-1}$ and the percentage of crests that break is larger in the monochromatic waves and increases with a logistic shape in the JONSWAP spectrum wave conditions. Local wave energy associated with breaking wave crests generally increases linearly with the wind stress, which is found to be larger in JONSWAP spectrum conditions for high winds $U_{10N} \geq 40 \text{ ms}^{-1}$.

Bubble size distributions observed with an underwater enclosed camera system were parameterized in terms of observed wind-wave turbulence as described by the wind-wave Reynolds number. This proxy includes friction velocity, significant wave height, and water viscosity, to account for the roughness of the surface and height of surface waves in the context of wave breaking. The density and viscosity of the water environment resist air entrainment through buoyancy and surface tension effects. Bubble size distributions were parameterized using a lognormal distribution with wind-wave Reynolds number as the only parameter. Normalized bubble size distributions from various field, numerical, and laboratory studies over the past several decades were fitted to lognormal distributions as a diagnostic and literature supports lognormal fits as appropriate to describe bubble populations.

Bubble statistics including total entrained volume, number, and bubble size were evaluated in terms of wind-wave Reynolds number. Total entrained bubble volume and number of bubbles were found to increase in both wave conditions, whereas the average radius decreased. A decrease in entrained volume, stagnation in number, and steep decrease

in bubble radius were observed at high wind-wave Reynolds number and are associated with reduced roughness and somewhat smaller significant wave heights in monochromatic breaking waves at these high winds. Visual inspection of bubble images clearly shows the progression of bubble behavior from discrete and separated, to occasionally clustered, and finally saturated or heavily clustered groups of bubbles.

Linear fits between amplitude, mean, and variance of the lognormal fits to bubble size distributions were made in terms of wind-wave Reynolds number. A decrease in amplitude a and mean μ , with an increase in bubble size variance σ were observed. Pearson correlation coefficients between parameterized and actual values for each of these terms exceeded 0.90. Probability distribution functions $P(r)$ constructed using the parameterized distributions were compared to the actual bubble size distributions, and show good agreement where sufficient bubble objects and scattering of light provided quality images for bubble statistics to be collected. A decrease in amplitude and mean radius and increase in variance of the bubbles was clearly seen in the PDFs in both JONSWAP spectrum and monochromatic wave conditions.

To connect the waves and bubbles to sub-surface turbulence, we calculated the wave-scaled TKE dissipation rate $\varepsilon H_{sig} F^{-1}$ based on two sets of field experiments (Drennan et al. 1996; Terray et al. 1996). Wavelet directional method (WDM; Donelan, et al. 1996) and the wave growth rate functions (Donelan and Plant, 2009) were used to determine the energy input from wind to waves F . Wave growth rate was found to be similar at low winds for both monochromatic and JONSWAP wave conditions, but be noticeably larger in monochromatic wave conditions at high winds. The largest growth rates were observed within $\pm 30^\circ$ of the wind direction.

Directional wave spectra were compared between the two wave conditions, and present with broader wavenumber extent in the wave energy in JONSWAP spectrum wave conditions, while the monochromatic wave spectra extended to greater angles outward from the wind direction at high winds but otherwise were similar. Significant wave heights calculated using water surface elevation data from wave wires agreed very well with manual calculation using the zeroth statistical moment determined from the WDM results.

Energy input values were compared with those from SWADE (Drennan, et al. 1996) and are shown to increase with the inverse wave age $u_* c_p^{-1}$. The datasets were plotted on logarithmic-logarithmic axes and fitted to power law lines, with the laboratory JONSWAP spectrum data being roughly collinear with the higher peak-frequency, lower significant wave height subset of the SWADE data. Monochromatic laboratory data was collinear with the higher wave height, lower-frequency more swell-like waves from SWADE. Disagreement to the fits was observed for lower wind conditions and was believed to be the result of lower wind stress and significant wave height (weaker wave spectral density) than would be expected for real open ocean conditions.

Sub-surface velocity and derived turbulence data were gathered using a Vectrino II 3D-ADCP for a 0.03-meter vertical profile about 0.30 meters below the air sea interface near-fetch to the bubble imager and wave wire array. Water-side average velocity and friction velocity increase universally in JONSWAP spectrum wave conditions and for $U_{10N} < 40 \text{ ms}^{-1}$, and then decrease slightly in monochromatic wave conditions. Each behavior is consistent with the average signal-to-noise ratio (SNR), which we noted was lower than recommended guidelines in experiments with $U_{10N} \leq 30$ and $U_{10N} \leq 20$ in JONSWAP spectrum and monochromatic wave conditions, respectively.

Velocity data were decomposed into mean, wave, turbulent, and noise components using water-surface elevation data from wave wires, and the turbulent spectra from sub-surface measurements were processed using a newly-developed algorithm for robustly identifying the inertial subrange (ARIIS; Ortiz-Suslow, et al. 2019). Inertial subranges were identified following a test for isotropy. Spectral slopes and wave band location in each experiment show poor identification at low wind speeds, particularly in the JONSWAP spectrum wave conditions where SNR was poor.

Wave-scaled dissipation rates were constructed using these calculated TKE dissipation rates and found to follow the power law fit $\varepsilon H_{sig} F^{-1} \approx 0.15(zH_{sig}^{-1})^{-2}$ whereas data from SWADE followed a fit $\varepsilon H_{sig} F^{-1} \approx 0.75(zH_{sig}^{-1})^{-2}$ shifted to the right of laboratory data due to differences in significant wave height. Energy input from wind to waves F was then linked to observed average SNR and TKE dissipation rates from both field and laboratory data. Larger momentum flux and waves of smaller age resulted in greater frequency and intensity of breaking, subsequent sub-surface SNR, and larger dissipation rates.

Lastly, the bubble Hinze scale, a metric for relating bubble size to surface tension and turbulent shear forces the bubbles are subjected to, was estimated for the bubble size distributions and compared with local wave energy of breaking waves and measured sub-surface TKE dissipation rates. The Hinze scale, or maximum size a bubble can attain prior to turbulent fragmentation, is shown to decrease with increasing local breaking wave energy, shear production of TKE, which yield higher TKE dissipation rates.

Chapter 5: Conclusions

In this dissertation, we used data and observations from a multi-faceted open ocean field campaign and a series of cross-disciplinary laboratory wind-wave tank experiments to gain further understanding as to the integral and complex role of the evolving structure of the sea surface on energy budgets and energy transfer. Specifically, we focused on turbulent kinetic energy and its dissipation in the atmospheric and ocean surface layers adjacent to the air-water interface. From the multi-day LAgrangian Submesoscale ExpeRiment (LASER) cruise data, we were able to link turbulent kinetic energy production and dissipation rates from atmospheric surface layers to wave age and atmospheric stability in a variety of wind and wave conditions. Furthermore, we were able to compare TKE dissipation rates with moderate to high wind hurricane boundary layer (HBL) aircraft data from the CBLAST campaign (Zhang, 2010). Laboratory experiments designed to investigate bubble dynamics and air-sea gas transfer at high winds provided data for directly connecting wave statistics and breaking waves in up to hurricane-force winds to sub-surface turbulence, dissipation, and the production of bubbles. Herein, we present conclusions based on detailed analysis of data from these field and laboratory studies:

- (1) Local rate of change and dissipation rate of turbulent kinetic energy increase with wind stress and where the air-water temperature disequilibrium favors positive heat fluxes. Sea conditions during LASER were predominantly windsea and over deep water, while swells were observed in lower winds. Momentum and heat fluxes were larger in windsea conditions, and these eddy fluxes act to produce TKE by working against the mean velocity profile and stratification in the atmospheric surface layer.

(2) TKE dissipation rates measured in non-hurricane ASL and hurricane boundary layer environments increase with the air-sea drag coefficient and agree better when $C_{D10N} = u_*^2 U_{10N}^{-2}$ is used as a proxy in place of wind speed alone regardless of differences in the height at which the measurements were taken. This is exclusive to windsea conditions where waves respond to local wind stress. We assert that using the drag coefficient accounts for the local eddy momentum flux relative to the magnitude of the mean wind profile $\partial \bar{U} / \partial z^{-1}$ which becomes increasingly larger as u_* increases. Therefore, drag coefficient describes the efficiency of shear production of TKE and thus the dissipation rate.

(3) Dissipation of turbulence in the ASL results in a portion of the energy being transferred as heat internal to the surface layer, which while typically taking small values relative to bulk sensible and latent heat can be large in near-neutral atmospheric stability. This dissipative heat flux or dissipative heating should be calculated using the TKE dissipation rate itself, as has been found to be overestimated using the cube of wind speed. The ratio of dissipative to bulk heat fluxes is largest (typically 5-15 percent) when shear production of TKE is large and buoyancy production of TKE is small.

(4) Sea surface roughness parameterized with the Charnock roughness length (Charnock, 1955), inverse wave age (Drennan et al. 2003), and significant wave steepness (Taylor and Yelland, 2001) was larger in windsea than swell. Inverse wave age parameterized roughness in windsea more accurately, whereas significant steepness parameterized roughness better in swell as discussed by Drennan et al. (2005). TKE dissipation rates increase with sea surface roughness, which is itself larger in windsea. This

reaffirms the importance of momentum flux to turbulence and shear production as often the dominant production term in the ASL.

(5) Shear production was the dominant TKE production term in the LASER (2016) measurements and large in windsea where atmospheric stability was near-neutral. Buoyancy production, turbulent transport, and pressure work were more influential to the TKE budget in unstable ASLs where the seas were swell-dominated and winds were light.

(6) TKE dissipation rate can be parameterized following Yelland and Taylor (1996) and Ortiz-Suslow et al. (2020) using shear production of TKE and atmospheric stability. Parameterized and measured dissipation rates agree well in windsea, where wave age is small and Monin-Obukhov theory is valid. Disagreement is strongest in swell conditions. TKE dissipation rates can also be parameterized in terms of the aerodynamic drag coefficient, however units are inconsistent. Nevertheless, TKE dissipation rates are physically constrained by the local eddy momentum flux magnitude relative to the ambient vertical wind profile – which is not conveyed by wind speed alone.

(7) Laboratory waves modelled after the JONSWAP wave spectrum (Hasselmann et al. 1973) rather than using a monochromatic wave of arbitrary frequency produced gradually increasing wave energy spectra , decreasing wave frequency and wavenumber with increased wind stress. Monochromatic waves by comparison receive momentum flux from the overlying wind to a single frequency, have wave spectra that respond less noticeably to increasing wind stress, and wave statistics with much less variance.

(8) Wave breaking occurs more frequently and with greater intensity for the monochromatic waves, the probability of breaking increasing most rapidly between $U_{10N} = 25 - 30 \text{ ms}^{-1}$. Wind stress and local wave energy however are larger in JONSWAP

spectrum wave conditions for high winds ($U_{10N} \geq 40 \text{ ms}^{-1}$), indicating that these waves continue to roughen and steepen without the wave collapse seen with plunging breakers.

(9) Bubble size distributions from field, numerical, and laboratory studies can be parameterized using the lognormal distribution, which includes a low-radius peak and high-radius tail taking positive values everywhere and has been shown appropriate to model bubble populations (Riquelme, et al. 2013).

(10) Total integrated bubble volume, number and size of bubbles can each be expressed in terms of non-dimensional turbulence numbers such as the wind-wave Reynolds number. Increasing wind stress and wave height results in greater air volume entrainment and a greater number of bubbles. Air entrainment is greater in the more frequently and intensely breaking monochromatic wave conditions. Bubble size however, decreases as the turbulence number increases. Large bubbles buoyantly degas or are fragmented by sub-surface turbulent shear instigated by the wave breaking events. Bubble distribution as seen in raw images progress from separate, to occasionally clustered, to saturated and frequently clustered at high wind-wave Reynolds number.

(11) Amplitude, mean, and variance parameters used to construct lognormal distributions parameterize the bubble size distributions well. Amplitude (probability of bubbles at the peak of the distribution) and average bubble size decrease with wind-wave Reynolds number whereas the variety of bubble sizes indicated by the variance, increases with wind-wave Reynolds number. The resulting bubble size distributions thus become more broad and more negatively skewed with increasing surface roughness and breaking waves of greater height.

(12) Wave growth rate and directional wave spectra indicate a higher average

growth rate and larger integrated wave energy in monochromatic waves as shown by significant wave height, particularly in hurricane force winds and greater. JONSWAP spectrum waves are broad-banded in angular wave frequency, whereas monochromatic waves have greater directional spread as wind speed increases. The projection of wave growth rate across the directional wave spectra show expected peaks near the prescribed 1.00 Hz wave frequency but greater magnitude in monochromatic wave cases.

(13) Energy input from wind to waves is larger in monochromatic waves, increasing with inverse wave age $u_* c_p^{-1}$, and laboratory data follow power law fits that agree with two groups of data from the SWADE field campaign (Drennan et al. 1996). Disagreement between the laboratory data and these fits occurs in lower wind speed conditions regardless of wave type and the magnitude of wave energies in the directional wave spectra for such cases are also relatively weak. We surmise reduced roughness and/or unrealistic steepness given that these are paddle generated waves may contribute to this observation.

(14) Sub-surface velocity, stress, and ADCP signal to noise ratio (SNR) are each larger in monochromatic than JONSWAP spectrum wave conditions, owing to increased probability and intensity of wave breaking. Signal to noise ratio is weak in the low-wind conditions, particularly for JONSWAP spectrum waves, as a direct consequence of the smaller wave heights and less vigorous breaking events resulting in fewer sub-surface scatterers (e.g. bubbles).

(15) Velocity spectra allow for calculation of TKE dissipation rates only for moderate to high wind speeds, where surface wave breaking yields sufficient SNR to identify an inertial sub-range at higher frequencies than the wave band. Inertial sub-range

frequency bands are larger in monochromatic than JONSWAP spectrum wave conditions, and TKE dissipation rates are expected to be larger beneath the monochromatic waves.

(16) Wave-scaled TKE dissipation rates in laboratory and field data from SWADE (Drennan et al. 1996) and WAVES (Terray et al. 1996) follow power law fits with wave-scaled depth. Significant wave heights in the three datasets segregate out the fits and determine the scaling coefficient. Wave-scaled dissipation rates are larger in monochromatic wave conditions, and increase towards smaller wave-scaled depth where ADCP SNR was sufficient to yield quality turbulence data.

(17) TKE dissipation rate increases with energy input from the wind (momentum flux to waves) in conjunction with higher SNR values in the laboratory measurements. Field data affirm that higher significant wave heights and lower wave age result in greater local sub-surface shear turbulence associated with multi-scale wave breaking events.

(18) With increasing wind stress, wave breaking, and sub-surface turbulence, fewer large bubbles remain either due to buoyant outgassing, horizontal advection, or fragmentation due to shear turbulence. A greater number of small bubbles is observed, particularly in monochromatic wave conditions and the bubble size distribution slope at high radii decreases as a result.

(19) Large bubbles become harder to maintain below the air-water interface in higher wind and rougher conditions as more frequent breaking occurs. Hinze scale estimates decrease with greater local breaking wave energy and as sub-surface TKE dissipation rates increase. Both field and laboratory TKE dissipation rates exceed wall-layer theory values, with greater exceedance in field data potentially a consequence of

higher significant wave heights, smaller water-side stress and/or lower peak frequency of the open ocean waves

REFERENCES

- Abbas, S., Hayat, K., Karangwa, E., Bashari, M., & Zhang, X. (2013). An overview of ultrasound-assisted food-grade nanoemulsions. *Food Engineering Reviews*, 5(3), 139–157. <https://doi.org/10.1007/s12393-013-9066-3>
- Agrawal, Y. C., Terray, E. A., Donelan, M. A., Hwang, P. A., Williams, A. J., Drennan, W. M., ... Kitaigorodskii, S. A. (1992). Enhanced dissipation of kinetic energy beneath surface waves. *Nature*, 359(6392), 219–220. <https://doi.org/10.1038/359219a0>
- Arsenyev, S. A., Dorbrooklonsky, S. V., Mamedov, R. M., & Shelkovnikov, N. K. (1975). Direct measurements of some characteristics of fine structure from a stationary platform in the open sea. *Fizika Atmosphery i Okeana*, 11, 845–850.
- Atherton, T. J., & Kerbyson, D. J. (1993). The coherent circle Hough transform. *Proceedings of the 4th British Machine Vision Conference*, 269–278. <https://doi.org/10.5244/c.7.27>
- Atherton, T. J., & Kerbyson, D. J. (1999). Size invariant circle detection. *Image and Vision Computing*, 17(11), 795–803. [https://doi.org/10.1016/S0262-8856\(98\)00160-7](https://doi.org/10.1016/S0262-8856(98)00160-7)
- Babanin, A., Chalikov, D., Young, I., & Savelyev, I. (2007). Predicting the breaking onset of surface water waves. *Geophysical Research Letters*, 34(7), 1–6. <https://doi.org/10.1029/2006GL029135>
- Banner, M. L., Barthelemy, X., Fedele, F., Allis, M., Benetazzo, A., Dias, F., & Peirson, W. L. (2014). Linking reduced breaking crest speeds to unsteady nonlinear water wave group behavior. *Physical Review Letters*, 112(11), 1–5. <https://doi.org/10.1103/PhysRevLett.112.114502>
- Banner, M. L., & Peregrine, D. H. (1993). Wave breaking in deep water. *Annual Review of Fluid Mechanics*, 25, 373–397.
- Benilov, A. Y., & Filyushkin, B. N. (1970). Application of methods of linear filtration to an analysis of fluctuations in the surface layer of the sea. *Izv. Atmos. Oceanic Phys.*, 6, 810–819.
- Blanchard, D. C., & Woodcock, A. H. (1957). Bubble formation and modification in the sea and its meteorological significance. *Tellus*, 9(2), 145–158.
- Boettcher, E. J., Fineberg, J., & Lathrop, D. P. (2000). Turbulence and wave breaking effects on air-water gas exchange. *Physical Review Letters*, 85(9), 2030–2033. <https://doi.org/10.1103/PhysRevLett.85.2030>

- Bricker, J. D., & Monismith, S. G. (2007). Spectral wave-turbulence decomposition. *Journal of Atmospheric and Oceanic Technology*, 24(8), 1479–1487. <https://doi.org/10.1175/JTECH2066.1>
- Brumer, S. E., Zappa, C. J., Blomquist, B. W., Fairall, C. W., Cifuentes-Lorenzen, A., Edson, J. B., ... Huebert, B. J. (2017). Wave-related Reynolds number parameterizations of CO₂ and DMS transfer velocities. *Geophysical Research Letters*, 44(19), 9865–9875. <https://doi.org/10.1002/2017GL074979>
- Brumer, S. E., Zappa, C. J., Brooks, I. M., Tamura, H., Brown, S. M., Blomquist, B. W., ... Cifuentes-Lorenzen, A. (2017). Whitecap coverage dependence on wind and wave statistics as observed during SO GasEx and HiWinGS. *Journal of Physical Oceanography*, 47(9), 2211–2235. <https://doi.org/10.1175/JPO-D-17-0005.1>
- Cai, Y., Wen, Y., Wu, L., Zhou, C., & Zhang, F. (2017). Impact of wave breaking on upper-ocean turbulence. *Journal of Geophysical Research: Oceans*, 122(2), 1513–1528. <https://doi.org/10.1002/2016JC012654>
- Callaghan, A. H., Stokes, M. D., & Deane, G. B. (2014). The effect of water temperature on air entrainment, bubble plumes, and surface foam in a laboratory breaking-wave analog. *Journal of Geophysical Research: Oceans*. <https://doi.org/10.1002/2014JC010351>
- Collins, C. O., Blomquist, B., Persson, O., Lund, B., Rogers, W. E., Thomson, J., ... Graber, H. C. (2017). Doppler correction of wave frequency spectra measured by underway vessels. *Journal of Atmospheric and Oceanic Technology*, 34(2), 429–436. <https://doi.org/10.1175/jtech-d-16-0138.1>
- D'Asaro, E., & McNeil, C. (2008). Air-sea gas exchange at extreme wind speeds measured by autonomous oceanographic floats (DOI:10.1016/j.jmarsys.2006.06.007). *Journal of Marine Systems*, 74(1–2), 722–736. <https://doi.org/10.1016/j.jmarsys.2008.02.006>
- Deane, G. B. (1997). Sound generation and air entrainment by breaking waves in the surf zone. *The Journal of the Acoustical Society of America*, 102(5), 2671–2689. <https://doi.org/10.1121/1.420321>
- Deane, G. B., & Stokes, M. D. (1999). Air entrainment processes and bubble size distributions in the surf zone. *Journal of Physical Oceanography*, 29(7), 1393–1403. [https://doi.org/10.1175/1520-0485\(1999\)029<1393:aepabs>2.0.co;2](https://doi.org/10.1175/1520-0485(1999)029<1393:aepabs>2.0.co;2)
- Deane, G. B., & Stokes, M. D. (2002). Scale dependence of bubble creation mechanisms in breaking waves. *Nature*, 418(6900), 839–844. <https://doi.org/10.1038/nature00967>

- Deane, G. B., Stokes, M. D., & Callaghan, A. H. (2016). The saturation of fluid turbulence in breaking laboratory waves and implications for whitecaps. *Journal of Physical Oceanography*, 46(3), 975–992. <https://doi.org/10.1175/JPO-D-14-0187.1>
- Derakhti, M., & Kirby, J. T. (2016). Breaking-onset, energy and momentum flux in unsteady focused wave packets. *Journal of Fluid Mechanics*. <https://doi.org/10.1017/jfm.2016.17>
- Derakhti, M., & Kirby, J. T. (2014). Bubble entrainment and liquid-bubble interaction under unsteady breaking waves. *Journal of Fluid Mechanics*, 761, 464–506. <https://doi.org/10.1017/jfm.2014.637>
- Donelan, M. A., Drennan, W. M., & Magnusson, A. K. (1996). Nonstationary analysis of the directional properties of propagating waves. *Journal of Physical Oceanography*, 26(9), 1901–1914. [https://doi.org/10.1175/1520-0485\(1996\)026<1901:NAOTDP>2.0.CO;2](https://doi.org/10.1175/1520-0485(1996)026<1901:NAOTDP>2.0.CO;2)
- Donelan, M. A., & Plant, W. J. (2009). A threshold for wind-wave growth. *Journal of Geophysical Research: Oceans*, 114(7), 1–8. <https://doi.org/10.1029/2008JC005238>
- Drennan, W. M., Donelan, M. A., Terray, E. A., & Katsaros, K. B. (1996). Oceanic turbulence dissipation measurements in SWADE. *Journal of Physical Oceanography*, 26(5), 808–815. [https://doi.org/10.1175/1520-0485\(1996\)026<0808:OTDMIS>2.0.CO;2](https://doi.org/10.1175/1520-0485(1996)026<0808:OTDMIS>2.0.CO;2)
- Drennan, W. M., Donelan, M. A., Madsen, N., Katsaros, K. B., Terray, E. A., & Flagg, C. N. (1994). Directional wave spectra from a SWATH ship at sea. *Journal of Atmospheric and Ocean Tech*, 11.
- Drennan, W. M., Kahma, K. K., & Donelan, M. A. (1999). On momentum flux and velocity spectra over waves. *Boundary-Layer Meteorology*, 92(3), 489–515. <https://doi.org/10.1023/A:1002054820455>
- Edson, J. B., & Fairall, C. W. (1998). Similarity relationships in the marine atmospheric surface layer for terms in the TKE and scalar variance budgets. *Journal of the Atmospheric Sciences*, 55(13), 2311–2328. [https://doi.org/10.1175/1520-0469\(1998\)055<2311:SRITMA>2.0.CO;2](https://doi.org/10.1175/1520-0469(1998)055<2311:SRITMA>2.0.CO;2)
- Egan, G., Cowherd, M., Fringer, O., & Monismith, S. (2019). Observations of near-bed shear stress in a shallow, wave- and current-driven flow. *Journal of Geophysical Research: Oceans*, 124(8), 6323–6344. <https://doi.org/10.1029/2019JC015165>
- Elsayed, M. A. K. (2008). Application of continuous wavelet analysis in distinguishing breaking and nonbreaking waves in the wind-wave time series. *Journal of Coastal Research*, 24(1), 273–277. <https://doi.org/10.2112/05-0443.1>

- Fairall, C. W., & Larsen, S. E. (1986). Inertial-dissipation methods and turbulent fluxes at the air-ocean interface. *Boundary-Layer Meteorology*, 34(3), 287–301.
<https://doi.org/10.1007/BF00122383>
- Farmer, D. M., McNeil, C. L., & Johnson, B. D. (1993). Evidence for the importance of bubbles in increasing air-sea gas flux. *Nature*, 361, 620–623.
<https://doi.org/10.1017/CBO9781107415324.004>
- Foken, T., & Wichura, B. (1996). Tools for quality assessment of surface-based flux measurements. *Agricultural and Forest Meteorology*, 78(1–2), 83–105.
[https://doi.org/10.1016/0168-1923\(95\)02248-1](https://doi.org/10.1016/0168-1923(95)02248-1)
- Friebel, H. C., Herrington, T. O., & Benilov, A. Y. (2009). Evaluation of the flow distortion around the Campbell Scientific CSAT3 sonic anemometer relative to incident wind direction. *Journal of Atmospheric and Oceanic Technology*, 26(3), 582–592. <https://doi.org/10.1175/2008JTECHO550.1>
- Galchenko, A., Babanin, A. V., Chalikov, D., Young, I. R., & Haus, B. K. (2012). Influence of wind forcing on modulation and breaking of one-dimensional deep-water wave groups. *Journal of Physical Oceanography*, 42(6), 928–939.
<https://doi.org/10.1175/JPO-D-11-083.1>
- Gargett, A. (1989). Ocean Turbulence. *Annual Review of Fluid Mechanics*, 21(1), 419–451. <https://doi.org/10.1146/annurev.fluid.21.1.419>
- Garrett, C., Li, M., & Farmer, D. (2000). The connection between bubble size spectra and energy dissipation rates in the upper ocean. *Journal of Physical Oceanography*, 30(9), 2163–2171. [https://doi.org/10.1175/1520-0485\(2000\)030<2163:TCBBSS>2.0.CO;2](https://doi.org/10.1175/1520-0485(2000)030<2163:TCBBSS>2.0.CO;2)
- Gemmrich, J. (2010). Breaking waves and near-surface turbulence. In *Encyclopedia of Ocean Sciences* (pp. 431–438). <https://doi.org/10.1016/B978-012374473-9.00641-X>
- Gemmrich, J. R., & Farmer, D. M. (1999). Near-surface turbulence and thermal structure in a wind-driven sea. *Journal of Physical Oceanography*, 29(3), 480–499.
[https://doi.org/10.1175/1520-0485\(1999\)029<0480:NSTATS>2.0.CO;2](https://doi.org/10.1175/1520-0485(1999)029<0480:NSTATS>2.0.CO;2)
- Gemmrich, J. R., & Farmer, D. M. (1999). Observations of the scale and occurrence of breaking surface waves. *Journal of Physical Oceanography*, 29(10), 2595–2606.
[https://doi.org/10.1175/1520-0485\(1999\)029<2595:OOTSAO>2.0.CO;2](https://doi.org/10.1175/1520-0485(1999)029<2595:OOTSAO>2.0.CO;2)
- Gemmrich, J. R., & Farmer, D. M. (2004). Near-surface turbulence in the presence of breaking waves. *Journal of Physical Oceanography*, 34(5), 1067–1086.
[https://doi.org/10.1175/1520-0485\(2004\)034<1067:NTITPO>2.0.CO;2](https://doi.org/10.1175/1520-0485(2004)034<1067:NTITPO>2.0.CO;2)

- Gerbi, G. P., Trowbridge, J. H., Terray, E. A., Plueddemann, A. J., & Kukulka, T. (2009). Observations of turbulence in the ocean surface boundary layer: Energetics and transport. *Journal of Physical Oceanography*, 39(5), 1077–1096. <https://doi.org/10.1175/2008JPO4044.1>
- Goddijn-Murphy, L., Woolf, D. K., & Callaghan, A. H. (2011). Parameterizations and algorithms for oceanic whitecap coverage. *Journal of Physical Oceanography*, 41(4), 742–756. <https://doi.org/10.1175/2010JPO4533.1>
- Goring, D. G., & Nikora, V. I. (2002). Despiking acoustic Doppler velocimeter data. *Journal of Hydraulic Engineering*, 117–126.
- Hasselmann, K., Barnett, T. P., Bouws, E., Carlson, H., Cartwright, D. E., Eake, K., ... Walden, H. (1973). Measurements of wind-wave growth and swell decay during the joint North Sea wave project (JONSWAP). *Supplement to the German Hydrographic Journal*, 12(1), 10–90.
- Hinze, J. O. (1955). Fundamentals of the hydrodynamic mechanism of splitting in dispersion processes. *AICHE Journal*, 1(3), 289–295. <https://doi.org/10.1002/aic.690010303>
- Holthuijsen, L. H., & Herbers, T. H. C. (1986). Statistics of breaking waves observed as whitecaps in the open sea. *Journal of Physical Oceanography*, Vol. 16, pp. 290–297. [https://doi.org/10.1175/1520-0485\(1986\)016<0290:sobwoa>2.0.co;2](https://doi.org/10.1175/1520-0485(1986)016<0290:sobwoa>2.0.co;2)
- Huang, N. E., Long, S. R., Donelan, M. A., Yuan, Y., & Lai, Ronald, J. (1992). The local properties of ocean surface waves by the phase-time method. *Geophysical Research Letters*, 19(7), 685–688.
- Hwang, P. A., Poon, Y.-K., & Wu, J. (1991). Temperature effects on generation and entrainment of bubbles induced by a water jet. *Journal of Physical Oceanography*, Vol. 21, pp. 1602–1605. [https://doi.org/10.1175/1520-0485\(1991\)021<1602:teogae>2.0.co;2](https://doi.org/10.1175/1520-0485(1991)021<1602:teogae>2.0.co;2)
- Hwang, P. A., Xu, D., & Wu, J. (1989). Breaking of wind-generated waves: Measurements and characteristics. *Journal of Fluid Mechanics*, 202(5), 177–200. <https://doi.org/10.1017/S002211208900114X>
- Jeong, D., Haus, B. K., & Donelan, M. A. (2012). Enthalpy transfer across the air–water interface in high winds including spray. *Journal of the Atmospheric Sciences*, 69(9), 2733–2748. <https://doi.org/10.1175/JAS-D-11-0260.1>
- Jimenez, J., Wray, A. A., Saffman, P. G., & Rogallo, R. S. (1993). The structure of intense vorticity in isotropic turbulence. *Journal of Fluid Mechanics*, 255, 65–90. <https://doi.org/10.1017/S0022112093002393>

- Johnson, B. D., & Cooke, R. C. (1979). Bubble populations and spectra in coastal waters: a photographic approach. *Journal of Geophysical Research*, 84(C7), 3761. <https://doi.org/10.1029/jc084ic07p03761>
- Kanwisher, J. (1963). On the exchange of gases between the atmosphere and the sea. *Deep-Sea Research and Oceanographic Abstracts*, 10(3), 195–207. [https://doi.org/10.1016/0011-7471\(63\)90356-5](https://doi.org/10.1016/0011-7471(63)90356-5)
- Keeling, R. F. (1993). On the role of large bubbles in air-sea gas exchange and supersaturation in the ocean. *Journal of Marine Research*, 51(2), 237–271. <https://doi.org/10.1357/0022240933223800>
- Kendall Melville, W. (1994). Energy dissipation by breaking waves. *Journal of Physical Oceanography*, 24(10), 2041–2049. [https://doi.org/10.1175/1520-0485\(1994\)024<2041:EDBBW>2.0.CO;2](https://doi.org/10.1175/1520-0485(1994)024<2041:EDBBW>2.0.CO;2)
- Kinsman, B. (1965). *Wind waves, their generation and propagation on the ocean surface*. Englewood Cliffs, N.J.: Prentice Hall.
- Kitaigorodskii, S. A., Donelan, M. A., Lumley, J. L., & Terray, E. A. (1983). Wave-turbulence interactions in the upper ocean. Part II. Statistical characteristics of wave and turbulent components of the random velocity field in the marine surface layer. *Journal of Physical Oceanography*, 13(11), 1988–1999. [https://doi.org/10.1175/1520-0485\(1983\)013<1988:WTIITU>2.0.CO;2](https://doi.org/10.1175/1520-0485(1983)013<1988:WTIITU>2.0.CO;2)
- Koga, M. (1982). Bubble entrainment in breaking wind waves. *Tellus*, 34(5), 481–489. <https://doi.org/10.3402/tellusa.v34i5.10833>
- Kolmogorov, A. N. (1941). The local structure of turbulence in incompressible viscous fluid for very large Reynolds numbers. *Proceedings of the Royal Society A: Mathematical, Physical and Engineering Sciences*, Vol. 434, pp. 9–13. <https://doi.org/10.1098/rspa.1991.0075>
- Krall, K. E., Smith, A. W., Takagaki, N., & Jähne, B. (2019). Air – sea gas exchange at wind speeds up to 85 m s⁻¹. *Ocean Science*, 15, 1783–1799.
- Lamarre, E., & Melville, W. K. (1991). Air entrainment and dissipation in breaking waves. *Nature*, 351, 469–472.
- Lance, M., & Bataille, J. (1991). Turbulence in the liquid phase of a uniform bubbly air-water flow. *Journal of Fluid Mechanics*, 222, 95–118.
- Large, W. G., & Pond, S. (1981). Open ocean momentum flux measurements in moderate to strong winds. *Journal of Physical Oceanography*, Vol. 11, pp. 324–336. [https://doi.org/10.1175/1520-0485\(1981\)011<0324:OOMFMI>2.0.CO;2](https://doi.org/10.1175/1520-0485(1981)011<0324:OOMFMI>2.0.CO;2)

- Laxague, N. J. M., Haus, B. K., Ortiz-Suslow, D. G., Smith, C. J., Novelli, G., Dai, H., ... Gruber, H. C. (2017). Passive optical sensing of the near-surface wind-driven current profile. *Journal of Atmospheric and Oceanic Technology*, 34(5), 1097–1111. <https://doi.org/10.1175/JTECH-D-16-0090.1>
- Lelouvetel, J., Tanaka, T., Sato, Y., & Hishida, K. (2014). Transport mechanisms of the turbulent energy cascade in upward/downward bubbly flows. *Journal of Fluid Mechanics*. <https://doi.org/10.1017/jfm.2014.24>
- Leong, T., Wu, S., Kentish, S., & Ashokkumar, M. (2010). Growth of bubbles by rectified diffusion in aqueous surfactant solutions. *Journal of Physical Chemistry C*, 114(47), 20141–20145. <https://doi.org/10.1021/jp107731j>
- Lewis, E. R., & Schwartz, S. E. (2004). *Sea salt aerosol production: mechanisms, methods, measurements and models - a critical review*.
- Liberzon, D., Vreme, A., Knobler, S., & Bentwich, I. (2019). Detection of breaking waves in single wave gauge records of surface elevation fluctuations. *Journal of Atmospheric and Oceanic Technology*, 36(9), 1863–1879. <https://doi.org/10.1175/JTECH-D-19-0011.1>
- Liu, P. C. (1985). Chapter 78 What Is the Slope of Equilibrium Range. (629), 1045–1057.
- Liu, P. (1993). Estimating breaking wave statistics from wind-wave time series data. *Annales Geophysicae*, 11(10), 970–972.
- Longuet-Higgins, M. S. (1974). Breaking waves in deep or shallow water. *Proceedings of the 10th Conference on Naval Hydrodynamics*, 597–605.
- Marple, S. L. (1999). Computing the discrete-time “analytic” signal via FFT. *IEEE Transactions on Signal Processing*, 47(9), 2849. <https://doi.org/10.1109/acssc.1997.679118>
- Mazzitelli, I. M., & Lohse, D. (2009). Evolution of energy in flow driven by rising bubbles. *Physical Review E - Statistical, Nonlinear, and Soft Matter Physics*, 79(6), 1–9. <https://doi.org/10.1103/PhysRevE.79.066317>
- Medwin, H. (1970). In-situ acoustic measurements of bubble populations in coastal ocean waters. *J Geophys Res*, 75(3), 599–611.
- Medwin, H. (1977). In-situ acoustic measurements of microbubbles at sea. *Journal of Geophysical Research*, 82(6), 971–976.

- Melville, W. K. (1996). The role of surface-wave breaking in air-sea interaction. *Annual Review of Fluid Mechanics*, 28(1), 279–321.
<https://doi.org/10.1146/annurev.fl.28.010196.001431>
- Melville, W. K., Veron, F., & White, C. J. (2002). The velocity field under breaking waves: Coherent structures and turbulence. *Journal of Fluid Mechanics*, 454, 203–233. <https://doi.org/10.1017/S0022112001007078>
- Monin, A. S., & Obukhov, A. M. (1954). Basic laws of turbulent mixing in the surface layer of the atmosphere. *Contrib. Geophys. Inst. Acad. Sci. USSR*, 24(151), 163–187.
- Norris, S. J., Brooks, I. M., & Salisbury, D. J. (2013). A wave roughness Reynolds number parameterization of the sea spray source flux. *Geophysical Research Letters*, 40(16), 4415–4419. <https://doi.org/10.1002/grl.50795>
- Oakey, N. S., & Elliott, J. A. (1982). Dissipation within the surface mixed layer. *Journal of Physical Oceanography*, 12, 171–185.
- Ortiz-Suslow, D. G., & Wang, Q. (2019). An evaluation of Kolmogorov's $-5/3$ power law observed within the turbulent airflow above the ocean. *Geophysical Research Letters*, 46(24), 14901–14911. <https://doi.org/10.1029/2019GL085083>
- Ortiz-Suslow, D. G., Wang, Q., Kalogiros, J., & Yamaguchi, R. (2020). A method for identifying Kolmogorov's inertial subrange in the velocity variance spectrum. *Journal of Atmospheric and Oceanic Technology*, 37(1), 85–102.
<https://doi.org/10.1175/JTECH-D-19-0028.1>
- Osborn, T., Farmer, D. M., Vagle, S., Thorpe, S. A., & Cure, M. (1992). Measurements of bubble plumes and turbulence from a submarine. *Atmosphere - Ocean*, 30(3), 419–440. <https://doi.org/10.1080/07055900.1992.9649447>
- Phillips, O. M. (1958). The equilibrium range in the spectrum of wind-generated waves. *Journal of Fluid Mechanics*, 4(4), 426–434.
<https://doi.org/10.1017/S0022112058000550>
- Plant, W. J., Dahl, P. H., Giovanangeli, J. P., & Branger, H. (2004). Bound and free surface waves in a large wind-wave tank. *Journal of Geophysical Research C: Oceans*, 109(10), 1–14. <https://doi.org/10.1029/2004JC002342>
- Plant, W. J., Keller, W. C., Hesany, V., Hara, T., Bock, E., & Donelan, M. A. (1999). Bound waves and Bragg scattering in a wind-wave tank. *Journal of Geophysical Research*, 104(1998), 3243–3263.

- Prakash, V. N., Martínez Mercado, J., Van Wijngaarden, L., Mancilla, E., Tagawa, Y., Lohse, D., & Sun, C. (2016). Energy spectra in turbulent bubbly flows. *Journal of Fluid Mechanics*, 791, 174–190. <https://doi.org/10.1017/jfm.2016.49>
- Prosperetti, A., & Oğuz, H. N. (1997). Air entrainment upon liquid impact. *Philosophical Transactions of the Royal Society A: Mathematical, Physical and Engineering Sciences*, 355(1724), 491–506. <https://doi.org/10.1098/rsta.1997.0020>
- Pumphrey, H., & Elmore, P. (1990). The entrainment of bubbles by drop impacts. *Journal of Fluid Mechanics*, 220, 539–567. <https://doi.org/10.1017/S0022112090003378>
- Rapp, R. J., & Melville, W. K. (1990). Laboratory measurements of deep-water breaking waves. *Philosophical Transactions of the Royal Society A: Mathematical, Physical and Engineering Sciences*, 331(1622), 735–800.
- Rascle, N., Chapron, B., Arduin, F., & Soloviev, A. (2013). A note on the direct injection of turbulence by breaking waves. *Ocean Modelling*, 70, 145–151. <https://doi.org/10.1016/j.ocemod.2012.09.001>
- Rensen, J., Luther, S., & Lohse, D. (2005). The effect of bubbles on developed turbulence. *Journal of Fluid Mechanics*, 538, 153–187. <https://doi.org/10.1017/S0022112005005276>
- Riquelme, A., Desbiens, A., Bouchard, J., & Del Villar, R. (2013). Parameterization of bubble size distribution in flotation columns. In *IFAC Proceedings Volumes (IFAC-PapersOnline)* (Vol. 46). <https://doi.org/10.3182/20130825-4-US-2038.00073>
- Roy, R. A., Carey, W., Nicholas, M., Schindall, J., & Crum, L. A. (1992). Low-frequency scattering from submerged bubble clouds. *The Journal of the Acoustical Society of America*, 92(5), 2993–2996. <https://doi.org/10.1121/1.404368>
- Scully, M. E., Trowbridge, J. H., & Fisher, A. W. (2016). Observations of the transfer of energy and momentum to the oceanic surface boundary layer beneath breaking waves. *Journal of Physical Oceanography*, 46(6), 1823–1837. <https://doi.org/10.1175/JPO-D-15-0165.1>
- Shi, F., Kirby, J. T., & Ma, G. (2010). Modeling quiescent phase transport of air bubbles induced by breaking waves. *Ocean Modelling*. <https://doi.org/10.1016/j.ocemod.2010.07.002>
- Sjöblom, A., & Smedman. (2002). The turbulent kinetic energy budget in the marine atmospheric surface layer. *Journal of Geophysical Research*, 107, 1–18. <https://doi.org/10.1029/2001JC001016>

- Smith, A. W., Haus, B. K., & Zhang, J. A. (2019). Stability and sea state as limiting conditions for TKE dissipation and dissipative heating. *Journal of Atmospheric Sciences*, 76, 689–706.
- Soloviev, A. V., Vershinsky, N. V., & Bezverchnii, V. A. (1988). Small-scale turbulence measurements in the thin surface layer of the ocean. *Deep Sea Research Part A, Oceanographic Research Papers*, 35(12), 1859–1874.
[https://doi.org/10.1016/0198-0149\(88\)90113-6](https://doi.org/10.1016/0198-0149(88)90113-6)
- Soloviev, A., & Lukas, R. (2010). Effects of bubbles and sea spray on air-sea exchange in hurricane conditions. *Boundary-Layer Meteorology*, 136(3), 365–376.
<https://doi.org/10.1007/s10546-010-9505-0>
- Sreenivasan, K. R. (1995). On the universality of the Kolmogorov constant. *Physics of Fluids*, 7(11), 2778–2784.
- Stanley, R. H. R., Jenkins, W. J., Lott, D. E., & Doney, S. C. (2009). Noble gas constraints on air-sea gas exchange and bubble fluxes. *Journal of Geophysical Research: Oceans*, 114(11), 1–14. <https://doi.org/10.1029/2009JC005396>
- Stansell, P., & MacFarlane, C. (2002). Experimental investigation of wave breaking criteria based on wave phase speeds. *Journal of Physical Oceanography*, 32(5), 1269–1283. [https://doi.org/10.1175/1520-0485\(2002\)032<1269:EIOWBC>2.0.CO;2](https://doi.org/10.1175/1520-0485(2002)032<1269:EIOWBC>2.0.CO;2)
- Stewart, R. W., Grant, H. L., & Moilliet, A. (1962). Turbulence spectra from a tidal channel. *Journal of Fluid Mechanics*, 12(2), 241–268.
<https://doi.org/10.1017/S002211206200018X>
- Stewart, R. W., & Grant, H. L. (1962). Determination of the rate of dissipation of turbulent energy near the sea surface in the presence of waves. *Journal of Geophysical Research*, 67(8), 3177–3180.
- Stramski, D., & Sedlák, M. (1995). Application of dynamic light scattering to the study of small marine particles: errata. *Applied Optics*, 34(3), 571.
<https://doi.org/10.1364/ao.34.000571>
- Sullivan, P. P., & McWilliams, J. C. (2010). Dynamics of winds and currents coupled to surface waves. *Annual Review of Fluid Mechanics*, 42(1), 19–42.
<https://doi.org/10.1146/annurev-fluid-121108-145541>
- Sutherland, P., & Melville, W. K. (2015). Field measurements of surface and near-surface turbulence in the presence of breaking waves. *Journal of Physical Oceanography*, 45(4), 943–965. <https://doi.org/10.1175/JPO-D-14-0133.1>

- Suzuki, N., Hara, T., & Sullivan, P. P. (2014). Impact of dominant breaking waves on air-sea momentum exchange and boundary layer turbulence at high winds. *Journal of Physical Oceanography*, 44(4), 1195–1212. <https://doi.org/10.1175/JPO-D-13-0146.1>
- Suzuki, N., Hara, T., & Sullivan, P. P. (2013). Impact of breaking wave form drag on near-surface turbulence and drag coefficient over young seas at high winds. *Journal of Physical Oceanography*, 43(2), 324–343. <https://doi.org/10.1175/JPO-D-12-0127.1>
- Taylor, G. I. (1938). The spectrum of turbulence. *Proceedings of the Royal Society A: Mathematical, Physical and Engineering Sciences*, 164(919), 476–490. <https://doi.org/10.1098/rspa.1938.0032>
- Terray, E. A., Donelan, M. A., Agrawal, Y. C., Drennan, W. M., Kahma, K. K., Williams, A. J., ... Kitaigorodskii, S. A. (1996). Estimates of kinetic energy dissipation under breaking waves. *Journal of Physical Oceanography*, Vol. 26, pp. 792–807. [https://doi.org/10.1175/1520-0485\(1996\)026<0792:EOKEDU>2.0.CO;2](https://doi.org/10.1175/1520-0485(1996)026<0792:EOKEDU>2.0.CO;2)
- Thomas, R. E., L, S., J, M. S., S, C., & T, D. M. (2017). Bias in mean velocities and noise in variances and covariances measured using a multistatic acoustic profiler: The Nortek Vectrino Profiler. *Measurement Science and Technology*.
- Thorpe, S. A. (1984). A model of the turbulent diffusion of bubbles below the sea surface. *Journal of Physical Oceanography*, Vol. 14, pp. 841–854. [https://doi.org/10.1175/1520-0485\(1984\)014<0841:amottd>2.0.co;2](https://doi.org/10.1175/1520-0485(1984)014<0841:amottd>2.0.co;2)
- Thorpe, S. A. (1982). On the clouds of bubbles formed by breaking wind-waves in deep water and their role in air-sea gas transfer. *Philosophical Transactions of the Royal Society A: Mathematical, Physical and Engineering Sciences*, 304, 155–210.
- Thorpe, S. A. (1993). Energy loss by breaking waves. *Journal of Physical Oceanography*, 23, 2498–2502. <https://doi.org/10.1049/ir:19930072>
- Thorpe, S. A., & Humphries, P. N. (1980). Bubbles and breaking waves. *Nature*, 283(5746), 463–465. <https://doi.org/10.1038/283463a0>
- Thorpe, S. A., & Stubbs, A. R. (1979). Bubbles in a freshwater lake. *Nature*, 279, 403–405.
- Urick, R., & Kuperman, W. A. (1989). Ambient noise in the sea. *The Journal of the Acoustical Society of America*, 86(4), 1626–1626. <https://doi.org/10.1121/1.398683>
- Vargaftik, N. B., Volkov, B. N., & Voljak, L. D. (1983). International tables of the surface tension of water. *Journal of Physical and Chemical Reference Data*, 12(3), 817–820. <https://doi.org/10.1063/1.555688>

- Veron, F., & Melville, W. K. (1999). Pulse-to-pulse coherent Doppler measurements of waves and turbulence. *Journal of Atmospheric and Oceanic Technology*, 16(11 PART 1), 1580–1597. [https://doi.org/10.1175/1520-0426\(1999\)016<1580:ptpcdm>2.0.co;2](https://doi.org/10.1175/1520-0426(1999)016<1580:ptpcdm>2.0.co;2)
- Wang, Q., Alappattu, D. P., Billingsley, S., Blomquist, B., Burkholder, R. J., Christman, A. J., ... Yardim, C. (2018). CASPER: Coupled Air-Sea Processes and Electromagnetic ducting Research. *Bulletin of the American Meteorological Society*, 99(7), 1449–1471. <https://doi.org/10.1175/bams-d-16-0046.1>
- Wanninkhof, R., Asher, W. E., Ho, D. T., Sweeney, C., & McGillis, W. R. (2009). Advances in quantifying air-sea gas exchange and environmental forcing. *Annual Review of Marine Science*, 1(1), 213–244. <https://doi.org/10.1146/annurev.marine.010908.163742>
- Yelland, M., & Taylor, P. K. (1996). Wind stress measurements from the open ocean. *Journal of Physical Oceanography*, Vol. 26, pp. 541–558. [https://doi.org/10.1175/1520-0485\(1996\)026<0541:WSMFTO>2.0.CO;2](https://doi.org/10.1175/1520-0485(1996)026<0541:WSMFTO>2.0.CO;2)
- Zhang, J. A. (2010). Estimation of dissipative heating using low-level in situ aircraft observations in the hurricane boundary layer. *J. Atmos. Sci.*, 67, 1853–1862. <https://doi.org/10.1175/2010JAS3397.1>

